Development of a CFD-based model for simulation of UV-LED reactors for water treatment

by

Majid Keshavarzfathy

M.A.Sc., Sharif University of Technology, 2012

B.A.Sc., Sharif University of Technology, 2010

A THESIS SUBMITTED IN PARTIAL FULFILLMENT OF

THE REQUIREMENTS FOR THE DEGREE OF

DOCTOR OF PHILOSOPHY

in

THE FACULTY OF GRADUATE AND POSTDOCTORAL STUDIES

(Chemical and Biological Engineering)

THE UNIVERSITY OF BRITISH COLUMBIA

(Vancouver)

February 2019

The following individuals certify that they have read, and recommend to the Faculty of Graduate and Postdoctoral Studies for acceptance, the dissertation entitled:

Development of a CFD-based model for simulation of UV-LED reactors for water treatment

submitted by Majid Keshavarzfathy in partial fulfillment of the requirements for

the degree of Doctor of Philosophy

in Chemical and Biological Engineering

Examining Committee:

Dr. Fariborz Taghipour, Chemical and Biological Engineering Department, UBC
Supervisor

Dr. Madjid Mohseni, Chemical and Biological Engineering Department, UBC
Supervisory Committee Member

Dr. Boris Stoeber, Mechanical Engineering Department, UBC
Supervisory Committee Member

Dr. Mark Martinez, Chemical and Biological Engineering Department, UBC
University Examiner

Dr. Dana Grecov, Mechanical Engineering Department, UBC
University Examiner

Abstract

The ultraviolet light emitting diode (UV-LED) has recently emerged as a new UV source. It offers design flexibility due to its small size and ability to alter its radiation profile. In view of the variety of design possibilities for a UV-LED reactor, a computational model could be of great value for simulating the reactor and providing insight into its performance. Given the UV-LED's ability to emit various radiation wavelengths and because it is a directional UV source, the challenges of simulation for UV-LEDs are greater than those for UV lamps, which typically have a single wavelength and an almost radial radiation profile. This study proposes a method of simulating UV-LED reactors for water treatment in the Eulerian framework through the integration of the kinetic, hydrodynamic, and radiation models, representing UV-LED systems. Additionally, the concept of an ideal UV-LED system is proposed, which can provide insight into the efficiency of any UV-LED reactor design concept.

In this study, UV-LED is modeled as a polychromatic point source with a specific radiation profile. The radiant energy field of a UV-LED reactor is developed by considering the absorption of media, refraction and reflection at air-quartz-water interfaces, and the reflection from the internal wall surfaces. The developed radiation model was applied to different UV-LEDs, and the numerical predictions were successfully evaluated using actinometry and radiometry. The radiation model was employed to obtain the kinetic rate constants of the challenge microorganisms (e.g., *Escherichia coli* and MS2) suspended in water, and biodosimetry results showed that modifying microorganisms' 254 nm fluence-response data based on the germicidal efficiency of UV-LED could yield acceptable kinetics information. Therefore, during the development of the integrated model, the germicidal factors of UV-LEDs were used to homogenize the germicidal radiant power outputs of UV-LEDs.

The integrated model of reactor performance was evaluated through experimental studies of the challenge organisms in two UV-LED reactors under different operating conditions, including flow rates, flow regimes, radiant powers, and UV-LED configurations. The integrated model could predict the overall reactor performance and provide information that enabled to improve the efficiency 10 times.

Lay Summary

Ultraviolet light emitting diode (UV-LED) is a radiation source that emits high energy photons of a narrow spectrum. UV-LED has no warm-up time and can run on batteries or solar cells. These features make UV-LED an excellent option for the development of water treatment systems for remote areas that do not have continuous access to electricity. Since UV-LED technology offer design flexibility, a simulation tool is needed to quickly assess different design concepts. This study develops a computational model for simulating the UV-LED reactor and provides insight into its performance. The computational model of reactor performance was successfully evaluated through experimental studies of challenge organisms (e.g., *Escherichia coli* and MS2) in two UV-LED reactors under different operating conditions. Modifying reactor design based on the information provided by the computational modeling improved the efficiency of the reactor 10 times.

Preface

This dissertation is submitted for the degree of Doctor of Philosophy at the University of British Columbia. The author, Majid Keshavarzfathy, has done the literature review, designing and conducting the experiments in Chapter 2 and 4, data processing and analysis, and preparation of the thesis under the supervision of Professor Fariborz Taghipour, Chemical and Biological Engineering Department, University of British Columbia.

The construction and microbial tests in Chapter 3 were performed by Adel Haji Malayeri. The data analysis and simulation in Chapter 3 are my original work. Mélanie Meilliez, a summer student, assisted in performing some of the microbial tests in Chapter 4.

The following is the list of conference podium presentations.

Keshavarzfathy, M., Taghipour, F., (2017) The UV-LED Reactor Performance Modeling by Eulerian Method, IUVA world conference, Croatia, September 17-21

Taghipour, F., Keshavarzfathy M. (2017) Computational Modeling of UV-LED Reactors, IUVA Americas Conference, Austin, February 5–8

Keshavarzfathy, M., Taghipour, F., (2016) UV-LED Radiation Distribution in a Cylindrical Reactor. In *2016 IUVA world congress*. Vancouver.

Table of Contents

List of Tables

List of Figures

List of Symbols

Greek Symbols

α	Absorption coefficient, m^{-1}
$\alpha_{diffuse}$	The diffuse coefficient of reflective surface
β	The incident angle, degree
Γ	The ratio of actual radiation profile to the normalized radiation profile
ϵ_{352}	The molar absorption coefficient, $l \cdot mol^{-1} \cdot m^{-1}$
θ	Polar angle, degree
$\theta_{1/2}$	Half viewing angle, degree
ϑ_t	Turbulent Schmidt number
κ	Extinction coefficient, m^{-1}
λ	Wavelength, m
λ_{peak}	UV-LED peak wavelength, m
υ	Velocity, $m \cdot s^{-1}$
ρ	Density, $kg \cdot m^{-3}$
σ_s	The scattering coefficient, m^{-1}
τ	Viscous stress tensor, Pa
ϕ	The phase function for the in-scattering of photons
$\overline{\Phi}$	Average quantum yield
Ω	Solid angle, $Steradian\ (Sr)$

Roman Symbols

A	Area, m^2
A_{352}^t	The absorbance of actinometry solution at 352 at t seconds
C	The concentration of microorganisms after UV exposure, $kg \cdot m^{-3}$
C_0	The concentration of microorganisms before UV exposure, $kg \cdot m^{-3}$
d	Water depth, m
E	Irradiance, $W \cdot m^{-2}$
E_0	Fluence rate, $W \cdot m^{-2}$

$\overline{E_0}$	Volume weighted averaged fluence rate, $W \cdot m^{-2}$
$\bar{E}_{0_{surface}}$	Area-weighted averaged fluence rate, $W \cdot m^{-2}$
f	External body force, N
F	Fluence, $J \cdot m^{-2}$
F_{max}	Maximum deliverable fluence, $J \cdot m^{-2}$
$F^{H}{}_{max}$	Maximum deliverable fluence resulted from mixed flow assumption, $J \cdot m^{-2}$
F_U	Ultimate fluence, $J \cdot m^{-2}$
g	Gravitational acceleration, $m \cdot s^{-2}$
$\overline{GE}$	The germicidal efficiency of a radiation source
G_λ	Germicidal efficiency at the wavelength of λ
H	Height, m
I	Radiant intensity, $W \cdot Sr^{-1}$
I_b	The intensity of radiant energy emitted by a black body, $W \cdot sr^{-1}$
$I_{diffuse}$	The intensity of diffusely reflected radiation, $W \cdot Sr^{-1}$
$I_{specular}$	The intensity of specularly reflected radiation, $W \cdot Sr^{-1}$
$I_0\ (s)$	The radiant intensity of the emitter at the source, $W \cdot Sr^{-1}$
k'	The microbial inactivation rate constant, $m^2 \cdot J^{-1}$
L	Distance, m
m	The order of Lambertian
n	Refractive index
N	Number of microorganisms after UV exposure
N_0	Number of microorganisms before UV exposure
$\vec{N}_i$	The normal surface vector of the ith interface
p	Pressure, Pa
P	Radiant power, W
P_0	Germicidal power of UV-LED based on *B. Subtilis*, W
Q	Flow rate, $m^3 \cdot s^{-1}$
R	Radius, m
$\vec{r}_i$	Ray vector in the ith medium, m

R_i	Reflection from the ith interface
s	Directional unit vector
S	Surface area of Petri dish, m^2
S_i	Species source term, $kg \cdot m^3 \cdot s^{-1}$
s'	The scattering direction vector
T	Temperature, K
t	Exposure time, s
$\overline{U}$	The energy of one mole of photon, J
V	Volume, m^3
x	Position vector, m
x_i	Species mass fraction

List of Abbreviations

3D	3-Dimensional
CFD	Computational Fluid Dynamics
CWTP	Centralized Water Treatment Plant
DBPs	Disinfection By-Products
FWHM	Full-Width at Half Maximum
HRT	Hydraulic Residence Time
LP	Low Pressure
LPHO	Low-Pressure High Output
MOVPE	Metalorganic Vapor Phase Epitaxy
MP	Medium Pressure
NRP	Normalized Radiation Profile
PCB	Printed Circuit Board
REF	Reduction Equivalent Fluence
RTE	Radiative Transfer Equation
SMA	Sub-Miniature Assembly
SMD	Surface Mount Device
UV	Ultraviolet
UV-LED	Ultraviolet Light Emitting Diode
UVT	Ultraviolet Transmittance
WPE	Wall Plug Efficiency

Acknowledgements

I would like to express my sincere gratitude to:

- Dr. Fariborz Taghipour, my supervisor, for his continuous guidance, support, encouragement, and valuable feedback throughout this research project.
- Dr. Madjid Mohseni and Dr. Boris Stoeber, member of advisory committee, for their valuable comments.
- UBC and Natural Sciences and Engineering Research Council of Canada (NSERC) for financial support and their trust.
- All my fellow researchers, particularly to Adel Haji Malayeri and Mélanie Meilliez who offered countless hours of assistance during my project, and Ata Kheyrandish and Kai Song for teaching me analytical techniques.
- My parents and family for their love, sacrifices, encouragement, and continuous support.
- My beloved wife, Hasti, for her support and endless love throughout my study.

To my love, Hasti

Chapter 1: The fundamentals of Ultraviolet Light Emitting Diode (UV-LED) reactor

A water treatment plant removes solid particles, unwanted components, and pathogens from a drinking water source to provide clean drinking water. In the final step of the treatment process, the water is usually disinfected by chlorination. Chlorination, however, has some drawbacks. For example, it cannot disinfect all pathogens although it is effective on most of them. *Giardia* and *Cryptosporidium* are two well-known pathogens that chlorination has found ineffective for their removal [1]. Also, chlorination leads to the formation of harmful disinfection by-products (DBPs) such as trihalomethanes (THM) and Five Haloacetic acids (HAA5) [2]. Moreover, chlorination changes the taste of water, and some people do not like its taste [3]. The ozonation is another alternative to chlorination; however, this process in the presence of bromide leads to bromate formation which is a carcinogenic substance [4].

Ultraviolet water disinfection is a modern approach to cope with chlorination and ozonation shortcomings. UV treatment is effective on all sorts of microorganisms and does not lead to the formation of harmful DBPs [1]. This technology harvests high energy UV rays to inactivate microorganisms in a short period. In addition, unlike the chemical disinfectant, extra UV irradiation (overdosing) does not compromise the taste of the water [5]. The disinfection mechanism of UV technology differs from that of chemical methods, which are based on destroying or damaging cellular structures [6].

Recently, a new UV source has emerged that promises more efficient UV water treatment systems. This new radiation source, which generates UV photons using semiconductor technology, is called ultraviolet light emitting diode (UV-LED). This chapter discusses the challenges related to the simulation of the next generation of UV treatment systems that use UV-LEDs as their

primary radiation source. The following sections describe the principles of UV treatment and UV-LED technology before diving into the challenges that this study is going to address.

1.1 The principles of UV water disinfection

Ultraviolet is a form of electromagnetic radiation that ranges from 100 to 400 nm [7] and has a shorter wavelength than visible light. Ultraviolet radiation is divided into four sub-ranges of UVA (315–400 nm), UVB (280–315 nm), UVC (200–280 nm), and vacuum UV (100–200 nm). Among all, Vacuum UV has the highest energy and can be absorbed by almost all substances, so it can only be transmitted through vacuum [7]. The rationale behind the name of the first three sub-ranges pertains to their effects on human's skin. The shorter the wavelength becomes, the more detrimental effect it poses to human's skin. For example, UVA has the least harmful effect, and getting exposed to it leads to sun tanning [7]. UVC, however, has a lethal effect on human. DNA, RNA, and proteins of a living cell absorb UVC, thereby cell mutation occurs which results in cancer and ultimately cell death [1]. Since living organisms such as germs can absorb UVC, this range is called the germicidal range [1].

1.1.1 Definition of technical terms

The technical terms irradiance, fluence rate, and fluence are frequently used in this study, and their definitions are as follows:

Irradiance (Figure 1-A) represents the total radiant power incident from all upward directions on an infinitesimal element of the surface of area dA containing the point under consideration divided by dA [7]. According to this definition, a radiometer measures irradiance.

Fluence rate (Figure 1-B) is defined as the total radiant power incident from all directions through an infinitesimally small sphere of cross sectional area dA, divided by dA [7]. In a simple word, fluence rate represents the power of all photon incident on a small sphere. In a UV reactor,

photons from all direction hit microorganisms and lead to their inactivation. The fluence rate is the true representative of the delivered UV energy to microorganisms.

The amount of absorbed energy in the germicidal range depends on the fluence rate and the exposure time. The product of fluence rate and exposure time yields the total delivered UV energy (UV fluence) that determines the amount of microbial inactivation. There are different sources of UV, but here only two relevant types of UV sources are introduced.

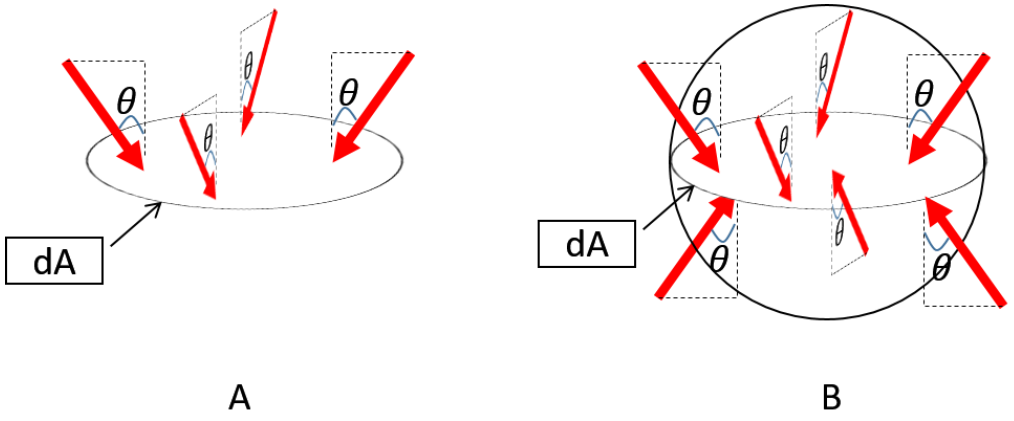

Figure 1. The illustration of the concept of irradiance (A) and fluence rate (B). The sphere represents an infinitesimally small element with cross sectional area dA, and the red arrows represent the UV beams.

1.1.2 Mechanism of UV disinfection

UVC photons carry high energy, and when DNA/RNA absorbs them, the photons cause three major damages: pyrimidine dimers, pyrimidine (6-4) pyrimidone photoproducts, and protein-DNA cross-links [6]. The dominant damage, however, is pyrimidine dimers [6]. In this case, two adjacent thymines in DNA/RNA produce a thymine-thymine dimer, and these mutagenic DNA damages disrupt the ability of the microorganism to replicate. Because microorganisms cannot replicate, they do not pose infection [1]; therefore, they are called inactivated microorganisms. The number of damaged sites on the DNA of microorganisms is important. For example, a study

showed that microorganisms inactivation happened when the number of thymine dimers in the DNA reached ~100 [8].

Proteins and DNA/RNA absorb UV differently (Figure 2). DNA UV absorption reaches a peak around 265 nm, whereas the protein UV absorption starts increasing at wavelengths shorter than 245 nm and surpasses DNA absorption at ~225 nm. A small peak in the protein UV absorption is also observed around 280 nm (Figure 2). Due to the UV absorption of proteins another type of damage in the cell membrane can occur. Such damage leads to the disruption of the cell membrane and consequently cell death [1]. Given the size of the protein UV absorption, the damage to the cell membrane occurs when the cell is exposed to a high UV fluence [1].

A microorganism undergoes a series of complex photoreactions during UV exposure. The response of the microorganism to UV arises from all those photoreactions. The action spectrum presents the combined effects of the photoreactions in terms of microorganism inactivation versus wavelength.

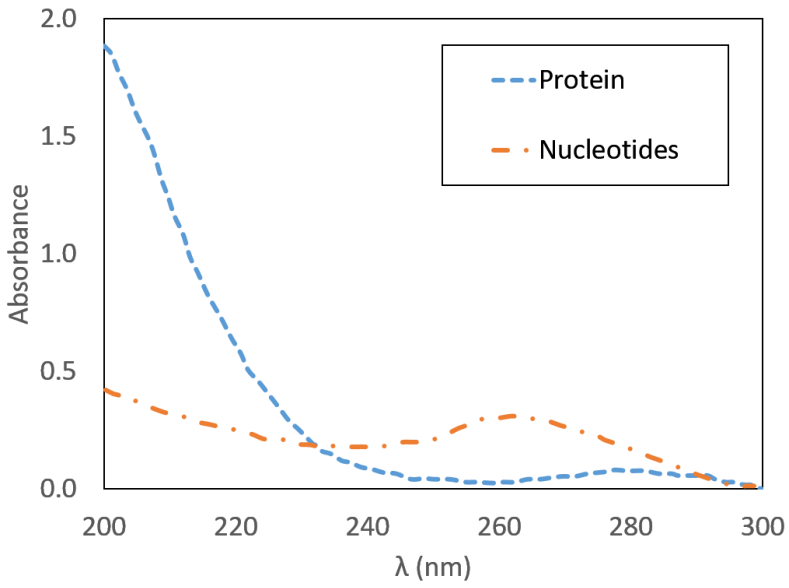

Figure 2. Specific absorption of protein and nucleotides within the cell of a microorganism (adapted from reference [1]**). Absorbance (unitless) is the common logarithm of the ratio of incident to transmitted irradiance when a beam passes through a medium over a path length l.**

Some microorganisms can repair the damaged sites through either dark or photoreactivation repair mechanism [1]. In the case of dark repair, the microorganism does not need light to restore the DNA damage. However, photoreactivation mechanism—which is more effective than the dark repair mechanism— requires UVA and/or visible light to repair the DNA damage [1]. The details of these mechanisms are explained in the literature [9]. Because of the repair mechanisms, higher UV fluences are usually applied during the treatment process.

1.1.3 Mercury lamps

Mercury vapor lamps are the primary sources of UV in water and wastewater technologies. When an electrical current in the gas excites mercury vapor atoms trapped in the quartz envelope (mainly cylindrical), these lamps emit UV radiation. Based on the pressure of the mercury vapor in the envelope, the UV lamps are categorized as low-pressure (LP), low-pressure high output (LPHO), and medium-pressure (MP) (Table 1). The principal emission wavelength of LP and

LPHO UV lamps is 253.7 nm, but MP UV lamps have a broad emission spectrum (185–600 nm). Considering their emission spectra, LP and MP UV lamps are called monochromatic and polychromatic UV sources, respectively. The optimum operating bulb temperature of LP UV lamps is ~ 40 °C [7]. Maintaining the bulb temperature around the optimum value is crucial because the output power of the LP lamp is sensitive to the ambient temperature [1]. MP UV lamps carry up ~500 times more power than that of LP UV lamps. Nonetheless, MP lamps have a relatively shorter lifetime and lower germicidal efficiency than LP lamps.

Table 1. Technical properties of conventional UV lamps [1,6]

Characteristics	LP	LPHO	MP
Emission type	monochromatic (253.7 nm)	monochromatic (253.7 nm)	Polychromatic (185-600 nm)
Mercury vapor pressure (Pa)	~0.93	0.18–1.6	40×10^3–4000×10^3
Mass of mercury for a 1.2-m lamp (mg)	~30	~30–75	2000–4000
Bulb temperature (°C)	30–50	60–100	600–900
Arc length (cm)	15–200	15–200	10–200
Lifetime (h)	8000–10000	8000–12000	4000–8000
Warm-up time (min)	2–7	2–7	4–10 (including cooldown)
Electrical input (W/cm)	0.5	1.5–10	50–250
Germicidal UV output (W/cm)	0.2	0.5–3.5	5–30
Electrical to Germicidal UV conversion efficiency (%)	35–38	30–35	10–20
Flow rate (m^3/d)	< 550	400–38000	> 38000

1.1.4 Ultraviolet Light Emitting Diode (UV-LED)

A UV-LED is a Light Emitting Diode (LED) that emits ultraviolet radiation. An LED is a solid-state semiconductor device that emits light when is connected to direct current (DC) (e.g., battery or solar panel). It requires low power (few watts) to run and has no warm-up[1] time. LED

[1] The amount of time that a lamp takes to reach its stable performance.

is rated as instant-on with full brightness device, which means that this radiation source reaches its full brightness immediately after being turned on. Therefore, LEDs can be turned on and off with high frequency without losing their performance [10–12]. The emitting region of an LED is about 1 mm^2 [13], and its emission spectrum resembles a Gaussian profile [13]. The wavelength at which the peak appears is called nominal (peak) wavelength, and conventionally a UV-LED is named by that peak wavelength. Full-Width at Half Maximum (FWHM) defines the width of the UV-LED's emission spectrum (Figure 3) which is usually about 10–15 nm. This range is the difference between the longest and shortest wavelengths at which the intensity of the emitted UV energy is half of the maximum intensity. Given the size of the FWHM, UV-LEDs, are not a monochromatic radiation source.

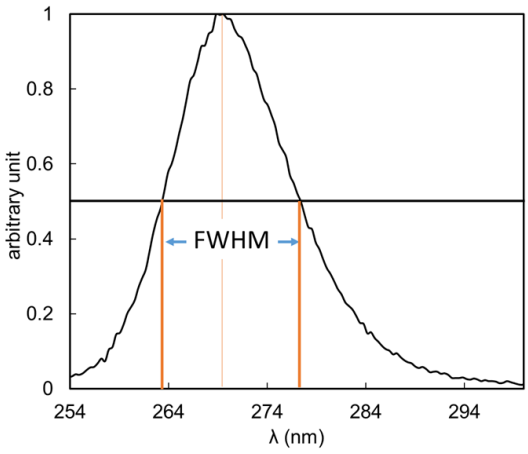

Figure 3. An emission spectrum of a UV-LED with a peak at 272 nm and the FWHM of 13 nm.

1.1.4.1 The mechanism of UV generation in UV-LED

In an LED, the semiconductor p-n junction[1] is responsible for the light generation [13]. At this junction, electrons and positive holes recombine, and the excess amount of energy releases in

[1] When p-type and n-type semiconductors are brought into contact a p-n junction is formed. The p-type and n-type semiconductors are prepared by adding an impurity (dopant) to an intrinsic semiconductor. If the impurity has one less/more valence electron than the semiconductor, p-type/n-type semiconductor forms. As for p-type

the form of light and heat (Figure 4). The non-radiative recombination generates heat which needs to be dissipated properly. The wavelength of the emitted light is inversely proportional to the energy of the semiconductor's bandgap [13] in a sense that the higher the bandgap's energy becomes, the light with a shorter wavelength is emitted. For example, the bandgap's energy of UV-LED's semiconductor such as Aluminum Nitride (6 eV [14]) is higher than that of red LEDs which use Gallium Arsenide (GaAs) (1.424 eV) [15]. The main difference between visible LED and UV-LED relates to the composition of their semiconductor materials. Wide bandgap materials, such as diamond and III–V nitride semiconductors such as Gallium Nitride (GaN), Aluminum Gallium Nitride (AlGaN) and Aluminum Nitride (AlN), are potential materials for ultraviolet LEDs but suffer from difficulties in controlling electrical conduction [14]. The flexibility in the semiconductor materials enables this technology to produce a selectable wavelength.

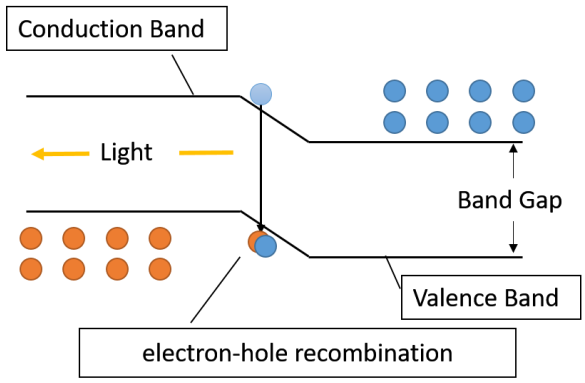

Figure 4. The energy level diagram schematic of an LED p-n junction. When a bias voltage is applied, electrons in the n-region conduction band combine with holes in the p-region valence band, excess energy equivalent to the band gap is released in the form of light and heat.

semiconductors, the positive holes (h^+) are majority positive charge carriers, whereas, the electrons (e-) in the n-type semiconductors are the dominant charge carriers.

1.1.4.2 Physical properties of UV-LED

An LED chip contains a semiconductor p-n junction (emitting region). The LED chip is prepared by the deposition layers of n-type followed by p-type semiconductors on the sapphire substrate through a process known as metalorganic vapor phase epitaxy (MOVPE) [13]. Two typical techniques in UV-LED chip fabrication are conventional and flip chip [13]. Although the conventional chip fabrication is cost-effective, the flip chip technique offers two times higher efficiency [13]. Currently, due to the formation of crystal lattice defects (the main cause of non-radiative recombination) during chip fabrication, UV-LEDs (particularly in germicidal range) suffer low performance [13,16]. For example, during epitaxial growth of GaN on sapphire, the crystal lattice defects are generated due to both the large lattice mismatch and the high thermal coefficient incomparability between sapphire and GaN [13]. In contrast to GaN, AlGaN showed the lower density of the crystal lattice defects, consequently, AlGaN has been chosen for the development of UV-LEDs for practical applications [13].

The performance of a light source is expressed using Wall Plug Efficiency (WPE). The WPE of a lamp expresses the ratio of the radiant power to the input power. While the WPE of visible LED is as high as 75% [17], commercial UVC-LEDs' WPEs ranges 1–4% [16,18]. The WPE of 7.8% for a 272 nm UV-LED has also been reported [19]; however, such UV-LEDs are not commercially available. A recent study grew AlGaN nanowires on graphene as the UV-LED substrate and UV transparent electrode [20] to improve the quantum yield. This new technique promises WPE of 45% with ten times less energy consumption [21].

When the UV-LED chip is produced, a package is needed to protect the chip. The surface mount device (SMD) (Figure 5) is commonly used as the package of a UV-LED [13]. The package includes the LED chip, wire, case, and quartz window or lens. Since UV-LEDs tend to convert a

significant amount of input power to heat—which is a result of high numbers of non-radiative recombination—they are usually mounted on a metal core Printed Circuit Board (PCB). Despite the small size of the LED chip, a UV-LED package is about ~ 6 mm long.

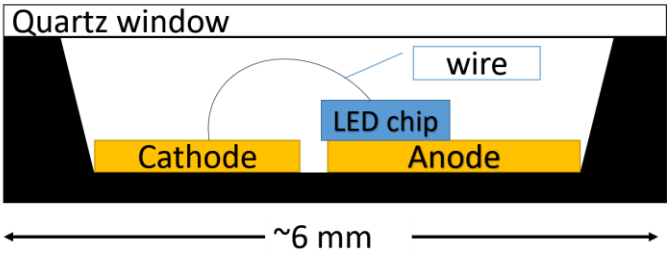

Figure 5. The schematic of the surface mount package of a UV-LED

The packaging and the orientation of the chip play essential roles in UV-LED's radiation pattern [13,22]. The extracted photons from the LED chip hit the internal surface of the package and then leave the package through the window. The radiation pattern of a UV-LED depends on the chip structure. The radiation pattern of an LED expresses the directional dependence of the radiant energy from the LED chip.

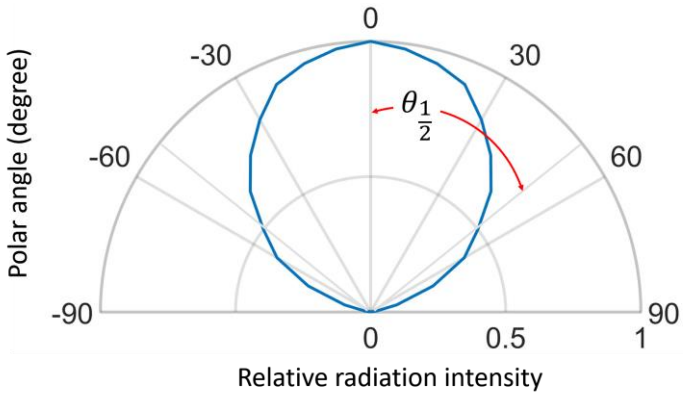

Figure 6. A normalized UV-LED radiation profile in polar coordinate is shown. Blue line illustrates the intensity of radiation versus polar angle. The half viewing angle ($\theta_{\frac{1}{2}}$) represents the angle at which the

intensity of radiation becomes half of the maximum intensity. For a UV-LED with symmetric radiation profile, the viewing angle is 2 times $\theta_{\frac{1}{2}}$.

1.2 The access to safe drinking water in developing countries and remote areas is the major problem

People in developing countries struggle to access to safe drinking water, and the demand for clean and safe drinking water has risen due to rapid urbanization [10], economic growth and higher awareness [11]. Similar to developing countries, those who live in remote areas in developed countries [10,23] such as First Nation communities in Canada [24–26] struggle to access to safe drinking water. One type of health-threatening incident in developed countries is microbial contamination in the water distribution network. The number of boil-water advisories in Canada [27,28] shows the frequency of the related incidents.

In developing countries, people collect water from a certain location and carry the water to their homes. The source water refers to the water that is collected at that location. The issue of providing safe drinking water for all cannot be addressed only by improving the source water [29]. The reason is that the water likely gets contaminated after being collected. Also, the idea of building a centralized water treatment plant (CWTP) is not viable because the capital and operation costs of the CWTP are not affordable for low-income communities. Besides, the water consumption of a small community throughout the day fluctuate intensely [10], which makes the situation more difficult for the implementation of CWTP. In regions that CWTP exists, rapid urbanization and population growth limit access to the clean water [10]. In these cases, people tend to use water from unprotected dug well which is prone to the occasional microbial contamination [10]. In developing countries, there is not continuous access to electricity, so people tend to store water in a storage tank on their rooftops [30]. In such condition, chlorine residue decay over time

[10], thereby the quality of water drops. The shortcomings of the current strategies emphasize the urgent need for the implementation of point-of-use (POU[1]) and/or point-of-entry (POE[2]) water treatment systems to address the issue.

The common implemented POU technologies to restrain diarrhea are boiling, chlorination, bio-sand filtration, ceramic filtration, and solar disinfection [29]. Boiling is an energy-intensive process which is practical for a small amount of water; if the water is not stored properly, it is prone to recontamination. Water chlorination is not effective on *Giardia* and *Cryptosporidium* [1], produces harmful DBPs [1], and some consumers do not like the taste of it [3]. The drawbacks of filtration can be listed as follow: clogging, slow treatment [31], and not being effective on viruses (due to small size). Ceramic filters produce higher water quality than bio-sand filters, but both ceramic filters and solar disinfection offer slow treatment process [31] and are not suitable for instant water treatment purpose.

Providing clean water at the point of use is a multifaceted issue. A technology that entails the following criteria could address this issue. These criteria are being reliable, cost-benefit, easy-to-use, maintenance free and/or low maintenance cost [29], on-demand, able to handle intermittent flow rates [10], low power consumption, and not being dependent on climate or ambient temperature. Ultraviolet treatment technology was used in different projects to provide clean water for small communities [31,32]; however, they all suffered from recontamination problem. Consuming the water at the point-of-use immediately after the treatment protects the water against recontamination. Barstow et al. [29] showed that an ultraviolet reactor that treats water on-demand

[1] The POU water treatment systems refer to the units that treat water very close to where the water is used. A filter that lies before the faucet is an example of POU system.

[2] As for POE systems, they are put where water from distribution network flows to the water meter of a building. A POE system treats all of the incoming water to the building.

is a reliable alternative to all the POU methods mentioned above. Although the UV reactor could effectively treat 1 L/min of the water, it was more expensive ($65) than other the POU technologies. Besides, due to the long warm-up time of UV lamp, such reactor needs to operate continuously or be turned on well ahead of the treatment process.

UV-LED can address the shortcomings of the UV lamp in the field of POU/POE systems. UV-LED can easy handle intermittent water use because of its fast start-up [10]. In addition, UV-LED can be operated by battery or solar cell (low DC power requirement) which makes it a viable alternative for a remote area that does not have continuous access to electricity. The operating temperature of UV-LED is around 30 °C and has a negligible impact on the scaling effect on the quartz sleeve; therefore, there is no need to install wiper to clean the quartz sleeve similar to mercury lamps. The lifetime of UV-LEDs is improving fast [13,17], and taking into account their ability to meet the intermittent water use; a UV-LED system offers a longer lifetime than a similar UV lamp system. Furthermore, the cost of both lamp replacement and maintenance reduce concurrently. The aforementioned factors could make UV-LED technology reliable and affordable. Also being free from mercury makes this technology an environmentally-friendly radiation source for POU/POE systems.

1.2.1 The challenges associated with the simulation of UV-LED reactors

To fully and optimally benefit from the specific features of UV-LED technology for water disinfection, it is necessary to investigate the interaction of the three complex phenomena hydrodynamics, radiation, and kinetics that indicate the reactor performance. It has been shown that the phenomena above can be integrated and be solved by a numerical simulator such as Computational Fluid Dynamics (CFD) software package for UV reactor modeling (e.g., [33–35]). The challenges associated with the development of an integrated model for simulating UV-LED

reactors, however, is greater compared to that of UV lamp reactors. For example, specific features such as various UV-LED's radiation patterns and polychromatic radiation output [36] of UV-LEDs should be considered during the modeling the reactor radiation and kinetics.

1.3 Knowledge gaps and challenges

1.3.1 Development of an accurate radiation model

Microorganisms accumulate the UV energy along their trajectories inside the reactor, and the accumulated fluence determines their inactivation. As defined earlier, UV fluence is equal to the fluence rate multiplied by the exposure time, and the exposure time is a function of the hydrodynamics of the reactor. Therefore, the interaction of radiation distribution and fluid flow determines the delivered radiant energy to microorganisms in a UV reactor. The accuracy of a UV reactor performance simulator highly depends on the accuracy of the radiant energy field inside the reactor. Thus, it is essential to take into account all the main phenomena that affect the reactor's radiant energy field. For this purpose, the UV source, the propagation of beams through different media, and the reflection from the internal walls need to be modeled accurately.

A UV-LED is a directional radiation source with a variety of radiation patterns [13,37] and the typical UV lamp radiation models cannot be directly applied to UV-LEDs radiation modeling. In some studies reported in the literature, UV-LED radiation has been modeled similar to a cone where the UV-LED was on the cone's apex, and the cone's angle was determined by the UV-LED's viewing angle [36, 37]. In another attempt, a UV-LED has been modeled as a small transparent emitting surface through which UV rays get into the reactor [40]. These approaches, however, do not consider the correct emission from the UV-LED source. Therefore, using these approaches results in two different UV-LEDs with the same viewing angle but different radiation profiles to have the same simulated radiation distribution (Figure 7), which is not a reflection of

reality. In a different approach, a UV-LED was modeled as a Lambertian source [41]. This simplifying assumption in the modeling of UV-LED's radiation profile, however, has been shown to lead to incorrect fluence rate predictions [42]. In a more realistic method, the intensity variation across the polar angle was captured by appropriate mathematical functions (e.g., polynomial functions) [43,44]. This method assumes the UV-LED's radiation profile is symmetric and is not a function of the azimuthal angle. The accuracy of this method depends on the fit function. Apart from the approaches in modeling the UV-LED's radiation emission, some simplifying assumptions associated with the behavior of the UV rays after being emitted from the source such as neglecting UV beam refraction at a quartz interface [38] and the reflection from the reactor's internal wall [44] have also been made during the determination of the radiant energy field. The determination of the radiant energy field within a UV reactor is a delicate matter, and for this purpose, a comprehensive model is required.

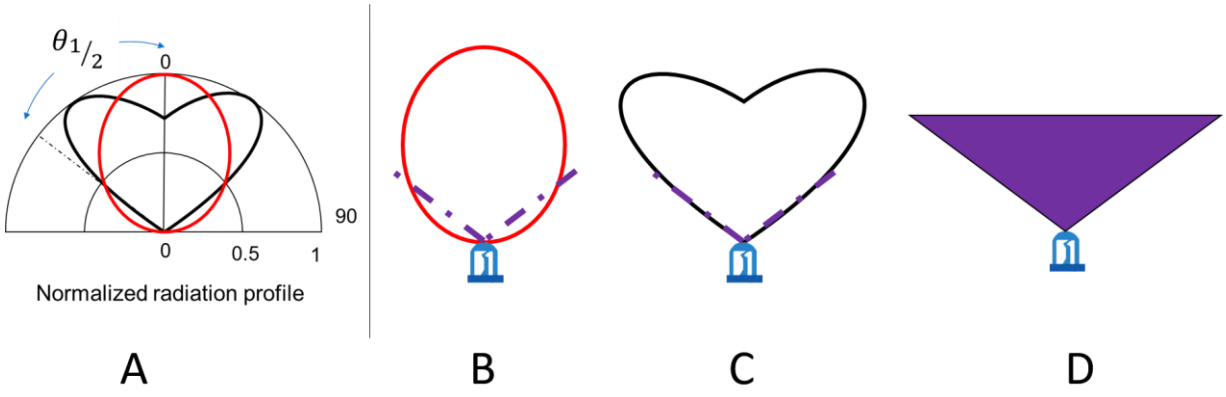

Figure 7. (A) shows two different UV-LED radiation profiles with the same viewing angle in polar coordinate. If UV-LEDs are modeled only based on their half viewing angles ($\theta_{1/2}$), two UV-LEDs with the same viewing angle but different radiation profiles (e.g., balloon shaped (B) and heart shaped (C)), will have the same simulated radiation distribution (D).

The propagation of UV rays across the reactor can be calculated by solving the Radiative Transfer Equation (RTE) using different numerical methods [45]. Among all, Monte Carlo and Finite-Volume methods have been commonly used for photoreactor modeling [46]. A ray tracing algorithm based on the Monte Carlo method is capable of handling complex geometries with accuracy, but getting an accurate solution is computationally intensive [47]. Similarly, in the finite volume methods, more computational resources are required if spatial and angular discretization increase [48]. In a 3-dimensional (3D) domain, obtaining a radiant field with high resolution needs powerful computers. For engineering application with limited resources, an accurate technique which requires less computational resources is preferable. The method of radiation modeling should be able to be implemented in general purpose computational fluid dynamics (CFD) software and enables the integration of radiation and hydrodynamics data in one platform. In general, the proposed method accelerates the design process by providing readily available radiation data during the reactor performance simulation.

1.3.2 UV-LED microbial inactivation kinetic study

Kinetics data are essential for UV reactor design and evaluation. The UV microbial inactivation is a function of fluence rate and exposure time. Therefore, the determination of the delivered fluence rate to a well-mixed microbial suspension is necessary to the UV inactivation study. The Collimated Beam Apparatus (CBA) [58] is usually used to irradiate a well-mixed microbial suspension inside a Petri dish. The CBA involves a UV lamp that irradiates the petri dish containing microbial suspension through a long tube, which ensures the delivered UV beams to the surface are parallel to the tube axis (Figure 8). Once the irradiance at the surface of the water in the Petri dish is measured, using four correction factors the delivered fluence rate is determined. The correction factors account for the divergence of beams, the reflection at the water surface, the

water absorption, and the uniformity of radiation at the water surface. The uniformity of radiation over the water surface is quantified using the Petri Factor, which is the average of irradiance divided by the irradiance at the center of the Petri dish.

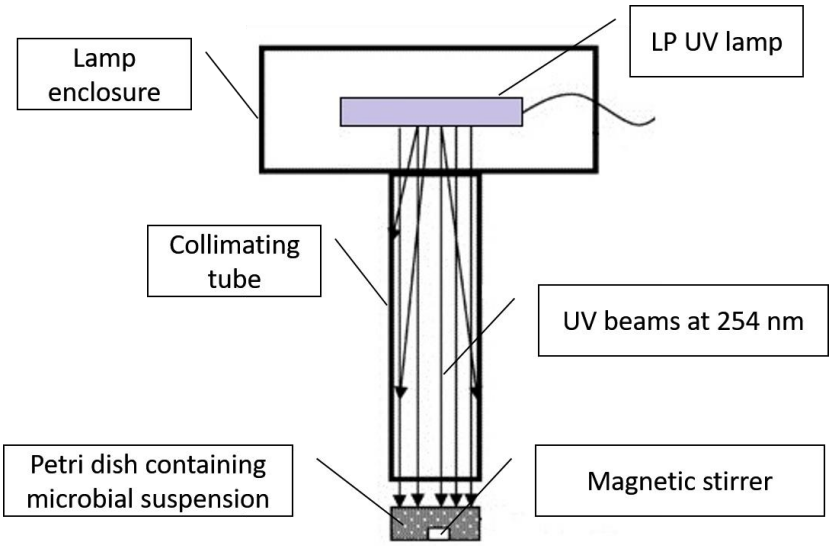

Figure 8. The schematic of the collimating beam apparatus (CBA)

Due to the low power of a UV-LED and its angular radiation pattern, it is not practical to replace the UV lamp with a UV-LED in the CBA. Several studies have employed UV-LED water disinfection units [16,39,49,50], but each has applied different methods to quantify the delivered fluence rate to the microbial suspension in order to study the kinetic of UV-LED microbial inactivation. There are uncertainties associated with the kinetics data reported for UV-LEDs of various wavelengths [51]. The disagreements can be attributed to differences in the UV-LED fluence rate determination methods.

The first essential step for studying UV-LED microbial inactivation is delivering the accurate estimation of the UV fluence rate to a well-mixed microbial suspension. It is only then that the UV fluence response data can be analyzed to calculate the inactivation rate constants. One

study performed biodosimetry[1] with MS2 (a challenge organism) to determine the delivered fluence rate to a well-mixed suspension and used the obtained fluence rate to derive the kinetics of other microorganisms [52]. The results of such method should be used with extra care because microorganisms have different action spectra, and the calculated fluence rate for one organism cannot be directly used for another one unless they have the same action spectra. Besides, the accuracy of the derived kinetics depends on the accuracy of the biodosimetry test with MS2 in the first place, so this method inherently introduces extra experimental errors in the process of microbial kinetics study. Finally, it is not practical to perform the biodosimetry test before each microbial inactivation study because this technique is time-consuming, costly, and resource-intensive.

A validated numerical method could determine UV fluence rate fast and reliably. In an attempt to design the equivalent of an optimum collimated beam apparatus using the numerical technique to investigate the irradiance distribution on the water surface in a petri dish, the UV-LED was modeled as a point source, so the radiation profile was similar to a cone, and the emission angles were limited to a predefined range [39]. As explained above, simplifying assumptions could lead to incorrect fluence rate determination. Kheyrandish et al. [42] used the LEDs' radiation profiles to predict the irradiance distribution and fluence rate on the water surface. The study showed that at farther distances between UV-LED and the water, the uniformity of fluence rate increased, but the amount of delivered fluence rate decreased substantially compared to near distances [42]. Insufficient radiation energy imposes a long exposure time when a highly UV-

[1] Biodosimetry is a procedure through which the delivered fluence (dose) to microorganisms is measured [6].

resistant organism or photochemical reaction is to be studied. This deficiency can be compensated by either placing UV-LEDs closer to the water or increasing the numbers of UV-LEDs.

The new proposed UV-LED fluence rate determination method [22], which is a modified version of Bolton's method [53], showed that placing a typical UV-LED 13 cm above the petri dish was sufficient to reach the acceptable range of collimation [22] (i.e., Petri factor > 0.9). The new proposed method requires the irradiance is measured across the water surface accurately, which needs a precise apparatus that is not always available. Furthermore, the amount of fluence rate of the single UV-LED 13 cm above the water, was one-tenth of that of usually seen for UV lamps. The low fluence rate requires a longer exposure time to deliver a required fluence. In the case of inactivating UV resistant organisms, such small fluence rate leads to hours of exposure, which is not practical. More UV-LEDs are needed to address the power deficiency. The problem with the increase in the number of UV-LEDs is that UV-LEDs must have the same emission spectrum. Currently, the nominal wavelength and FWHM of commercial UV-LEDs cannot be guaranteed. The UV-LED technology is not mature yet, and the peak wavelength may vary in the range of 10–15 nm for the same batch of UV-LEDs. DNA UV absorption changes significantly around 260 ± 20 (Figure 2), and the variations in the UV-LED emission spectrum could result in entirely different kinetics. For example, separate studies have reported different kinetic rate constants for 265 nm and 285 nm UV-LEDs [16,50], which implies the significance of the emission spectrum. Kheyrandish et al. [22] suggested that if a UV-LED is to be placed closer to water, a numerical model needs to be employed to account for all the phenomena that contribute to the radiant energy field distribution. Yet, the radiation modeling of UV-LED has not been employed to predict the fluence rate inside the water by considering accurate UV-LEDs' radiation

profile and main phenomena (i.e., refraction, reflection, and absorption) that affect the radiation distribution.

1.3.3 Development of an integrated model

Generally, there are two methods of Lagrangian and Eulerian for UV reactor simulation using a CFD software package. In the Lagrangian method, a flow field is achieved by solving the governing equation of mass and momentum, and then particles (as a dispersed phase) are released, and their trajectories are computed using the equations of motions (Newton's second law). The accumulated UV fluence for the particles is computed by considering fluence rate distribution inside the reactor and each particle trajectory. Finally, the overall performance of the UV reactor is obtained when the kinetic of microorganism is applied to the accumulated fluence of the particles [33]. The accuracy of the Lagrangian approach depends on the number of particles. Typically, a large number of particles is released to simulate the overall performance. However, particles cannot cover the entire numerical domain. Although the Lagrangian approach has been used for UV-LED reactor simulation [38], this method is unable to illustrate concentration and accumulated fluence distribution for the entire reactor, which is necessary for reactor modification and analysis of local performance.

In the Eulerian framework, the conservation equations of mass and momentum along with species mass conservation equations are solved to obtain species concentration profiles across the reactor [34]. In the Eulerian modeling, the entire numerical domain is counted for the simulation, and each computational cell behaves similarly to a small completely-mixed reactor. This technique of simulation provides extra information such as the concentration distribution, the rate of reaction, and the accumulated fluence distribution. Concentration profile has the history of received fluence for all species from the inlet of the reactor all the way to the outlet. Therefore, the concentration

information can be converted into the accumulated fluence for the entire domain using the kinetic data. The accumulated fluence shows how species receive fluence throughout the reactor. This information along with the local fluence rate are two essential data for assessing the performance of a reactor as well as design optimization. Yet, to our knowledge, no published study has simulated UV-LED reactor in the Eulerian framework.

1.3.4 An ideal UV-LED reactor

A UV-LED offers design flexibility. For example, UV-LEDs can be placed outside [38,44] or inside [50] a reactor and run wirelessly [54], thanks to their low DC power consumption. Although design flexibility is an advantage, at the same time, it adds up to the complexity of the process of the reactor design. Even though CFD simulation helps to understand how a reactor behaves, it does not suggest the most effective design for UV-LED reactors by itself. Theoretical work is required to study the concept of the ideal UV-LED reactor. Such concept opens the door for innovative designs and allows to investigate the conditions at which a UV-LED reactor can perform optimally. The knowledge that is derived from the ideal UV-LED reactor investigation allows harnessing CFD tool to design efficient UV-LED reactor.

An ideal reactor delivers the maximum fluence, but to our knowledge, the concept of ideal design for UV-LED reactors has not been discussed in the published studies. Quantifying the maximum deliverable fluence contributes to the field of reactor design in different ways. Generally, it sheds light on the room for design improvement and serves as a fundamental equation for feasibility studies and initial cost estimation for the implementation of UV-LED water treatment systems.

1.4 Objectives and thesis outline

This project aims to develop and evaluate a computational model to simulate UV-LED reactors for water disinfection. This computational model inherently requires models for hydrodynamics, radiation, and the kinetics of inactivation. The hydrodynamics of the UV-LED reactors are similar to those of UV lamps; therefore, based on the information provided in the literature, the appropriate models are chosen for the simulation of the flow field.

The development of an accurate radiation model for UV-LEDs is required to determine the radiant energy field for building an integrated model of reactor performance. For this purpose, the UV-LED is modeled by considering its actual radiation pattern as well as the phenomena such as refraction, reflection, and absorption of UV rays during the propagation inside the reactor. The radiation model is assessed by different techniques such as radiometry and actinometry. Chapter 2 presents the details of the radiation modeling.

The kinetics data of microbial inactivation are necessary for reactor modeling and evaluation. This study presents the numerical method, which can be applied to any UV-LED, for the determination of the delivered fluence rate to the microbial suspension in the Petri dish. Chapter 3 provides a detailed explanation of the numerical method along with the experimental data which were used for the model evaluation.

In Chapter 4, the procedures for developing a CFD-based model (integrated model) that simulates UV-LED reactors in the Eulerian framework are described. The integrated model is evaluated by biodosimetry technique in various operating conditions such as different flow rates, UV-LED configurations, and input powers. This chapter provides a detailed explanation for performance assessment and design modification.

The concept of an ideal UV-LED reactor is investigated in Chapter 5, and a mathematical formula is developed for the calculation of the maximum delivered fluence (dose). Chapter 5 shows the application of the integrated model and demonstrates the efficiency of a UV-LED reactor if the concept of the ideal UV-LED reactor is implemented. Finally, Chapter 6 presents a summary of this research study along with some recommendations for future studies.

1.5 Significance

This study proposes a general method for simulating UV-LED radiation by simplifying the radiative transfer equation when the UV-LED radiation profile is modeled accurately. The method incorporates all the attenuating factors happening during the UV ray propagation. The effects of reflection from the internal wall surfaces are also considered, which allows investigating the radiation distribution within a reactor with reflective surfaces. This method is not available by default in the commercial CFD software packages (e.g., ANSYS Fluent). The proposed numerical procedure can be implemented in general-purpose CFD software packages to simulate the radiation distribution of any UV-LED reactors with arbitrary geometry. This method requires less computational resources than the ray tracing and control volume techniques.

The kinetics data are essential for photoreactor design and evaluation. The accuracy of the kinetics data depends on the determination of the delivered fluence rate. This study develops a numerical method to determine the delivered fluence rate to the microorganisms suspended in water, which undergo photochemical reactions during UV exposure. The developed model can be implemented to study the kinetics of any photochemical reaction induced by UV-LED irradiation. Using the developed method, the fluence rate in a solution can be accurately estimated regardless of the position of UV-LED, the number of UV-LEDs, and the geometry and size of the container.

The UV-LEDs impose different effects on microorganisms depending on their emission spectra. When a reactor has various UV-LEDs of different wavelengths, the effect of each UV-LED needs to be modeled separately, resulting in a more complicated simulation which requires higher computational resources. An alternative approach can be the use of the same kinetics data for all UV-LEDs if their germicidal powers are used. To do so, this study finds the germicidal efficiency of UV-LEDs based on the emission spectra of UV-LEDs and the action spectra of microorganisms and used the 254 nm kinetics data obtained from the standard protocol [55]. This study uses the action spectra of *E. coli* and MS2 instead of their DNA action spectra because the microorganism action spectrum encompasses all the inactivation effects induced by UV exposure and truly represents what happens in reality. This method eliminates the necessity of developing the kinetics data for each UV-LED and leads to reliable information. Also, this method makes the simulation of the reactors which comprise different UV-LEDs more efficient because a single kinetics equation is solved for all UV-LEDs.

The design and optimization of a UV-LED reactor are challenging. Identifying areas with poor performance and prioritizing them requires the simultaneous analysis of the local fluence, accumulated fluence, and concentration profiles. Such invaluable pieces of information cannot be obtained by the Lagrangian modeling. This study proposes a general guideline for simulating UV-LED reactor in the Eulerian framework along with a method for the prioritization of low performing regions. The robust CFD-based model developed in this study can be utilized as an engineering tool to design, optimize and scale-up UV-LED reactors. Further, the proposed method can be applied to any similar photoreactor to improve efficiency.

The maximum performance of a UV-LED reactor is a piece of key information because by comparing the simulation results and the maximum performance, the room for the design

improvement is identified. This study proposes an ideal UV-LED reactor and develops a mathematical formula that estimates the maximum possible fluence that can be delivered by a single UV-LED. Based on the mathematical formula, the power consumption and the number of UV-LEDs can be determined even before simulating the reactor, which is a valuable piece of information during the feasibility studies. The formula can be applied to similar UV-LED system to estimate the power consumption and/or the maximum performance.

Chapter 2: A general method for the radiation modeling of UV-LED

2.1 Introduction

As explained in Chapter 1, the interaction of radiant energy field and hydrodynamics determines the delivered UV energy to each microorganism and the overall disinfection performance of a UV reactor. Therefore, it is essential to predict the radiant energy field inside a UV reactor accurately. Different radiation models have been developed for UV lamps [56–59]; however, since UV-LED is a directional radiation source with different radiation profiles, UV lamps radiation models cannot be directly applied to UV-LEDs. Moreover, since UV-LED is polychromatic [36], the absorption spectra of media such as the quartz window and the water need to be considered for the simulation of the UV rays propagation. To simulate radiation distribution, UV source geometry and its characteristics, the propagation of rays through different media, and the reflection from the reflective surfaces need to be considered.

The attempts for UV-LED modeling and the integration of the radiation model into CFD software programs were reviewed in Chapter 1. The developed radiation models have drawbacks such as the simplification of UV-LED radiation profile, the neglection of UV reflection from internal surfaces, and the lack of attention to the emission spectrum of UV-LEDs (i.e., monochromatic assumption). It has been reported that employing simplified radiation profiles for UV-LEDs results in incorrect fluence rate determination in a petri dish [42], which is one of the simplest types of photoreactors. Given the complexity of the UV rays propagation in a flow-through reactor, applying such models to the real-world problems leads to incorrect predictions.

The study of the effect of reflection on microbial inactivation in a batch reactor showed the cultivating of the reflected rays could significantly improve fluence rate [43,60,61], and such

results suggest that the UV reflection needs to be considered in the radiation modeling of a flow-through UV-LED reactor as well.

UV-LED is typically modeled as a monochromatic radiation source, but the validity of such an assumption needs to be studied. The absorption coefficient of the water and the commercial grade quartz vary over the germicidal range. Around 260 nm, the variation of the water absorption coefficient is negligible. However, the absorption coefficient of the commercial grade quartz increases with wavelength. Since UV-LED is polychromatic, the weighted average of the absorption coefficient of the quartz seems a better approach. Another effect of the variation of the quartz absorption coefficient on the reactor simulation relates to its effect on the spectrum of light that is sensed by microorganisms. Since the absorption varies by wavelength, the emission spectrum of light source alters after passing through the quartz window. Basically, the window behaves as a light filter which selectively reduces the energy of some photons. The microbes receive the emission spectrum after the quartz window, so they could exhibit different kinetics than what is observed in the collimated beam apparatus. Yet, the effect of quartz absorption on the radiation distribution and germicidal efficiency have not been considered in the radiation modeling.

Apart from the development of a reliable radiation model, the evaluation of that is also challenging. The main challenge is that there is not a detector to measure the fluence rate in the water. The challenge, however, can be addressed by measuring the irradiance using a radiometer when the reactor is empty. A radiometer (detector) is a device that measures the total irradiance

incident on a sensor[1] element [7]. Despite the approval of radiometry test, it is a sensitive experiment. The size of the sensor and the orientation of the detector are two critical parameters that affect the credibility of the radiometry test. The details of the sensor size and its effects on irradiance measurements can be found elsewhere [36]. Overall, measuring irradiance in the entire reactor is very time-consuming and sometimes reactor geometry limits such measurements.

Further, it is not practical to immerse the detector in water to measure irradiance. As for UV-LED reactors, irradiance measurement requires a tiny detector which is not always available. To cope with the mentioned difficulties, photoluminescence processes were used to capture the irradiance distribution in air and water in order to qualitatively investigate the radiation model predictions. In the photoluminescence processes the intensity of light is related to the energy of the absorbed photons; therefore, the captured light distribution using the photoluminescence process can be used for the evaluation of the radiation model predictions.

In this study, a method for the modeling of the radiant energy field of a UV-LED reactor is proposed by considering the actual radiation profile of the UV-LED, the absorption of media, refraction and reflection at air/quartz/water interfaces, and the internal wall reflection. In this method, RTE is simplified so that it can be solved for any UV-LED. The proposed radiation model was primarily intended to be integrated into a commercial CFD software package to simulate the performance of a UV-LED reactor. In this project, ANSYS Fluent was used to implement the proposed method. The irradiance was evaluated qualitatively and quantitatively using photoluminescence processes and radiometry test, respectively.

[1] The sensor consists of a photocell that generates electricity once hit by photons [7]. The amount of current pertains to the photons' energy

2.2 Material and methods

2.2.1 Radiation model

The propagation of photons in an absorbing, scattering, and emitting medium in space is described by the radiative transfer equation. For a monochromatic wavelength, RTE in steady-state condition can be written as:

$$s.\nabla I(x,s) + (\kappa + \sigma_s)I(x,s) = \kappa I_b(T) + \sigma_s \int_{4\pi} \phi(s,s')I(x,s')d\Omega(s') \quad (1)$$

where I is the radiant intensity, x is the position vector, s is the directional unit vector, κ is the absorption coefficient, σ_s is the scattering coefficient, I_b is the black body emissivity function that depends on the medium temperature (T), ϕ is the phase function for the in-scattering of photons, Ω is the solid angle about the scattering direction vector s′. On the left-hand side of Equation 1, the first and second terms describe the change of radiant intensity, and energy loss due to absorption and out scattering, respectively. The right-hand side describes intensity gain due to medium temperature and in-scattering effect.

Before simplifying RTE, it should be noted that water disinfection is the final step of the water treatment process, and there is typically no particulate matter in the water to scatter light (i.e., σ_s~0). Also, UV emission due to water temperature is extremely low; therefore, the magnitude of black body emission is negligible (i.e., I_b~0). Finally, since the medium is homogenous, it is assumed the absorption coefficient is constant and is not a function of the direction vector (i.e., κ is isotropic). Because $s.\nabla I(x,s)$ is equivalent to $\frac{dI(x,s)}{ds}$, RTE in its integral form can be written as follows (Equation 2):

$$I(\mathrm{s}) = I_o(\mathrm{s}) * e^{\int_0^L k\,dx} \quad (2)$$

where $I(s)$ and $I_0\ (s)$ are the radiant intensity of the emitter at the distance of L and the radiant intensity of the emitter at the source, all for the specific direction vector (s), respectively. According to the irradiance and intensity definitions [7], irradiance for a specific direction, s, on an infinitesimal circular area, A, is equal to $\frac{I(s)*\mathrm{s}}{A}$ [48]. For an infinitesimal circular area, s can be approximated as $\frac{A}{L^2}\cos(\beta)$, where β represents the incident angle on the area. Substituting the solid angle with its approximation results in irradiance equation (Equation 3).

$$E(\mathrm{s}) = \frac{I(\mathrm{s})\cos(\beta)}{L^2} e^{-\int_0^L k\, ds} \qquad (3)$$

where $E\ (s)$ is the irradiance for a specific direction vector (s). The radiation pattern of any UV-LED can be substituted as $I(s)$. Here, in order to accurately capture the UV-LED radiation profile, Equation 4 which was proposed by Wue et. al. [62] was fit to the LED normalized radiation profile (NRP) (i.e., $\Gamma = 1$). After substituting the order of Lambertian, *m*— which was given by the semi-angle at a half illuminance of the LED, $\theta_{½}$ (i.e., $m = \frac{-ln2}{\ln(cos\ \theta_{\frac{1}{2}})}$)—the constants C_0–C_4 were obtained.

$$I(\theta) = \Gamma(C_4\theta^4 + C_3\theta^3 + C_2\theta^2 + C_1\theta + C_0)cos^m\theta \qquad (4)$$

Since it was assumed that NRP was symmetric around the UV-LED normal axis and did not depend on an azimuthal angle, Equation 4 was expressed as a function of emission angle, θ; thus, $E\ (s)$ turned to $E\ (\theta)$. An experimental measurement was needed to obtain the magnitude of Γ, and consequently the actual radiation profile. The integral of $E\ (\theta)$ over the surface of a hemisphere with an arbitrary radius, R, was calculated and compared against the radiant flux measured by an integrated sphere. In this way, the power of a UV-LED can be conveniently adjusted using Γ.

The propagation of photons through the media is affected by refraction, reflection, and absorption. As shown in Figure 9, the UV source is typically separated from the water by means of a quartz window, and due to the differences in the refractive indices of the media, UV beams undergo refraction at air/quartz/water interfaces. The direction of the refracted rays was calculated using the following equation (Equation 5):

$$\vec{r}_{i+1} = \left(\frac{n_i}{n_{i+1}}\right)\vec{r}_i + \left[\left(\frac{n_i}{n_{i+1}}\right)\left(-\vec{N}_i.\vec{r}_i\right) - \sqrt{1-\left(\frac{n_i}{n_{i+1}}\right)^2\left(1-\left(-\vec{N}_i.\vec{r}_i\right)^2\right)}\right]\vec{N}_i \quad (5)$$

where $\vec{r}_{i+1}$ is a refracted vector, $\vec{r}_i$ is a ray vector, subscript i points to the medium number, n is the refractive index, and $\vec{N}$ is the normal vector of the interface. Given UV-LEDs are separated from water using a quartz window, there are three media air, quartz, and water that need to be taken into consideration. The refractive indices of air, quartz, and water are 1, 1.48, and 1.37, respectively. According to Fresnel's law, a part of the energy of the refracted beams is reflected back at the interfaces and get lost (i.e., R_1 and R_2 in Equation 6). In addition to refraction and reflection, UV beams lose energy along their path due to the absorption. Equation 6 expresses the irradiance function by considering the effect of absorption, refraction, and reflection. As explained earlier, since fluence rate is not a function of incident angle, if the $cos(\beta)$ is removed from Equation 6, the fluence rate equation is obtained. Fluence rate is the most determinant information for the prediction of the delivered fluence (UV dose) to microorganisms.

$$E(\theta) = \frac{I(\theta)\cos(\beta)}{(L_1+L_2+L_3)^2}(1-R_1)(1-R_2)e^{-(\kappa_1.L_1+\kappa_2.L_2+\kappa_2.L_3)} \quad (6)$$

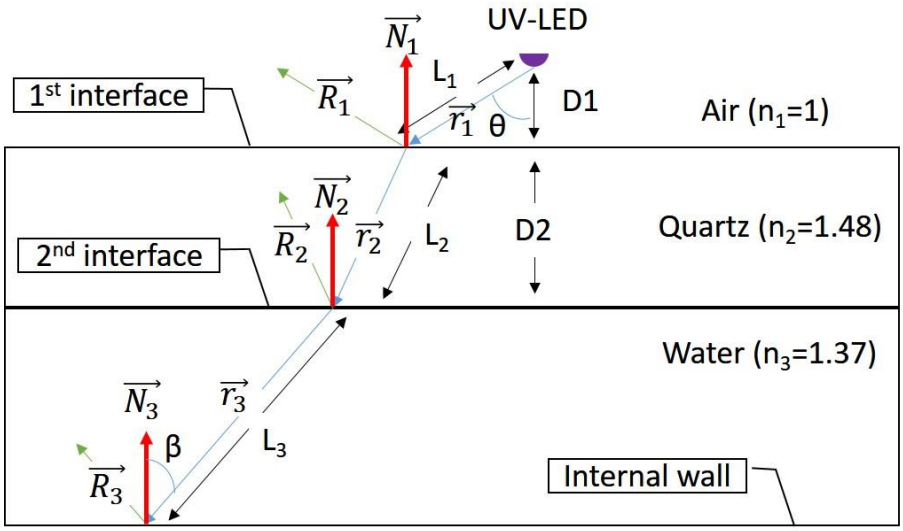

Figure 9. Schematic description of refraction and reflection at air/quartz/water interfaces, where i=1, 2, and 3 point to air, quartz, and water, respectively. $\vec{r}_i$, $\vec{R}_i$, $\vec{N}_i$, and L_i are ray vector, reflected vector, the normal vector of the interface, and the travelled path lengths in the i^{th} medium, respectively. θ and β presents the emission angle and the incident angle on the internal wall, respectively. D1 is the distance between LED dye and the first interface, D2 is the thickness of the quartz sheet. In this study, D1 and D2 are 500 μm and 3 mm, respectively

In addition to the direct irradiation, reflected rays from internal walls contribute to the radiant energy field. When rays hit the reactor wall, a part of their energy is reflected back to the medium. The reflected beams bounce back, but they lose a great deal of their energy during the subsequent reflections. Thus the first reflection was considered in this study. In general, the energy is reflected specularly, diffusely, or a combination of both. Since there is not an external UV source that adds to the reflected energy from the walls at the boundaries, the intensity of reflected light, $I_{reflection}$, can be written as:

$$I_{reflection} = (\alpha_{diffuse})I_{diffuse} + (1 - \alpha_{diffuse})I_{specular} \qquad (7)$$

where $I_{diffuse}$, $I_{specular}$, and $\alpha_{diffuse}$ are the intensity of diffusely reflected radiation, the intensity of specularly reflected radiation, and the diffuse coefficient of reflective surface, respectively. The diffuse coefficient relates to the characteristics of the material of the reactor. For transparent material, the amount of specular reflected energy is calculated according to Fresnel's law, and the direction of a reflected ray ($\vec{R}_3$) is determined using Equation 8. As for the diffuse reflection, the diffusely reflected energy is obtained by dividing the radiant power by π [63] and uniformly spread across the space.

$$\vec{R}_3 = \vec{r}_3 - 2(\vec{r}_3.\vec{N}_3)\vec{N}_3 \quad (8)$$

2.2.2 The absorption coefficient of quartz

Since the transmittance of commercial grade quartz changes over the so-called germicidal range (200–280 nm) and UV-LED is a polychromatic UV source [36], the weighted average of quartz UV Transmittance (UVT) was used in calculations.

2.3 Strategy to implement the radiation model

ANSYS 18.2 simulation package was used to build and discretize the problem domains of the UV-LED reactor via 742539 hexahedral meshes. Since simulation using 2259416 hexahedral meshes had negligible impact on the irradiance and radiant energy distribution, the simulation results were assumed to be mesh independent. To implement the radiation model, the normal vectors of the computational cell which lie on the quartz-water interface and the internal wall surfaces were captured and stored in the memory. Next, ray vectors were generated and the radiant energy field across the reactor, as well as the irradiance on the internal wall surfaces, were calculated and stored in user-defined memories. The angle between the incident ray and the normal vector of the quartz-water interface was used to calculate refracted ray. Since the quartz was not part of the numerical domain, all the relevant calculations to air-quartz interface and quartz

absorption were included in the user-defined function. The irradiance and the direction of the incident ray along with the reflection properties of the internal wall surface were utilized to calculate the irradiance and/or fluence rate derived from the reflected rays. The stored normal vectors of the internal wall surfaces were used to calculate the inverted ray vector during the specular reflection. In the end, the sum of the direct irradiation and the reflected irradiation was reported as the total irradiance. All the aforementioned steps were programmed and implemented using user-defined functions.

2.4 Experimental methods

2.4.1 Characterization of UV-LEDs

Four UV-LEDs with the balloon shape radiation profile but slightly different emission spectra and various power outputs (Figure 10) were selected for irradiating the reactor. The UV-LEDs radiant flux was measured using a custom-designed holder, securing the LEDs at 5/8" input port of a calibrated 2" integrating sphere (IC2 StellarNet Inc.). The integrating sphere was operated at 10 ms integrating-time at 200–400 nm collecting wavelength, coupled to a spectrometer (StellarNet Inc. BLACK-Comet UV-VIS) via a Sub-Miniature Assembly (SMA) fiber optic.

The UV-LEDs' outputs were measured at 350 mA and 400 mA using the integrating sphere. The outputs of LED1–LED4 at 350 mA and 400 mA were 12.0, 6.2, 8, 15.3 mW and 12.9, 8.6, 9.3, 16.4 mW, respectively. Considering the UV-LED's power-current relationship, which was provided by the manufacturer, each UV-LED's output at the current of interest (e.g., 375 mA) was calculated by interpolation of the measured values.

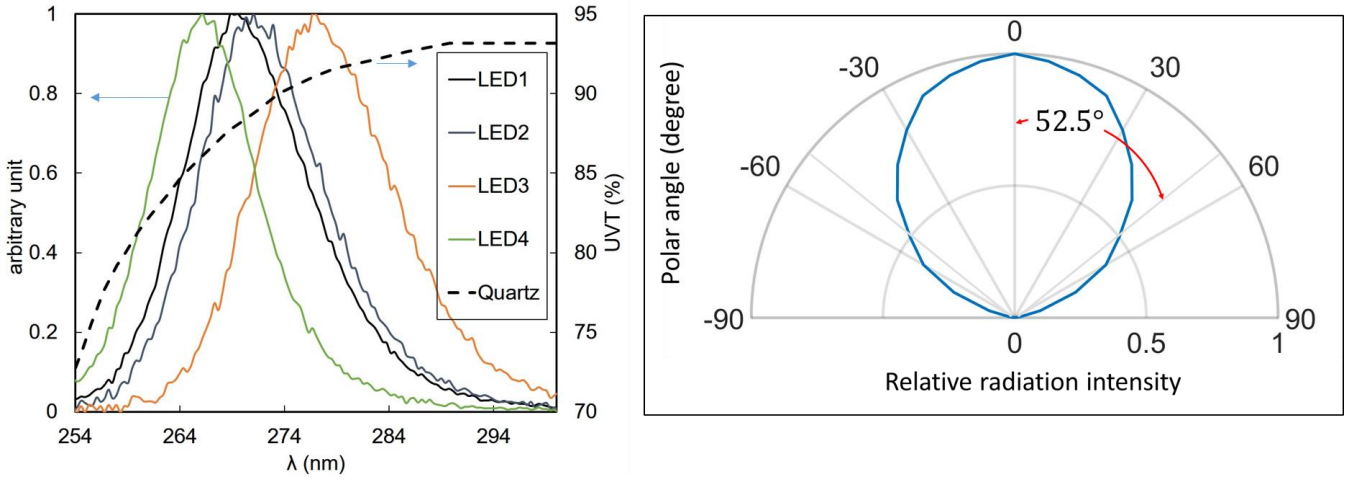

Figure 10. Left: UV Transmittance of the commercial grade quartz changed over the emission spectra of the four UV-LEDs. The UV-LEDs have different peak wavelengths ranging from 265 nm to 275 nm. Right: the balloon shaped relative radiation profile of the UV-LEDs with a half viewing angle ($\theta_{1/2}$) of 52.5˚.

2.4.2 UV-LED reactor geometry and operation

The UV-LED reactor consisted of a 5-cm plexiglass pipe with a length of 17-cm to incorporate four UV-LEDs, which were in a row and 3.175 cm apart from each other (Figure 11). The UV-LEDs were separated from the water using a 3-mm-thick commercial grade quartz sheet (Technical Glass product, Inc.). In order to accurately install UV-LEDs on the intended place, a 3D printed holder was used. To effectively control the temperature of each UV-LED during the operation, the heat dissipation was managed using a combination of a thermoelectric cooler, a heatsink, and a fan (Figure 11).

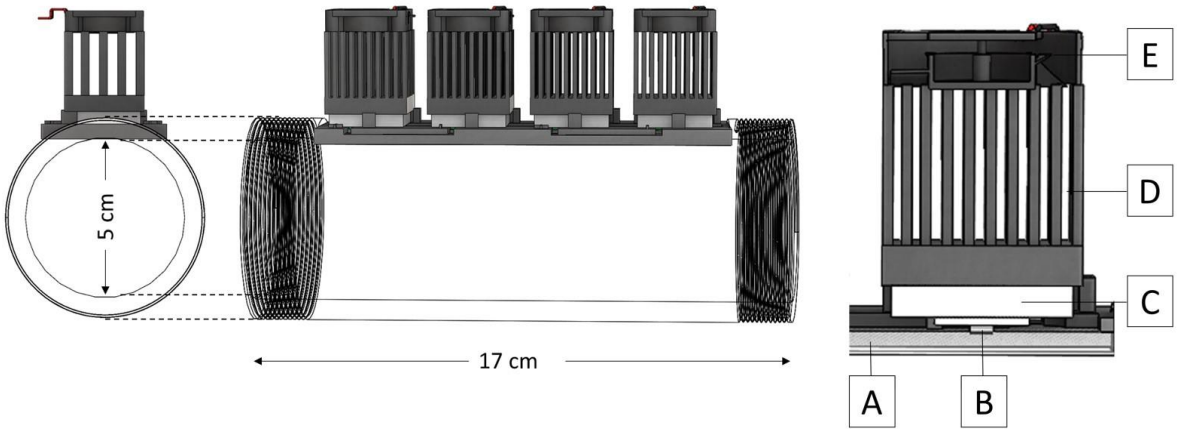

Figure 11. Left: the schematic of the side view of the cylindrical plexiglass UV-LED reactor incorporating four UV-LEDs. Right: a close view of the longitudinal cut of a UV-LED reactor illustrating quartz (A), UV-LED (B), a thermo-electric cooler (C), heatsink (D), and fan (E).

2.4.3 UV visualization using photoluminescence processes

The investigation of irradiation distribution with high resolution requires a detector with a small surface area and precise apparatus, which is not always available. In addition, measuring the irradiance for a large number of points in a reactor is time-consuming. Using a photoluminescence process, UV distribution over a large area can be captured fast with high resolution. Another advantage of this technique is its usefulness for identifying the dark area with minimum resources.

The typical white paper was found to exhibit the properties similar to those of a fluorescent material that absorbs UV radiation and re-emits blue light. As a qualitative method of irradiation assessment and to visualize the overall radiation pattern inside of the reactor, a white paper was put on at Z=0 cross section (Figure 12) to capture a full picture of irradiance distribution. Furthermore, using Rhodamine WT (CAS 37299-86-8), a fluorescent chemical, UV radiation in water was visualized to be used for qualitative irradiation model assessment.

2.4.4 Irradiance measurement using radiometry

The irradiance on the axis of the reactor was measured by a spectrometer (Ocean Optics USB 2000+ UV/Vis). Figure 12-A shows a schematic of the setup including the placement and direction of the optical fiber. The detector was equipped with an optical fiber to have better access to the inside of the reactor. To account for the incident angles, a cosine corrector diffuser with 180˚ viewing angle (CC-3-UV-S, Ocean Optics) was installed on the optical fiber (Figure 12-B). To move the detector inside the reactor, the detector was held tightly by two clamps mounted on a non-reflective rod secured on a manual lab jack. The jack was mounted on a single axis translation stage with 2 mm resolution. Due to the limitations of the setup, the optical fiber could not reach the end of the reactor to measure irradiance over the entire axis. Therefore, to measure the irradiance on the entire axis of the reactor, the detector was used in forward and backward modes. In the forward mode, the detector moves from Z=0 toward Z=17 cm (Figure 12-C), and the opposite was the case for backward mode (Figure 12-D).

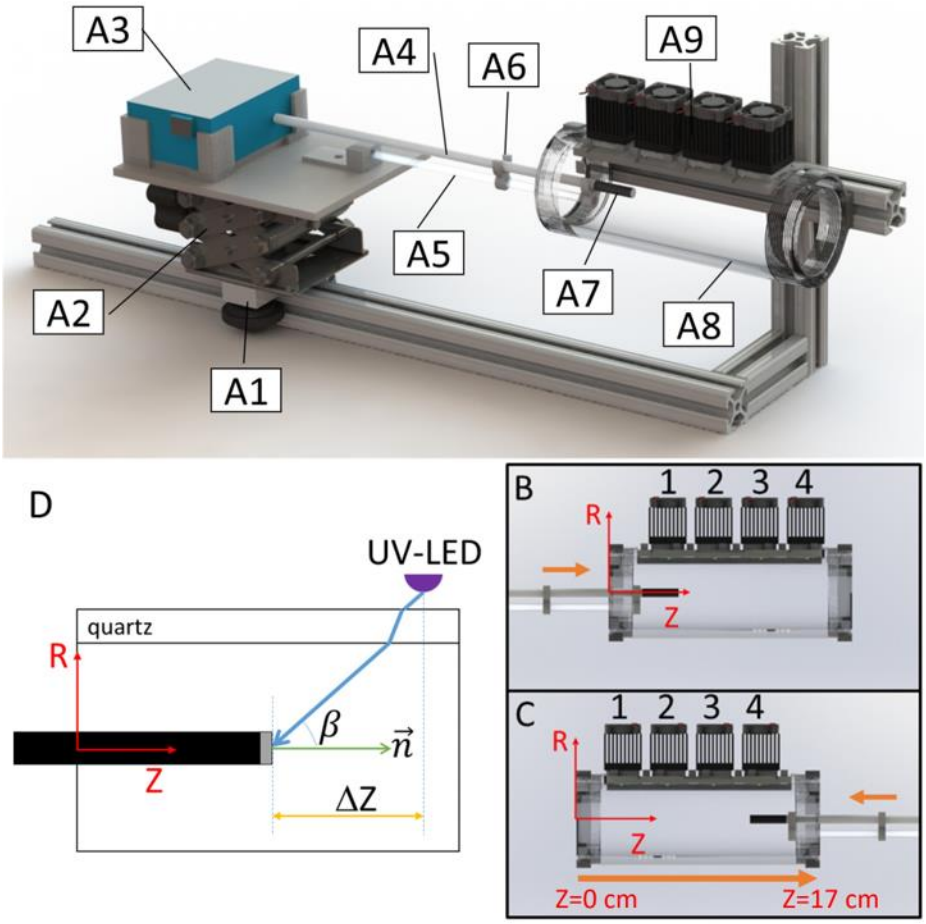

Figure 12. (A) the setup for irradiance measurement on the axis (i.e., R=0) of the UV-LED reactor where A1 is a single axis translation stage, A2 is a manual lab jack, A3 is a spectrometer, A4 is optical fiber, A5 is non-reflective rod, A6 is a clamp, A7 is a cosine corrector, A8 is the body of UV-LED reactor, A9 is UV-LED package. $\vec{n}$, β, and ΔZ in (B) represent the normal vector of the cosine corrector, the incident angle on the cosine corrector, and longitudinal distance from the UV-LED, respectively. In the forward mode (C), the detector moved from the Z=0 cm toward Z=17 cm. In the backward mode (D), the detector moved from Z=17 cm toward Z=0 cm.

2.5 Results and discussion

2.5.1 Energy loss due to reflection at the interfaces

The magnitude of reflectance from the first and second interfaces are different. The amount of energy loss due to reflectance depends on the distance of LED from the quartz sheet, the

refractive indices of the media, and the radiation profile of UV-LED. The most important factor is, however, the distance between LED and the quartz sheet, in a sense that the farther UV-LED gets, the less energy is lost due to reflection. UV-LEDs are typically very close to the quartz window to harvest all the photons for the inactivation. Given the size of UV-LEDs, the UV-LED chip is ~500 µm (the distance that has been chosen for this study) away from the quartz sheet. The minimum amount of reflections from the first and second interfaces are 4%, and 0.2% which means, at best, 4.2% of incoming energy is wasted due to reflection.

Table 2 shows the normalized average fluence rate inside the reactor in three different scenarios. In the first scenario, the effect of reflectance was not included, and the average fluence rate ($\overline{E}_0$), was chosen as the basis for the comparisons. In the second scenario, only the effect of the first interface was considered. As for the last scenario, the reflectance from both interfaces was taken into consideration. As seen (Table 2), the amount of the fluence rate dropped 6% after including the reflection from the first interface (R1). Due to a significant difference between air and the quartz refractive indices and large incident angles, most of the radiant energy is lost at the first interface. Once the reflection from both interfaces was considered (the third scenario), the delivered fluence rate further dropped, and the overall radiant energy loss reached 7%. Note, the attenuation of radiation energy due to the absorption in all the scenarios were the same. The amount of energy loss can be different for UV-LEDs with different radiation profile. According to Fresnel's law, the beams with larger incident angles lose more energy due to the reflection. This means that UV-LEDs with wide viewing angle lose more energy due to reflection compared to those with narrower ones.

Table 2. The normalized average fluence rate inside the reactor in three different scenarios.

$\overline{\mathrm{E}}_0$	1.00
$\overline{\mathrm{E}}_0 \times (1 - R_1)$	0.94
$\overline{\mathrm{E}}_0 \times (1 - R_1) \times (1 - R_2)$	0.93

2.5.2 UV absorption of the quartz

The quartz weighted UVT for LED1, LED2, LED3, LED4 were 88.1%, 88.7%, 90.7%, 85.9%, respectively. If the UVT at the peak wavelength of each of the LEDs is selected, LED1–LED4 exhibit UVTs of 88%, 88.5%, 91%, and 86%, respectively. The results show that the monochromatic assumption for the UV-LEDs posed negligible difference, so for the practical application, it is recommended to select the UVT at the peak wavelength of UV-LED.

The absorption of UV in the quartz relates to its thickness and UVT. The thickness of the quartz windows is about few millimeters, and considering the reported UVT (85%–91%) of commercial grade quartz, the overall UV absorption within the quartz is a small amount. Given that, it is recommended to select an averaged UVT for a UV-LEDs from a narrow emission range (~10 nm) for practical application. In fact, including the variation of UVTs in radiant energy calculations adds up to the complexity of the modeling without significant effects. However, if the peak wavelength of UV-LED fall below 240 nm, the effect of quartz's UVT becomes significant. For example, the UVT of quartz for a 254 nm UV-LED (73%) is significantly different from that of a 285 nm LED (92%).

2.5.3 Irradiance assessment qualitatively

To assess the capability of the radiation model in predicting the radiant energy field inside the reactor experimental studies were performed. In the first set of experiments, the radiation distributions in air and water were separately studied. In order to capture the light distribution on

the reactor wall, a white paper was rolled and covered the internal wall of the reactor. The bright region in Figure 13 shows the captured UV radiation on the white paper. UV-LED shined all the lateral cross section, and no dark area was seen (Figure 13-A1). The radiation distribution in water, however, was different from that of in the air. Figure 13-A2 and Figure 13-A3 show the radiation distribution of LED1 on lateral and longitudinal cross sections of the reactor in water, respectively. As seen, there is a distinct boundary between bright and dark areas (Figure 13-A2), and the captured pattern looks like a cone with the angle of ~40°. The captured pattern illustrates that the UV-LED radiation profile shrinks in water, and there is almost no light beyond 40°. This happens because of the refraction at the air-quartz interface. Additionally, at larger polar angles, due to more reflection at the air-quartz-water interfaces (due to Fresnel's law) along with less emitted UV rays, regions beyond the dash lines appear darker. As seen in Figure 13-A2 and Figure 13-A3, light intensity around the normal axis of UV-LED is higher compared to larger polar angles, and this aligns with the UV-LED's balloon shape radiation profile (Figure 10).

Figure 13-B1–Figure 13-B3 show the simulated radiation distribution in the air and water on the lateral and longitudinal cross sections of the reactor. As seen, the prediction of the cone of radiation, the attenuation of the radiation energy, and the dark area agrees well with the visualized pattern. According to Snell's law, the maximum refracted angle at the quartz-water interface is 47° which is higher than the experimental value (i.e., 40°) indicating that low energy rays may not be entirely visualized by this method in water.

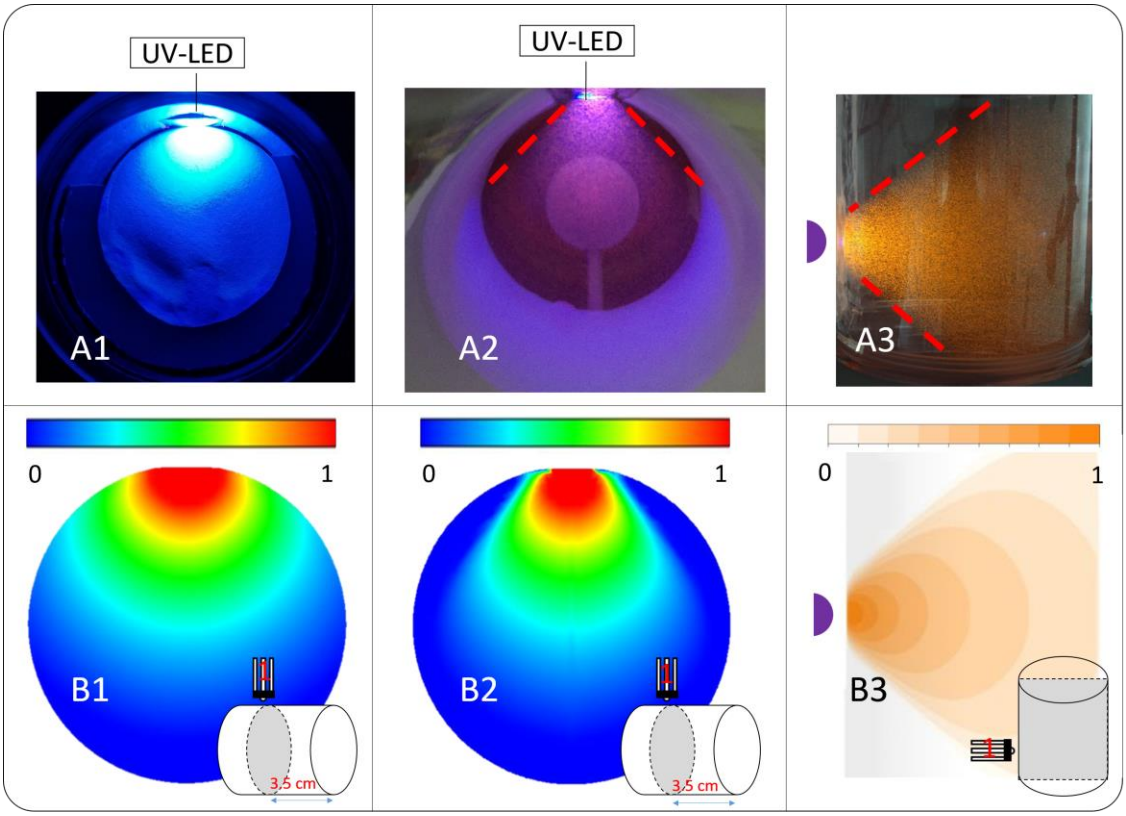

Figure 13. A1 shows the captured pattern on the white paper covered the lateral cross section of the pipe (Z=3.5 cm) without the presence of water. A2 and A3 show, in turn, the visualized UV pattern at lateral (Z=3.5 cm) and longitudinal cross sections in water using Rhodamine WT. B1–B3 are the simulated normalized radiation distributions that pertain to A1–A3, respectively.

Another set of experiments were performed to study the effect of reflection on the radiation distribution. Figure 14-A illustrates the radiation distribution of LED1 on the lateral cross section of Z=0 cm. Figure 14-A clearly shows that the radiation pattern is symmetric about R-axis, the central part is lighter, and there is a dark arc in the areas closer to LED1 (on top of the pipe). In Figure 14-B, a double-arc shape lit area is also seen; which is a result of specular reflection. Once the reactor's internal wall was covered by an absorptive material, the double-arc pattern disappeared. Figure 14-A2 and Figure 14-B2 show the irradiance distribution in grayscale where black color points to the darkest area and white color shows the brightest points. As seen the

simulated irradiance (Figure 14-A3 and Figure 14-B3) agree well with the captured light patterns (Figure 14-A2 and Figure 14-B2). The position and breadth of the dark arc and lit heart shape were predicted successfully indicating the capability of the irradiation model. Note, since the paper had roughness causing shadowing effects, the visualized pattern was not as smooth as the simulation results. It should be noted that the radiation pattern was captured once the reactor was empty. If the reactor is filled with water, fewer UV rays will reflect back (Fresnel's law) because the refractive indices of water (1.37) and plexiglass (1.5) are close to each other.

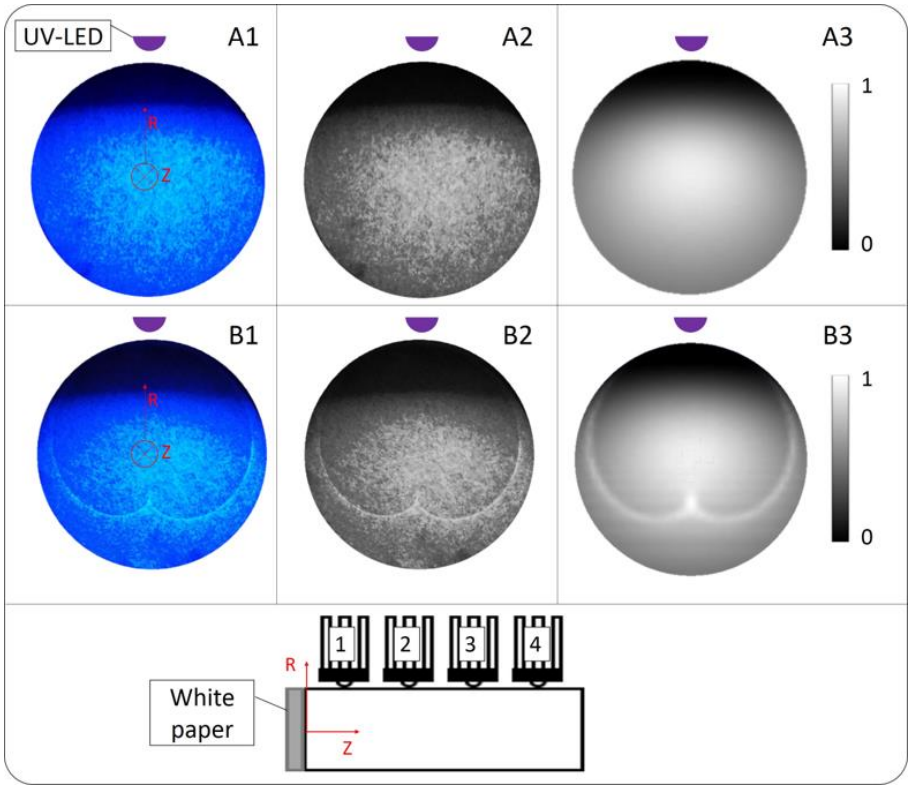

Figure 14. The light distribution on the lateral cross section (i.e., Z=0 cm) without (top) and with (bottom) the internal wall reflection when LED1 was operating. The Z axis lies on the center of the pipe and its direction is inward. UV-LED is shown on the top of the pipe using a half-circle. The processed image (B) and simulated irradiance distribution (C) are shown light distribution in a gray scale.

2.5.4 Irradiance assessment quantitatively

UV visualization using a photoluminescence process was an easy way to evaluate the radiation predictions; however, an accurate method is still required to quantify the error of prediction. The radiometry is a reliable technique that is commonly used for irradiance measurement. As seen earlier, in the photoluminescence process low energy beams cannot be detected, but radiometry can differentiate UV radiation energy to higher degrees. To evaluate radiation model, irradiance on the axis of the reactor was measured using the radiometer.

2.5.4.1 Comparison of the simulated and experimental irradiance on the axis of the reactor

Figure 15 presents the simulated and experimental irradiance distribution of each UV-LED on the reactor axis where the horizontal axis presents the longitudinal distance from the UV-LED's normal axis (i.e., ΔZ in Figure 12). As seen in Figure 15, at zero longitudinal distance the irradiance reaches zero due to the incident angle of 90°, but it increases sharply and grows to its maximum around ΔZ=1.5 cm. Next, the irradiance initially drops fast and then gradually reaches small values at farther distances. This fast increase and decrease near the UV-LED were observed because the incident angle of rays on the detector change sharply near UV-LED, where a high density of photons existed.

Since the UV-LEDs had different radiant powers, their maximum irradiances varied between about 90 $\frac{\mu W}{cm^2}$ and 250 $\frac{\mu W}{cm^2}$. Figure 15 shows that the variation of irradiance over the axis for each individual UV-LEDs successfully captured by simulation. The predictions agreed well with the measurements at farther distances; however, a deviation from the simulation is observed at the distances closer to the peak of irradiance distributions; the deviations grow further for more powerful UV-LEDs such as LED1 and LED4. There are two reasons for the deviations. First, the

simulation represents local irradiance, whereas the detector measures the average of collected irradiance over the detector surface area. Since there was an irradiance distribution over the detector surface area, the effect of the detector size on the error of measurements increased as it approached to a UV-LED. Irradiance measurement at close proximity of a UV source come with relatively larger errors especially in a nonparallel radiation field [64], which is the case in this study. Second, the inaccuracy of the orientation of the detector at closer distances to UV-LED could increase the error of the measurements. A tilted detector could measure a markedly different value at the closer distances to UV-LED, where the density of photons in the space was higher than the farther distances and the effect of incident angle is more important.

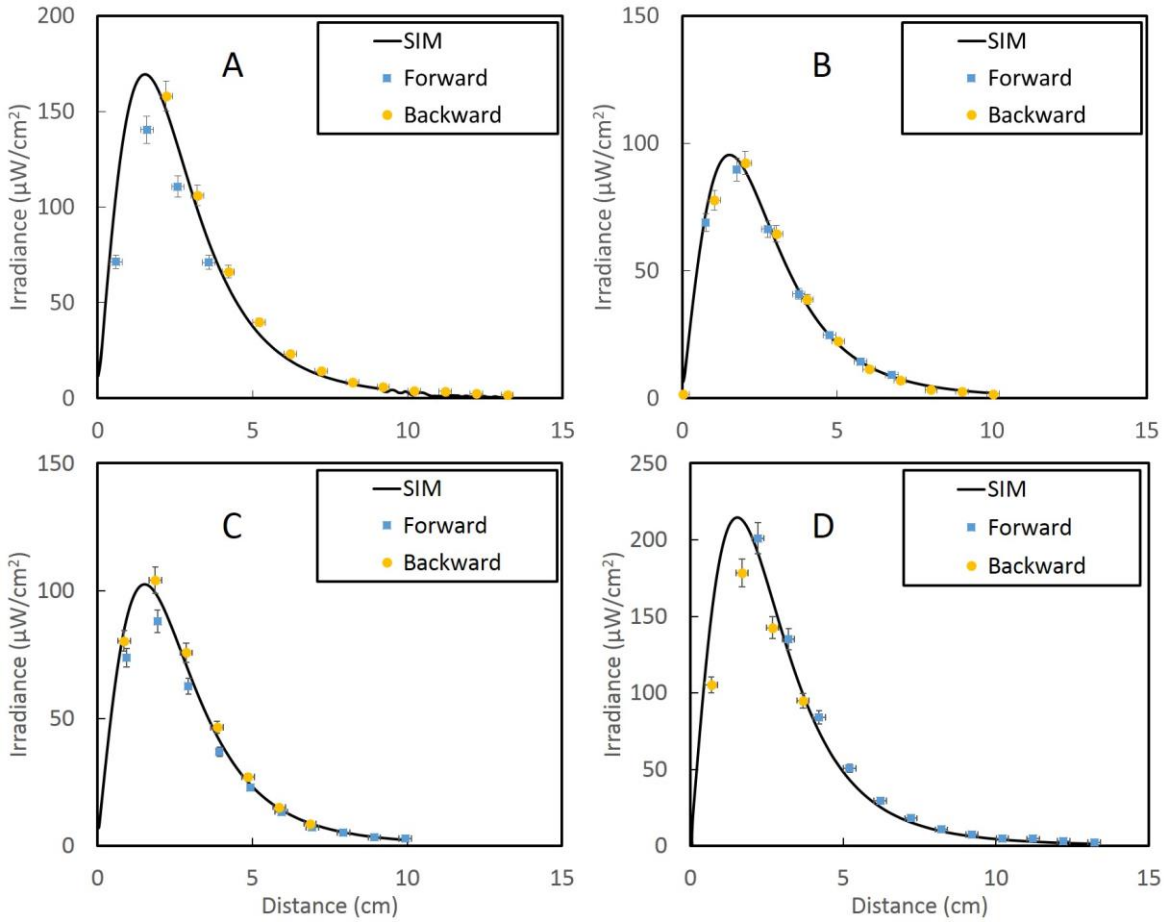

Figure 15. Irradiance measurements in the Forward and Backward modes along with the simulation predictions on the axis of the reactor. The x-axis shows the longitudinal distances from UV-LED, and the error bar shows the standard deviation of three independent tests. A–D correlates with LED1–LED4 in chronological order. At the longitudinal distance of 0 cm, the detector's surface (which is normal to the LED normal axis) is positioned under LED center (i.e., incident angle=90°), and as a result, the detector does not receive any radiation.

In flow-through UV-LED reactors, more than one UV-LED is typically used to inactivate microorganisms (e.g., [19, 36, 37, 45]), so an irradiation model should be able to simulate the combined effect of all UV-LEDs reliably. To assess the accuracy of the simulations further, the irradiance of all UV-LEDs on the axis of the reactor was measured in backward mode.

Figure 16 presents the experimental and simulated irradiance distribution on the axis of the reactor when all of the UV-LEDs were operating. Vertical lines also show the approximate position of the UV-LEDs on the horizontal axis. As seen, there are four peaks along the axis, and the highest peak happens after LED4 (the most powerful UV-LED) at ~Z=14.5 cm. Since LED4 is in front of other UV-LEDs, the first peak from right presents the combined irradiance of all UV-LEDs (given the detector direction and orientation). The trend of fluence rate along the axis shows that the fluence rate sharply falls after each peak and its minimum amounts coincide with the LEDs' locations. This happens because the angle between the normal detector surface and LED's normal vector becomes 90° when the detector lies under the LED. Taking the orientation of the surface of the detector into consideration, the detector could not receive any radiation at Z<3.5 cm. This agrees with simulation prediction. As seen, the radiation model could successfully predict the rise and fall of the fluence rate, the magnitude of peaks, and the positions of the inflection points across the axis. The close agreement between experimental and simulation results shows the capability of the proposed model to predict irradiance where multi UV-LED is used.

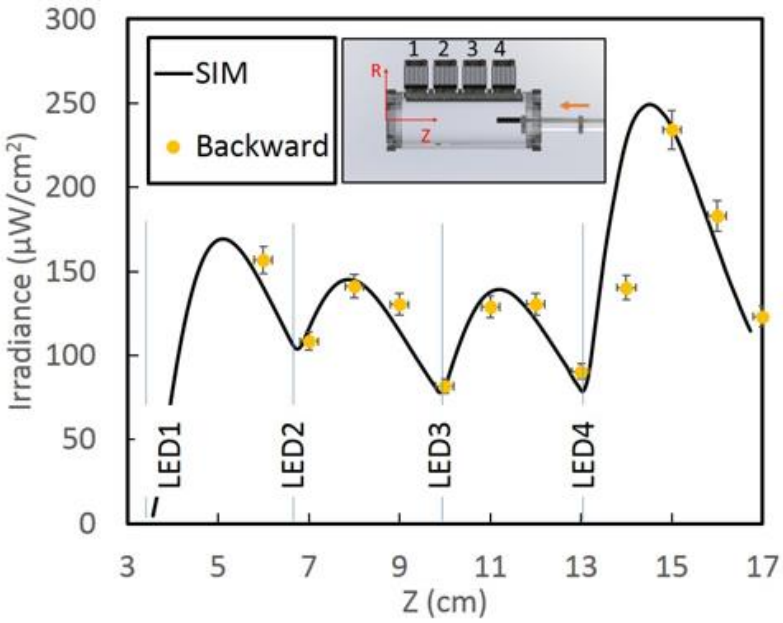

Figure 16. The distribution of the experimental and simulated irradiance in the backward mode on the axis of the reactor when all UV-LEDs were operating. The error bars show the standard deviation of three independent tests. Vertical lines on the Z-axis show the approximate positions of LEDs.

2.6 Summary

In this study, a numerical method was proposed for modeling the radiant energy field in a UV-LED reactor. The effect of refraction, reflection, and absorption, as well as the reflection from relevant surfaces, were considered in the radiation modeling. It was shown that UV energy is partially wasted due to reflection at air/quartz/water interfaces, and the larger the viewing angle becomes, the more energy is wasted. Compared to reflection, the impact of the refraction phenomenon was more significant so that the UV-LED radiation distribution shrunk in water and became different than that of in the air. It was found that UV-LEDs can be assumed as a monochromatic source for quartz UVT calculations. In addition, the quartz had a negligible impact on the emission spectrum of UV-LEDs. The study showed that 7% of UV energy is wasted to air and quartz and do not contribute to the radiant energy field when all the attenuating factors are

taken into account. In this study, UV visualization was employed as a convenient and fast method for capturing the UV-LED radiation profile. This approach allowed identifying the radiation profile in the water, which is not possible using a radiometer.

Chapter 3: UV-LED fluence rate determination by numerical and experimental methods for microbial inactivation studies

3.1 Introduction

As explained earlier, the simulation of a UV reactor entails the integration of three main phenomena hydrodynamics, radiation, and kinetics. Among all, the kinetics of microbial inactivation is necessary for the evaluation of the UV reactor. The performance of a UV reactor is assessed using a biodosimetry test. Biodosimetry is a procedure through which the delivered fluence (dose) to microorganisms is measured [6]. In this procedure, the amount of microbial inactivation during a UV process is measured and then converted to the fluence (dose) using the organisms' fluence-response curve [6]. Given that, the reliable fluence-response curve (kinetics data) are immensely important for the evaluation of UV reactor's performance.

The differences between UV-LED and Low-pressure UV lamps were discussed in Chapter 1. In short, UV-LEDs are polychromatic radiation sources that offer various emission wavelengths and radiation profiles [36]. These features make UV-LEDs different from low-pressure UV lamps. Due to the differences between UV-LEDs and UV lamps, the protocol that is currently used for UV lamps [53] cannot be directly applied to UV-LEDs. According to the protocol, quasi-collimated beams of a UV lamp are applied to the surface of a petri dish (containing microbial suspension), and the fluence rate inside the microbial suspension is calculated considering irradiance at the water surface and the four correction factors[1]. Typically, a UV lamp is placed 20 cm or farther normal to a Petri dish to achieve collimated beams. Since UV-LEDs

[1] These factors are petri factor, divergence factor, water factor, and reflection factor which account for the collimation of beams, divergence of beams, the UV absorption of the microbial suspension, and the reflection from the surface of the water, respectively.

have low output, they cannot replace UV lamps in the collimated beam apparatus. To overcome the low intensity of radiation, UV-LEDs have been placed closer to the petri dish [50], or a large number of UV-LEDs have been used [19, 46]. In such studies, either a simplified UV-LED's radiation profile has been used [39], or the correction factors were not carefully employed [50]. Almost all the proposed and developed methods have tried to apply Bolton's method [53] to UV-LEDs to calculate fluence rate in a petri dish. For example, the recent study showed that placing a typical UV-LED 13 cm away from the water allows applying the correction factors [25] safely. Despite reasonable collimation, low fluence rates (one-tenth of the typical value which is typically observed for LP UV lamps) were obtained at such distance. To overcome the low fluence rate, Kheyrandish et al. [22] suggested the increase the number of UV-LEDs at farther distances or the development of a reliable radiation model to predict the fluence rate inside a Petri dish in shorter distances. There are, however, some concerns associated with using multiple UV-LEDs. UV-LED technology is not mature yet, and the emission spectrum of the produced UV-LEDs cannot be guaranteed. UV-LEDs from the same batch may have different emission spectra which lead to different kinetic rate constants. Therefore, the results of such experimental setups should be used cautiously. A reliable radiation model can be used for fluence rate determination, and yet such an approach has not been implemented.

This chapter aims to apply the evaluated radiation model developed in Chapter 2 to determine the fluence rate inside a petri dish. This technique calculates the fluence rate regardless of UV-LED position and the geometry of the container. The precision of the radiation model on the water surface was assessed by radiometry and Iodide-Iodate chemical actinometry when the UV-LEDs were operating at two different forward currents. Further, the delivered fluence rates to the microbial suspensions (*Escherichia coli* (ATCC 11229) and MS2 (ATCC 15597-B1)) were

calculated in different operating conditions and were compared with the numerical predictions. The aim of such comparison was to test if by using the germicidal factor and the 254 nm fluence-response data, the kinetic rate constants of microorganism can be estimated. The results showed that deriving germicidal factor based on the action spectra and emission spectrum of UV-LED leads to the calculation of the acceptable kinetics rate constants.

3.2 Material and methods

3.2.1 Characterization of UV-LEDs

Table 3 shows the specifications of the UV-LEDs used in this study, based on the manufacturer's datasheets. The UV-LEDs with heart-shaped radiation profiles (Figure 17-A) and the nominal wavelengths of 265 nm and 275 nm were chosen to assess the accuracy of the irradiation model. The UV-LEDs of such peak wavelengths have frequently been used for water disinfection studies [16,38,39,43,50,65], and their microbial inactivation kinetics are of interest.

Table 3. UV-LED specifications along with the relevant weighted average quantities

	Parameter	LED-1	LED-2
Manufacturer datasheet	λ_{peak} (nm)	265	275
	P_o (mW)	10	8
	$2\theta_{1/2}$	130	124
Weighted average quantities	$\overline{GE}_{B.\ Subtilis}$	1.11	1.02
	$\overline{GE}_{E.coli}$	1.21	0.89
	$\overline{GE}_{MS2}$	1.11	0.87
	$\overline{U}$ (MJ/Einstein)	0.446	0.432
	Quantum Yield ($\overline{\Phi}$)	0.53	0.40

Unlike LP UV lamps, the UV-LED emission spectrum (Figure 17-B) indicated that UV-LED is not a quasi-monochromatic UV source. Figure 17-B shows the microorganisms' action spectra, the quantum yield (Φ_λ) of the actinometry solution [66], and the energy carried by one mole of photons (einstein), U_λ, change over the UV-LED's emission spectrum. In order to improve the prediction of UV-LED's effect on the aforementioned quantities, the weighted averages were calculated [55]. To obtain weighted germicidal efficiency, $\overline{GE}$, the LED's relative emission spectrum and microorganism action spectrum were considered. The microorganism action spectrum, G_λ, was defined as the biological photoresponse (i.e., germicidal effectiveness) of photons of wavelength λ relative to those at 253.7 nm. In this view, $\overline{GE}$ determines how effective a UV-LED is against microbial inactivation compared to an LP UV lamp (253.7 nm). To calculate the $\overline{GE}$ of each LED (Equation 9), the integral of the convolution of the UV-LED spectral power distribution (P_λ) and the microorganism action spectrum (G_λ) was computed and then divided by the integral of the UV-LED spectral power distribution. Similarly, when U_λ and Φ_λ separately substitutes G_λ in Equation 9, the weighted average of energy/einstein ($\overline{U}$) and quantum yield ($\overline{\Phi}$) is obtained, respectively.

$$\overline{GE} = \frac{P_o}{P} = \frac{\int_{\lambda_1}^{\lambda_2} P_\lambda * G_\lambda \, d\lambda}{\int_{\lambda_1}^{\lambda_2} P_\lambda \, d\lambda} \qquad (9)$$

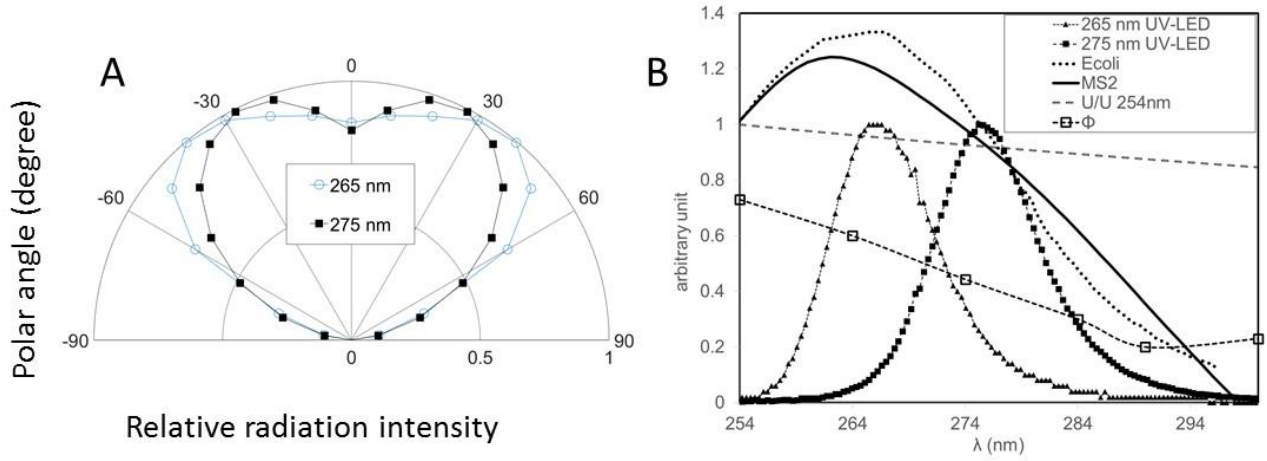

Figure 17. The radiation profiles of the UV-LEDs (A). The action spectra of MS2 and *E. coli,* the quantum yield of the chemical actinometry, and the energy of one mole of photons/the energy of one mole of 254-nm photons (U/U_{254nm}) change over the UV-LEDs emission spectra (B).

Typically, the LED's germicidal power, P_o, is the integral of the convolution of the LED spectral power distribution and *B. subtilis* action spectra [67] over the entire LED emission range. P_o cannot be used directly in radiation modeling because it does not show the radiant power of the UV-LED. The UV-LED radiant power, P, is the integral of the LED spectral power distribution over the entire LED emission range. In this regard, P_o is equal to P * $\overline{GE}_{B.Subtilis}$. Therefore, using the action spectra of *B. subtilis* [67] and the emission spectrum of each of the UV-LEDs, $\overline{GE}_{B.subtilis}$ and consequently P were achieved. Similarly, using the action spectra of *E. coli* and MS2 [68], the weighted germicidal efficiencies were calculated (Table 3).

3.2.2 Setup for irradiance measurement

Radiometry is a common method for irradiance measurement conducted on a flat surface [66]. The radiometer measurements were carried out with the spectrometer (Ocean Optics USB 2000+ UV/Vis) positioned at the liquid surface height of the sample being irradiated. To account for the incident angles, a cosine corrector diffuser with a 180˚ viewing angle (CC-3-UV-S, Ocean

Optics) was installed on the detector. The setup was placed in a black box to avoid detector saturation. For each measurement, the UV-LED of interest was mounted downward on a height-adjustable heat sink attached to the top part of the box. On the bottom of the box, the upward detector attached to an XY positioner was capable of measuring the irradiance distribution in a 5 cm × 5 cm square with 0.5-cm resolution (Figure 18).

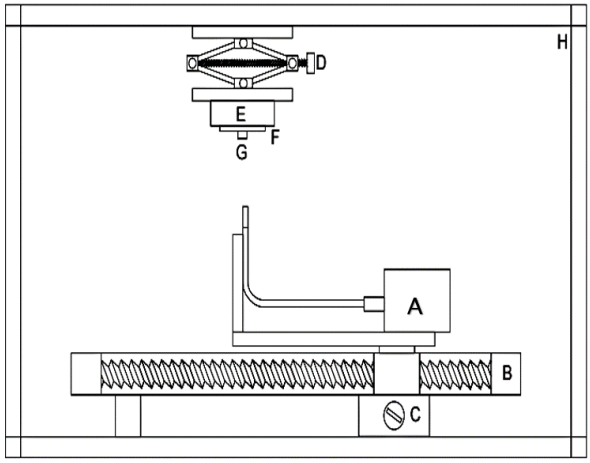

Figure 18. Setup for UV-LED irradiance measurement on the surface: (A) Ocean Optics USB 2000+ UV/Vis; (B) X positioner; (C) Y positioner; (D) laboratory jack; (E) heat sink; (F) LED circuit board; (G) UV-LED; and (H) black box.

3.2.3 Setup for microbial and actinometry experiments

Figure 19 shows the schematic of the experimental setup used for the microbial inactivation study. The UV-LED of interest was placed above the center of the petri dish, and its height was controlled by a translation stage with 100 μm resolution. The entire setup was enclosed in a black box to prevent any possible photoreactivation, and the irradiated samples were cultivated shortly after their exposure to minimize dark repair effects. The microbial suspensions were irradiated by two UV-LEDs of 265 nm and 275 nm, in two Petri dishes 5 cm and 9 cm in diameter, respectively, and the suspension was mixed during exposure. These Petri dishes are commonly used for

microbial inactivation studies. The water depths in the 5-cm and 9-cm petri dishes were 0.5 and 1 cm, respectively. The UV transmittance of the suspension was measured at the corresponding UV-LED's peak wavelength before each experiment by a spectrometer (Cary 100 UV-VIS), and each experiment was carried out in triplicate. The vertical distances of UV-LEDs from the water surface were chosen so that all the available photons in the viewing angle range got to the water surface. Since UV-LEDs had different viewing angles, for the 5-cm petri dish, the vertical distances for 265nm and 275nm UV-LEDs were 1.17 cm and 1.3 cm, respectively (e.g., the 265nm UV-LED vertical distance= $\frac{diameter/2}{\tan(\frac{130^\circ}{2})} = \frac{2.5\ cm}{\tan(65^\circ)} = 1.17\ cm$).

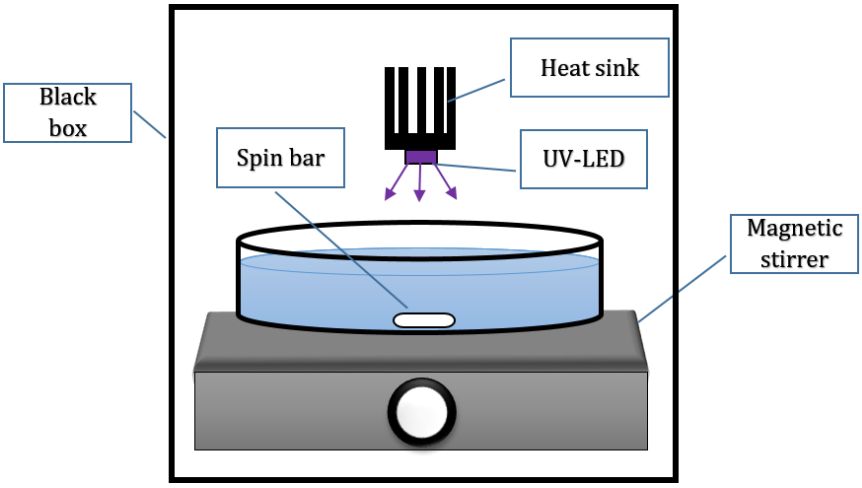

Figure 19. UV-LED bench-top setup for microbial inactivation.

Due to the high absorption coefficient of the KI/KIO_3 actinometry solution [66], all the UV radiation was absorbed in the first few microns of the solution surface. The solution is optically opaque to a wavelength shorter than 290 nm and blind to a wavelength longer than 330 nm [66], meaning that this solution absorbs UV radiation in the germicidal range, and ambient light does not have adverse effects on the measurements. Thus, the actinometry represents the fluence rate to the water surface and can be used for model validation.

The actinometry solution consisted of 0.6M KI, 0.1M KIO_3, and 0.01M $Na_2B_4O_7$ in 100-mL water [66]. Due to small variations in KI concentration, the molar absorption coefficient was selected as 27600 M^{-1} cm^{-1}. The fluence rate at the surface, $\overline{E_{0}}_{surface}$, was calculated using the following equation:

$$\overline{E_{0}}_{surface} = \frac{\frac{\left(A_{352}^{t} - A_{352}^{\circ}\right) * V}{\epsilon_{352}}}{t * S * \bar{\Phi}} * \bar{U} \qquad (10)$$

where A_{352}^{t}, A_{352}°, V, ϵ_{352}, t, S, $\bar{\Phi}$, and $\bar{U}$ are the absorption at 352 nm after the exposure, the absorption at 352 nm before exposure, the volume of the the solution, the molar absorption coefficient, exposure time, surface area of the Petri dish, weighted quantum yield, and weighted energy per einstein, respectively.

3.2.4 Kinetic data

E. coli (ATCC 11229) and MS2 (ATCC 15597-B1), as common bacterial and viral indicator organisms, were chosen for the biodosimetry experiments for three reasons. First, the availability of their 254nm UV fluence-response curves and the action spectra provided enough information to calculate the germicidal efficiencies. Second, their different UV sensitivities enabled the evaluation of the irradiation model in different UV fluences. Finally, these microorganisms are commonly used for reactor evaluation, and their kinetics will be helpful in future studies.

In this study, considering the action spectra, the weighted germicidal efficiency of each UV-LED was calculated (Table 3). By analyzing the kinetic data reported for *E. coli* (ATCC 11229) and MS2 (ATCC 15597-B1) by several researchers [69] using the collimated beam apparatus [53], the 254nm fluence-response curves of each microorganism were obtained

(Figure 20). For each log-inactivation on the curve, the corresponding fluence, along with its 99% confidence interval, was calculated. The lower and upper bounds (Figure 20) indicate the minimum and maximum possible log-removal (in the range of 1–5) for a given fluence.

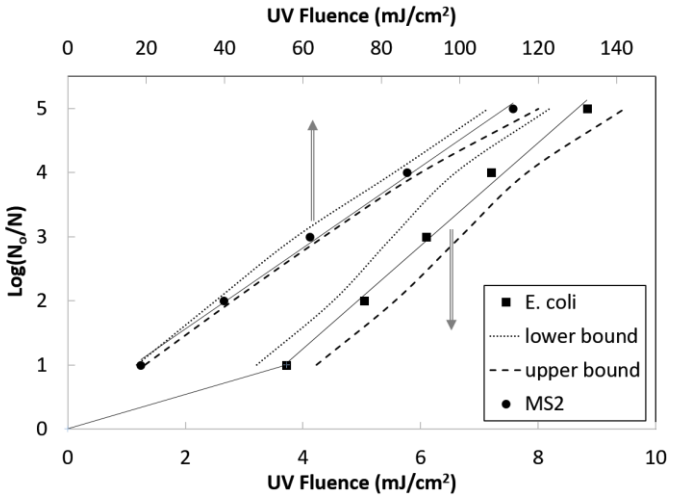

Figure 20. UV fluence-response curves of *E. coli* (ATCC 11229) and MS2 (ATCC 15597-B1) with their 99% confidence intervals were obtained by analyzing the kinetic data reported in the literature [69]. The markers indicate the average log-removal at any given fluence.

3.2.5 Microbial assays

3.2.5.1 *E. coli* preparation and enumeration

E. coli (ATCC 11229) was received as a frozen aliquot and was revived based on the manufacturer's guidelines. In the propagation step, one colony of the microorganism was detached from a freshly incubated lysogeny broth (LB) agar plate and added to 40 ml of sterile LB broth in a sterile 50-ml vial. The solution was incubated at 37°C and mixed at 200 rpm to ensure that constant oxygen levels were provided throughout the stock. Following overnight incubation, a 1-ml stationary-phase stock solution was mixed with 9 ml of fresh LB; then the solution was incubated again for 90 min to achieve its log-growth phase. The growth curves for the *E. coli* were developed based on the absorbance of the unwashed stock solution at 600 nm (OD 600) in order

to create a criterion to ensure that the sample was in its growth phase during the irradiation tests. The broth solution was washed in phosphate buffered saline (PBS) three times to achieve the concentration of around 5×10^6 CFU/ml for each experimental run. The enumeration of the tested microorganism followed a similar method to that of Cho et al. [70] Each exposed or unexposed sample was mixed and serially diluted. The dilutions were spread in triplicates on 90-mm LB agar plates. The plates were incubated in an inverted position for almost 12 h. Subsequently, spots in the range of 20–200 were counted.

3.2.5.2 MS2 preparation and enumeration

The method described by Shin et al. [71] was used for the preparation of phage stock solution. A 0.1-ml aliquot of MS2 (ATCC 15597-B1) and 1 ml of *E. coli* C3000 (ATCC 15597) as a host were spiked into 9 ml of LB broth. In order to improve the absorption ability of the host cells, 0.2 ml of $CaCl_2$ (1M) was added to the tube and the suspension was incubated at 37°C for 24 h. Then, the solution was centrifuged at 3300 rpm for 5 min. Next, the supernatant was filtered by using a 0.45µm low protein binding filter. The filtrate was collected and stored at 4°C as MS2 stock. For each experiment, the MS2 stock was diluted with PBS to achieve the initial concentration of around 10^6 PFU/ml. The double agar technique described by Adams [72] was used with some modification to do the infectivity assays. The bottom layer was prepared by adding 3 mm LB agar and cooled to room temperature. The exposed samples were diluted by adding 1 mL of suspension to 9 mL of fresh PBS at each step. The bottom agar was covered with 1 ml of each dilution followed by a 3-mm mixture of an upper agar layer and *E. coli* C3000 (ATCC 15597). After overnight incubation, the plaques were counted.

3.2.6 The procedure of numerical modeling

The radiation model was described in details in Chapter 2. Briefly, UV-LED was modeled as a directional point source with a specific radiation profile. The propagation of UV rays was modeled by considering the refraction and reflection at the first interface along with the absorption in the water. In addition, the specular reflection from the second interface was included in the fluence rate determination.

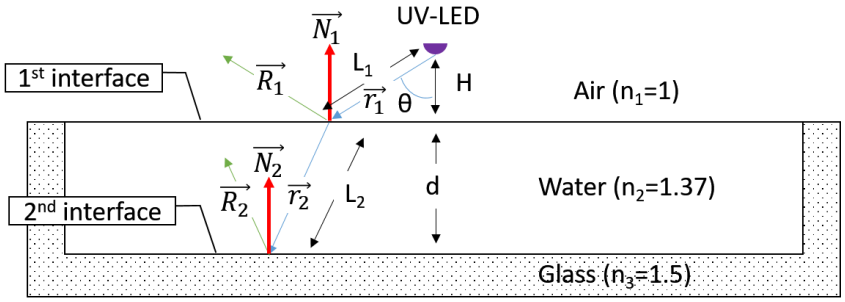

Figure 21. Typical UV-LED microbial inactivation setup. H is the distance between the UV-LED and the water surface, d is the water depth in a Petri dish, $\vec{r}$ is the direction of UV ray, $\vec{R}$ is the reflected UV ray, $\vec{N}$ is the normal vector of the surface, and the subscript points to the medium number.

The water refraction index, n_λ, depends on the emission wavelength [73]; however, due to small changes in the range of 254–285 nm (<1%), 1.37 was selected as n_{water} for the simulations. It was also assumed that the water-air interface was flat. At the water-glass interface, part of the UV light is transmitted and absorbed by the glass and the rest is reflected back to the water specularly. The amount of reflected energy was calculated using Fresnel's law and the direction was found using Equation 8 in Chapter 2.

3.2.7 Numerical modeling of the system

In completely-mixed conditions, it was assumed that all the microorganisms would receive the average fluence rate during the exposure time. After obtaining the fluence rate distribution

inside the reactor, the area-weighted average value was computed and reported as the delivered fluence rate.

ANSYS Fluent simulation packages were used to build and discretize the problem domains. The numerical domains of the 5-cm and 9-cm Petri dishes were discretized into 33340 and 51870 structured hexahedral cells, respectively. A user-defined function was developed to compute the fluence rate for each cell centroid. It was observed that doubling the cell numbers had a negligible impact on the delivered fluence rate, so the simulation results were assumed to be mesh independent.

3.3 Results and discussion

3.3.1 Comparison of the modeling and experimental data for irradiance on the water surface

Figure 22 shows the measured irradiance on a water surface for the 265nm and 275nm LEDs when they were operated at the low forward currents. The 5 cm × 5 cm square surface was discretized into 121 cells, and the measured irradiance at the center of each cell is presented in Figure 22. The distance of each cell center from the center of the square surface was calculated, and the average irradiances across the radius were obtained. The irradiance measurements showed that the LED's radiation profiles were not fully symmetric and depended on the azimuthal angle (Figure 22). However, chi-square tests that examined the goodness of fit showed that the simulation results and the corresponding average irradiances were not statistically different. Therefore, the symmetric assumption was valid for fluence rate modeling.

The irradiance distributions of the 265nm and 275nm UV-LEDs were different, although both LEDs had heart-shaped radiation profiles and were placed at an approximate vertical distance. The marked differences imply the significance of the LED's radiation profile and the LED's

position for UV fluence determination so that utilizing an approximate radiation profile would result in erroneous predictions. The comparison between the normalized irradiance distributions for high and low forward currents showed that the LED's radiation profile was independent of the applied current. The normalized distributions confirmed that the actual LED's radiation profile is Γ times greater than the LED's normalized radiation profile.

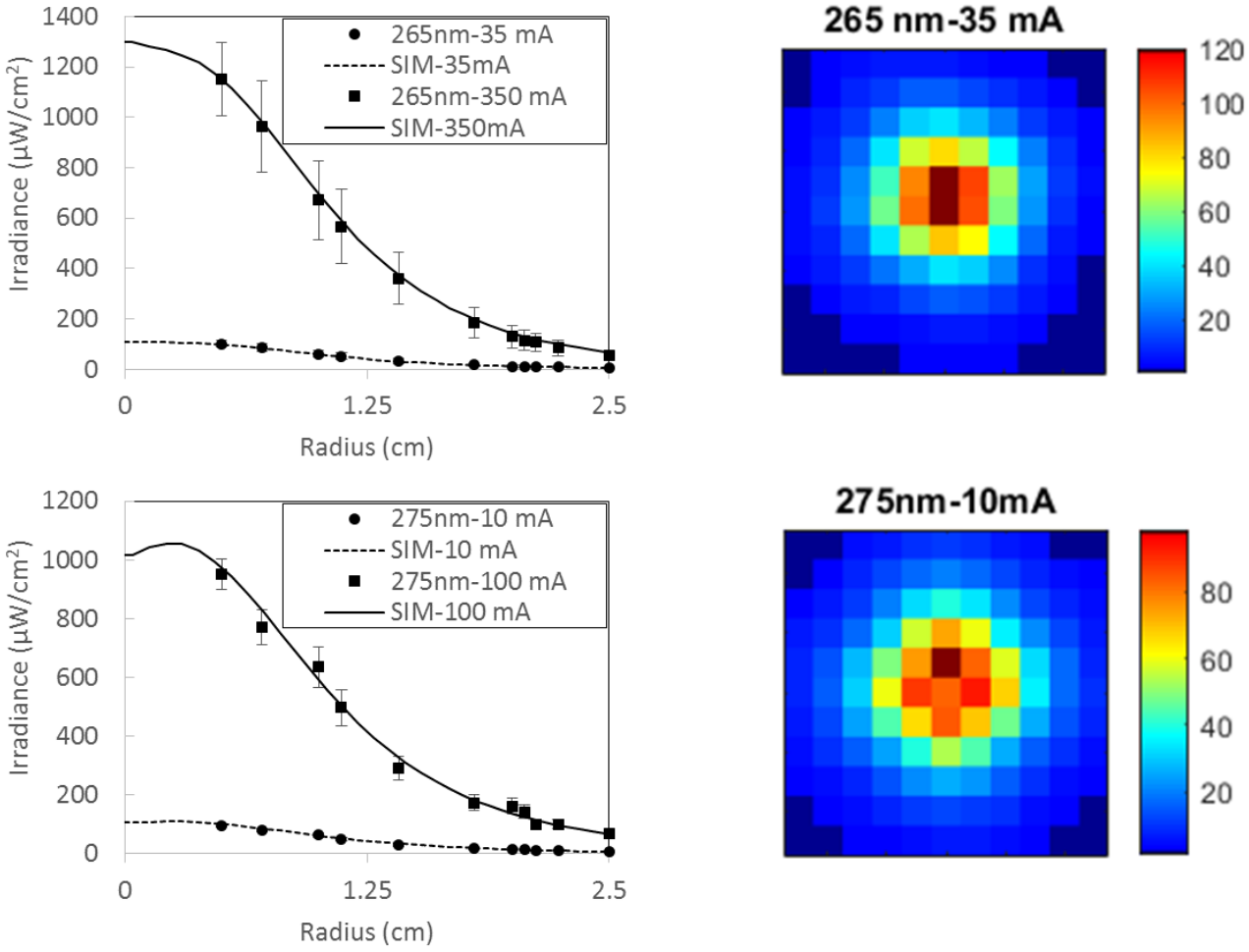

Figure 22. Left: Simulated and average measured irradiance across the radius of the 5-cm petri dish when 265-nm and 275-nm LEDs were operated at high (350 mA and 100 mA) and low forward currents (35 mA and 10 mA). The points are averages of at least four measurements, and the error bars represent standard deviations. Right: Irradiance distribution on the water surface where low forward currents applied to the LEDs.

3.3.2 Comparison of modeling and experimental data for fluence rate on the water surface

Chemical actinometry results expressed the average fluence rate at the water surface when the low and high forward currents were applied to the LEDs (Table 4). Utilizing the weighted quantum yield and weighted energy per einstein improved the numerical predictions. When the 265nm LED was operated at 350 mA, the fluence rate was 11 times greater than that of 35 mA. This was attributed to the non-linear relationship between the forward current and LED's output power. According to the current-power curve provided by the manufacturer, the radiant power at 350 mA was 11 times greater than that of a 35 mA. The same magnification number was used in the simulation, and the fluence rate measurements agreed well with the LED's datasheet. Likewise, for the 275nm UV-LED, the current-power relationship was confirmed by actinometry tests.

The simulations showed that the reflection increased from 2.44% at the center to 9.28% close to the border over the water surface when the 265nm UV-LED was operating (Figure 23-A). The delivered fluence rate to the center was almost 10 times greater than the one at the maximum radius (near the wall of the petri dish) which caused considerable non-uniformity on the water surface. The normalized fluence rate for high and low currents remained the same because it only depends on the LED's normalized radiation profile and position.

Table 4. Fluence rate at the water surface measured by Iodide/Iodate actinometry solution. The mean experimental results are presented with their standard deviations (SD).

		$\bar{E}_{0_{surface}}$(mW/cm^2)	
LED	current (mA)	Experiment (Mean±SD)	Simulation
265 nm	35	0.04 ± 0.00	0.04
	350	0.44 ± 0.02	0.45
275 nm	10	0.04 ± 0.00	0.04
	100	0.40 ± 0.02	0.41

3.3.3 Comparison of modeling and experimental data for the delivered fluence rate to the microbial suspension

The radiation model considers all the main parameters affecting the radiation distribution, resulting in accurate predictions on the surface of the water. Therefore, the evaluated radiation model can be used to predict the fluence rate within the well-mixed microbial suspension, and the predicted fluence rate can be used to test the following hypothesis. The delivered fluence rate to a well-mixed microbial suspension can also be estimated using biodosimetry tests if the UV-LED microbial inactivation data are available. In this section, using the UV-LED's germicidal efficiency and 254 nm fluence-response data, the UV-LED microbial inactivation data are estimated and used to predict experimentally delivered fluence rate. The comparison between the numerically and experimentally predicted fluence rate allows to test if the estimated kinetic data utilizing the germicidal efficiency lead to acceptable results.

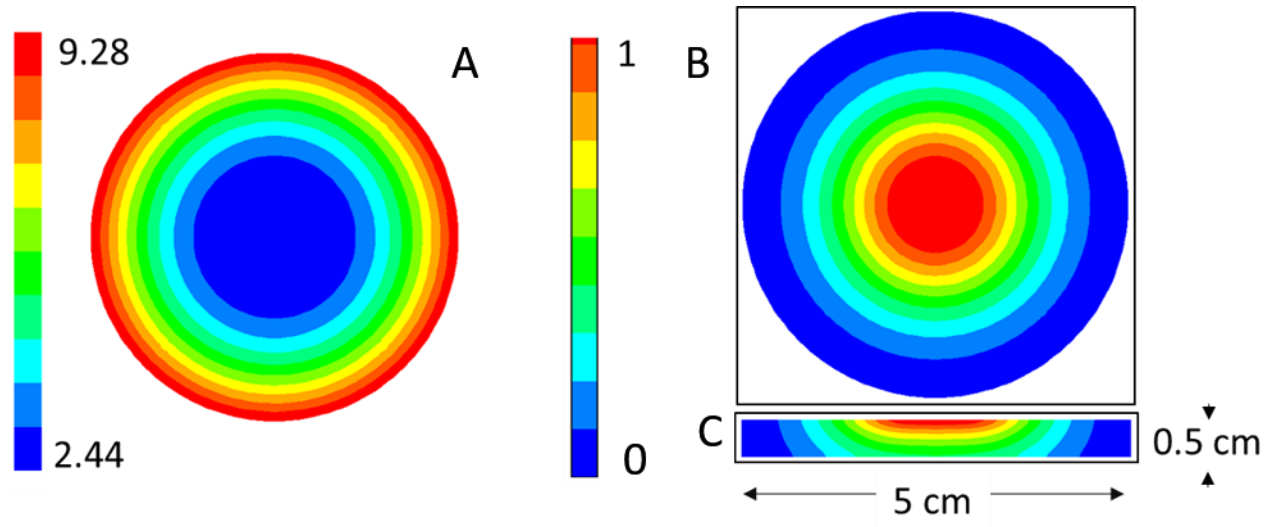

Figure 23. Numerically predicted distributions for reflection over the surface (A) and normalized fluence rate distributions over (B) and inside (C) the water when 265nm UV-LED was irradiating the solution in the 5-cm petri dish with 0.5 cm water depth.

Figure 23-C shows the simulated normalized fluence rate distribution inside the 5-cm Petri dish with a 0.5-cm water depth of 265nm UV-LED. The fluence rate at the central part was almost ten times greater than that of the corners (Figure 23-C). This means that microbial inactivation at the center takes place almost ten times faster than corners. The results of the biodosimetry test could be used against the simulation if the microbial suspension was fully mixed and all microorganisms were exposed to the same level of UV fluence. To smooth out the non-uniform fluence rate distribution, the water could be mixed gently for a long time or vigorously for a short time. If the suspension was mixed vigorously, the water surface would not remain flat during the exposure, so the flat assumption would not be valid. Therefore, the suspension was mixed gently to be consistent with the flat surface assumption.

In biodosimetry tests using *E. coli*, the experimental fluence rate ($E_{0\,EXP}$) approached simulated fluence rates, $E_{0\,SIM}$ (Table 5) at long exposure times. The disagreement between

$E_{0\,EXP}$ and $E_{0\,SIM}$ at shorter exposure times (<200s) can be attributed to the non-uniform UV fluence distribution to the microorganisms due to insufficient mixing. It appears that gentle mixing for a relatively short time period was not sufficient to uniformly spread the organisms across the solution in order to be exposed to the same UV fluence. Table 5 shows that for both UV-LEDs at exposure times longer than 200 seconds, the simulated fluence rates lied between the lowest and highest limits, which were obtained based on the upper and lower bounds of fluence-response data (Figure 20). These limits specify the minimum and maximum possible fluence rates that would result in the same *E. coli* inactivation based on the probability distribution of *E. coli* inactivation. The difference between the simulated and the experimental mean fluence rate for 265nm and 275nm UV-LEDs was 3% and 5%, respectively. It can thus be concluded that the simulated and experimental mean fluence rates were not statistically different ($P<0.01$). Utilizing a more accurate *E. coli* action spectrum would further improve the determination of experimental fluence rates.

In a different set of experiments, the delivered fluence rate to the water was evaluated using biodosimetry test with MS2. The MS2 was irradiated for 480 s by the 275 nm UV-LED at 100 mA in the 9-cm Petri dish. The water depth and the height of UV-LED from the water were 1 cm and 2.4 cm, respectively. The exposure time was long enough to lead to uniform fluence distribution. Since MS2 is more resistant than *E. coli*, the UV-LED was operated at its highest forward current to deliver maximum radiant power to the solution. The simulated fluence rate lied between the lower and higher limits, and it was 4% higher than the mean value. The close agreement between the simulated and experimental fluence rate showed that the kinetics data can be estimated using the germicidal factor derived based on the action spectra of microorganism and the entire emission spectrum of the UV-LED.

Table 5. Simulated and experimentally calculated fluence rates in different operating conditions. Log inactivations are the average of three experiments with their standard deviations.

					$E_{0\,exp}$ (mW/cm^2)			$E_{0\,SIM}$ (mW/cm^2)
	petri dish	LED	Time (s)	Log(N_0/N)	Mean	Lower limit	higher limit	
E. coli	5 cm	265 nm (35 mA)	75	1.22 ± 0.08	0.044 ± 0.001	0.049	0.038	0.031
			100	1.66 ± 0.21	0.037 ± 0.002	0.042	0.033	
			125	2.67 ± 0.17	0.038 ± 0.001	0.042	0.035	
			200	4.30 ± 0.21	0.032 ± 0.001	0.035	0.030	
			225	4.60 ± 0.33	0.030 ± 0.002	0.032	0.028	
		275 nm (10 mA)	125	1.73 ± 0.2	0.041 ± 0.002	0.036	0.046	0.034
			200	3.46 ± 0.36	0.037 ± 0.003	0.033	0.039	
			225	4.08 ± 0.18	0.036 ± 0.001	0.033	0.038	
MS2	9 cm	275 nm (100 mA)	480	1.94 ± 0.19	0.102 ± 0.010	0.097	0.107	0.106

3.3.1 The Effect of reflection on the fluence rate

Figure 24-A and Figure 24-B show the distribution of the direct and reflected fluence rate inside the 5 cm petri dish when 265 nm UV-LED was placed 1.7 cm above the water surface. As seen, both bottom and peripheral walls reflect UV rays. The incident angles of the rays that hit the peripheral wall are significantly larger than that hit the bottom wall (Figure 24-C). Due to that, the reflectance (Fresnel's law) from the peripheral wall is greater than that of the bottom wall. However, since the radiant energy of impinged beams at the center is higher than that of that hit the peripheral wall (Figure 24-C), the highest amount of the radiant energy is seen around the center. As seen, the fluence rates in Figure 24-B are significantly lower than Figure 24-A. In fact, the reflected energy contributes to the less than 1% of the overall fluence rate. The effect of reflection is not tangible because the refractive indices of water (1.37) and glass (1.5) are close to

each other, thereby the most of incident energy is transmitted at the water-glass interface. As can be inferred, the impact of the internal reflection decreases even more and becomes negligible when the beams become collimated at farther distances. Therefore, the effect of reflection can be ignored during the fluence rate determination.

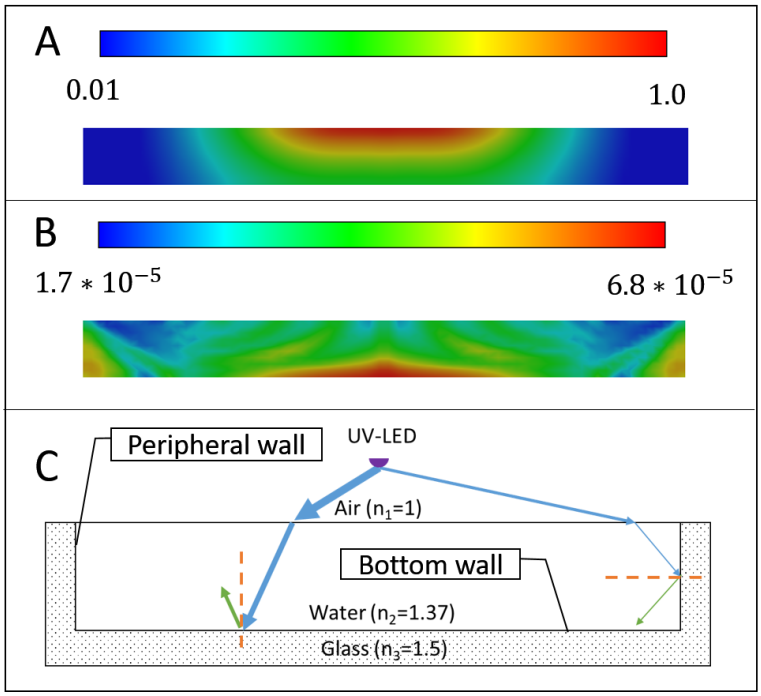

Figure 24. Fluence rate distribution [mW cm^{-2}] resulted solely from direct (A) and reflected (B) UV rays. UV rays hit the bottom wall with the smaller incident angle, so the ratio of energy that is reflected from bottom wall is relatively smaller than the peripheral wall, where the incident angle of UV rays is the highest.

3.4 Summary

The developed radiation model was applied to determine the delivered fluence rate to a well-mixed microbial suspension inside a petri dish. The accuracy of predictions was successfully evaluated using actinometry and radiometry techniques. The delivered fluence rate to microbial suspensions was calculated by considering UV-LEDs germicidal efficiencies and their 254 nm UV fluence-response data. The close agreement between numerical predictions and experimental data

showed that utilizing microorganisms action spectra and UV-LED emission spectrum for the calculation of germicidal efficiency could lead to acceptable kinetic data. Therefore, if the action spectrum of a microorganism is available, the kinetic data can be estimated using the method proposed in this study, which eliminates the need for experimental study.

This finding benefits UV-LED reactor simulation, particularly when the reactor contains UV-LEDs with various wavelengths, which have different inactivation rate constants. Utilizing the germicidal efficiency concept allows to determine the efficiency of each UV-LED with respect to 254 nm wavelength, and then apply 254 nm fluence-response data to simulate the reactor. Nonetheless, when the action spectra of microorganisms are not available, the proposed numerical method can be applied to predict the delivered fluence rate reliably.

Chapter 4: Computational modeling of UV-LED reactor for water treatment

4.1 Introduction

The Lagrangian and Eulerian modeling have been applied to the simulation of conventional UV reactors [33,34,74–76]; however, simulating UV reactors in the Eulerian framework provides necessary information for the design modification. The main drawback of the Lagrangian approach is its sensitivity to the number of released particles and not providing critical information for the design modification for the entire numerical domain. On the contrary, in the Eulerian framework, the microorganisms' concentration throughout the domain is obtained by solving the governing equation of mass and momentum conservation. So far, the performance of a flow-through UV-LED reactor in the Lagrangian framework using a simplified radiation model has been studied [45, 68]. Despite several studies related to the application of UV-LEDs for water and air purification [19, 37, 56, 83, 84], UV-LED reactors have not yet been simulated in the Eulerian framework.

In this chapter, a computational method for the simulation of UV-LED reactors for water treatment is proposed. In order to incorporate the effects of different UV-LEDs, a practical approach which works based on a single volumetric reaction rate is presented. In this study, a cylindrical flow-through UV-LED reactor comprised four UV-LEDs was selected for case studies. To assess the accuracy of the numerical predictions in different flow regimes, the UV-LED reactor was equipped with a diffuser in some of the experiments. The reactors with and without the diffuser were simulated in different operating conditions. The capability of the model for predicting the reactor performance was evaluated using biodosimetry with *E. coli* (ATCC 11229) and MS2 (ATCC 15597-B1) as challenge microorganisms. The biodosimetry experiments were carried out in different flow rates, flow regimes, UV-LED arrangements, and UV intensities. This chapter

explains explicitly how to identify the poorly-performed regions and methods for the reactor design modification.

4.1.1 Fundamentals of UV reactor modeling in the Eulerian framework

To simulate a UV reactor, the numerical domain is initially discretized into tiny computational cells. This step is followed by solving the governing equations of mass and momentum conservation for all the computational cells to obtain the velocity and pressure distributions. Next, the fluence rate at the centroid of each cell is calculated and stored in the memory of the computer. In Eulerian modeling, the microbial species are treated as chemical substances with the same properties as that of the water [33–35]. Based on this assumption, there are three components in the UV reactor, and they are the water (medium), alive organisms, and inactivated organisms. The properties of alive and inactivated organisms are the same, and this assumption aligns with the concept of UV disinfection (i.e., inactivated germs are alive but cannot replicate [1]). If there is a mixture of different types of microorganisms, each species is treated as a chemical substance with a specific kinetic rate constant, and the inactivation of one species does not impact others. In the Eulerian framework, each computational cell is treated as a small completely-mixed reactor so that there is not a gradient of fluence rate, the concentration of organisms, and the rate of reaction across the computational cell. In this view, the tiny computational cell behaves the same as a UV reactor that its microbial inactivation rate depends on the received fluence (which is the product of the local fluence rate and residence time of organisms in the computational cell). From this perspective, the local performance of a UV reactor can be defined based on the delivered fluence to each computational cell. If the collimated beam fluence-response data is applied to the received fluence, the amount of microbial removal per volume of the cell is found. This quantity is defined as the volumetric reaction rate. Through

solving the species mass conservation equations by considering the mass flows of species to/from and volumetric reaction rates are happening in the computational cells, the concentration of microorganisms is obtained across the numerical domain.

The concentration at each cell centroid illustrates the combined effect of hydrodynamics, radiation, and kinetics across the reactor. The concentration data implicitly contains the movement of particles (species) throughout the reactor; therefore, it illustrates the effect of accumulated fluence to the microorganisms. Given that, through back calculating the concentration information using the fluence-response data, the accumulated fluence across the reactor is obtained. The accumulated fluence shows how microorganisms receive energy from the inlet all the way to the outlet. In fact, it reveals the accumulated effects of locally delivered fluences of computational cells and the overall performance of the UV reactor.

In the Eulerian modeling, the kinetics information is concurrently integrated with radiation and hydrodynamics data, and this combination appears as volumetric reaction rate in the calculations. Therefore, the determination of the volumetric reaction rate is crucial. As we discussed in Chapter 3, UV-LEDs inactivation kinetic depends on their emission spectra, and if UV-LEDs with different peak wavelengths are used in the reactor, more kinetic data are needed.

4.2 Materials and methods

4.2.1 Numerical procedures

Fluid flow, the distribution of UV energy, and the kinetics of inactivation impact the performance of a UV reactor. Appropriate models are needed to capture such phenomena and integrate them to be able to simulate a UV reactor. In this section, relevant models along with the procedure for their integration are expressed.

4.2.1.1 Fluid flow model

The velocity and pressure distributions were obtained by solving the governing equations of the mass (Equation 11) and momentum (Equation 12) conservation, where $v, \rho, p, \tau, g, and\ f$ are velocity, density of the water, pressure, viscous stress tensor, gravitational acceleration, and external body force, respectively.

$$\nabla \cdot v = 0 \quad (11)$$

$$\nabla(\rho v v) = -\nabla p + \nabla \cdot \tau + \rho g + f \quad (12)$$

The density of organisms was assumed the same as that of water [34], and the molecular diffusion of microorganisms into the water was deemed negligible [34,35]. Therefore, in the steady state laminar flow regime, the species mass conservation equation can be simplified (Equation 13), where x_i, S_i are species mass fraction and source term, respectively. The source term represents the volumetric reaction rate of microorganisms. As for the turbulent regime, Equation 14 represents the species mass conservation when species turbulent Schmitt number (ϑ_t) was 0.7 [34].

$$\nabla(\rho x_i v) = S_i \quad (13)$$

$$\nabla(\rho x_i v) + \frac{\vartheta_t}{0.7}\nabla^2(\rho x_i) = S_i \quad (14)$$

4.2.1.2 Kinetic model

Microbial inactivation is a function of UV fluence (F) and the inactivation rate constant (k') (Equation 15). Chick-Watson, rational, and series event are examples of the microbial inactivation models that correlate the delivered fluence to the microbial inactivation [35]. In Equation 15, which represents Chick-Watson microbial UV inactivation model, F, N_0, and N are UV fluence, the number of microorganisms before and after the UV exposure, respectively. Note, Fluence is a product of fluence rate (E_0) and exposure time (t).

$$\log(\frac{N}{N_0}) = -k'F \qquad (15)$$

By rearranging and substituting concentration ratio ($\frac{C}{C_0}$) for the microbial survival ratio ($\frac{N}{N_0}$) and the product of E_0 and t for F in Equation 15, the following equation is obtained:

$$\frac{C}{C_0} = 10^{(-k'E_0 t)} \qquad (16)$$

where C_0 ($\frac{kg}{m^3}$) and C ($\frac{kg}{m^3}$) are the concentration of microorganisms before and after UV exposure, respectively. Equation 16 correlates the concentration of microorganisms to the exposure time under constant fluence rate in a completely-mixed reactor. The derivative of Equation 16 with respect to time yields the volumetric rate of microbial inactivation ($\frac{kg}{m^3.s}$) (Equation 17). As seen, volumetric reaction rate (Equation 17) with respect to the microbial concentration (C) is a first order kinetic, and its magnitude depends on the local concentration (C), fluence rate (E_0), and the inactivation rate constant (i.e., k').

$$\frac{dC}{dt} = -(\ln(10) * E_0 * k') * C \qquad (17)$$

4.2.1.3 Radiation model

In water treatment applications, the UV source is typically separated from water by a quartz window. In this study, the UV-LEDs were separated from the water by a commercial grade quartz window (Technical Glass product, Inc.). Based on the size of UV-LEDs, it was assumed that they were 500 μm away from the quartz window. In our model, refraction, reflection, and attenuation of UV rays while they pass through two interfaces air-quartz and quartz-water were taken into account. The refractive indices of air, quartz, and water were 1, 1.48, and 1.37 respectively. With

regards to UV absorption of the quartz it should be mentioned that since UV-LEDs were slightly different and the quartz's UVT was not constant (Figure 10), the weighted quartz's UVT for each UV-LED was calculated. The details of the radiation model were described in Chapter 2.

4.2.1.4 Strategies to adjust the volumetric reaction rate

Equation 17 is a general formula that can be applied to the simulation of any UV reactor. However, two parameters E_0 and k' need to be adjusted because UV-LEDs could have different emission spectra which in turn impacts k', and k' is not necessarily constant at any given fluence.

The k' represents the slope of the fluence-response curve at any given fluence. Since microorganisms (particularly bacteria) have repair mechanisms, they tend to show shoulder effect at low fluences. Due to that, *E. coli*'s fluence-response data do not follow a linear pattern similar to MS2 (Figure 20). Instead, it tends to illustrate a S-shape pattern which starts with a shoulder phase at the low fluences, a semi-log phase in the middle and tailing (saturation phase) at high fluences. To address the non-linearity of *E. coli* kinetic data, its fluence-response curve was captured by means of two linear functions to differentiate the different rates of reaction during the shoulder and semi-log phases.

According to Equation 17, another parameter that influences the magnitude of the volumetric reaction rate is the local fluence rate (E_0). When multiple UV-LEDs with different peak wavelengths are used to irradiate water, the rate of inactivation is influenced by the combined effects of each individual UV-LED. Since the disinfection capacity of a UV-LED depends on its emission spectrum, multiple kinetic data and source terms are required to simulate the reactor, which make the simulation complicated. To address this problem, the germicidal powers of UV-LEDs were used to calculate fluence rate. The germicidal power of a UV source expresses the ratio of the effectiveness of the UV source compared to that of a low-pressure UV lamp. In short, the

germicidal power of a UV source is the convolution of its spectral power distribution and the action spectra of a microorganism. Given that, using the UV-LED's germicidal factor, one is able to convert the radiant power of a UV-LED to that of a low-pressure UV lamp (254 nm). Therefore, the reliable fluence-response data obtained by a collimated beam apparatus using a LP UV lamp can be used as an acceptable approximation for obtaining reliable kinetic data. In this study, the challenge organisms' 254 nm kinetic data, which were obtained by following Bolton's method [53] from the year of 2000 onward, were collected from the literature [69], and the average of the collected data was selected for simulation. The details were explained in Chapter 3.

4.2.1.5 Geometrical model, mesh structure, and boundary condition

In this study, two UV-LED reactors were simulated, and the geometries of each of them are shown in Figure 25. ANSYS 18.2 simulation package was used to build and discretize the problem domains of the reactor with and without a diffuser, hereafter reactor-1 and reactor-2 (Figure 25), via 742539 hexahedral and 1047222 tetrahedral cells, respectively. Mesh size provided grid-independent results as further mesh refinement had a negligible impact on velocity, fluence rate, and concentration distributions. Fully developed boundary condition was applied to the inlet, and pressure-outlet and no-slip boundary conditions were imposed on the outlet and internal walls, respectively. The mass fraction of microorganisms at the inlet was set to one. Additionally, zero diffusive flux of species was specified on the walls.

4.2.1.6 Numerical solution method and strategy

ANSYS Fluent was employed to read the mesh and to perform the simulation. Two user-defined functions were developed and integrated into ANSYS Fluent to compute the source terms in the species mass conservation equations and fluence rate distribution. The steps were taken to implement the fluence rate distribution were explained in Chapter 2. The species transport model

was utilized to implement the species mass conservation equations. A user-defined function was developed to compute the volumetric reaction rate (source term) within each computational cell throughout the simulation process. The Laminar and realizable $k-\epsilon$ models from the hydrodynamic sub-models were selected for reactor-1 and reactor-2, respectively. The enhanced wall treatment method was used as a wall function. The SIMPLEC was selected for the pressure-velocity coupling. The second-order upwind was chosen for pressure and momentum and QUICK for species under spatial discretization. Finally, 0.7 was used for species under-relaxation factor. The convergence of the results was approved once the errors of two successive iterations for the scaled residuals were less than10^{-6}. Since the movement of microorganisms do not change the velocity distribution, the velocity field was initially obtained and kept frozen and then the species mass conservation equations were solved [75].

4.2.2 Experimental procedures

The UV-LED reactor consisted of a 5 cm plexiglass pipe with a length of 17 cm to incorporate four UV-LEDs (Figure 25). To assess the performance of the reactor in a wider range of hydrodynamics, a 2 cm circular object, henceforth it is called diffuser, was fixed on the axis of the reactor by a narrow rod (Figure 25). The UV-LEDs were running in series mode, and they were separated from the water using a 3 mm thickness commercially grade quartz sheet (Technical Glass product, Inc.). To effectively control the temperature of each UV-LED during the operation, the heat dissipation was managed by means of a combination of a thermoelectric cooler, a heatsink, and a fan. The inlet and outlet pipes (ID= 1 cm) were aligned with the axis of the reactor. In addition, the length of the inlet pipe was chosen 20 cm to eliminate the effect of entrance length and let the fully developed flow enter the reactor.

To maintain the homogeneity of the microbial suspension (i.e., *E. coli* or MS2) throughout the experiment, the suspension inside the feeding tank was stirred continuously using a mixer. The initial concentration of the microbial suspension in the feeding tank was typically 10^6 CFU/ml or PFU/ml. The UVT of the suspension was measured at 270 nm using a spectrometer (Cary 100 UV-VIS). The flow was pumped to the reactor by a peristaltic pump (Masterflex Analog pump system, Cole-Parmer Instrument Company), and a pulse dampener (Masterflex Pulse dampener, Cole-Parmer Instrument Company) was installed after the pump to dampen the flow fluctuation. The samples were collected at the outlet and kept in the dark and cultivated shortly after the sample collection.

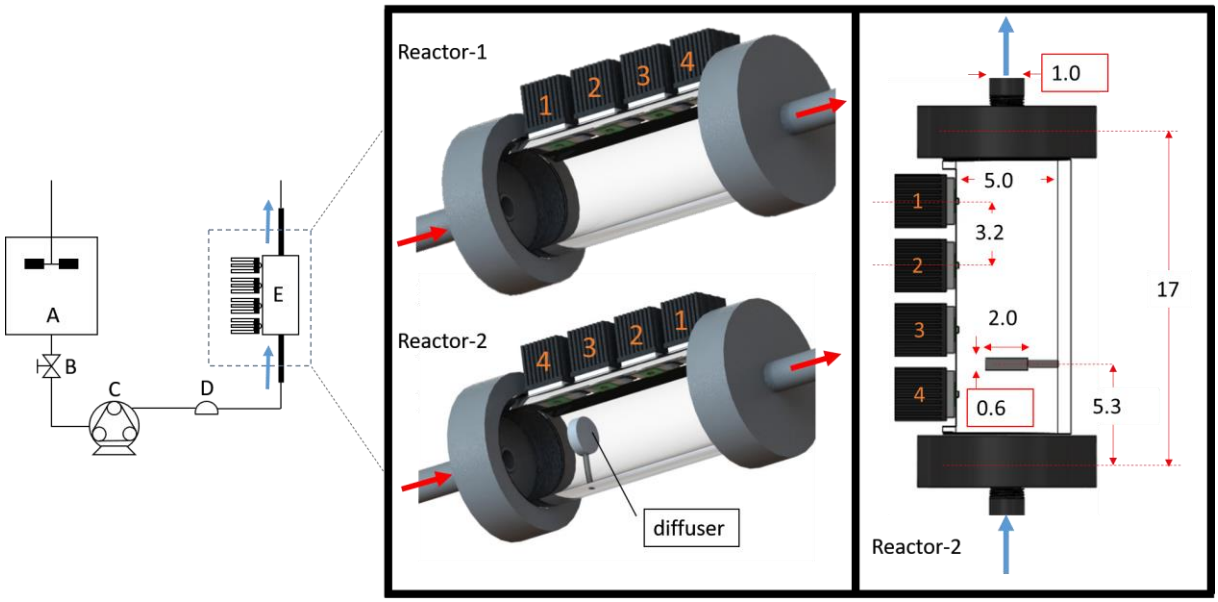

Figure 25. Left: schematic of the flow-through UV-LED reactor setup including a feeding tank with a mixer (A), valve (B), peristaltic pump (C), pulse dampener (D), and the UV-LED reactor (E). middle: reactor-1 and reactor-2. Right: the dimensions (cm) of the UV-LED reactor along with the diffuser.

4.3 Results and discussion

The simulation predictions were evaluated experimentally using two UV-LED reactors with *E. coli* and MS2 under different operating conditions such as different flow rates, flow

regimes, radiation intensities, and radiation distributions. In the following, the numerical and experimental results are presented, and a detailed discussion is provided about the UV-LED reactor performance and design modification.

4.3.1 The effect of flow rate on Reactor-1

The disinfection capacity of a UV reactor can be reported as a reduction equivalent fluence (REF). The reduction equivalent fluence is determined by inputting the measured log inactivation into the UV dose-response curve [6]. In other word, REF represents the amount of UV fluence which on average is delivered to the water. Since the delivered UV fluence determines the efficiency of a UV reactor, it was selected to compare the performance of the reactor in different conditions instead of log-inactivation, which depends on the type of microorganism.

Figure 26 shows that 3 $\log_{10}$-inactivation of *E. coli* (i.e., REF=6.2 $\frac{mJ}{cm^2}$) happened at the flow rate of 90 ml/min when all the UV-LEDs were operating at 375±5 mA. The $\log_{10}$-inactivation dropped sharply to 1.44 $\log_{10}$ (REF=4.2 $\frac{mJ}{cm^2}$) when the flow rate changed to 120 ml/min. When the flow rate further increased and reached 150 ml/min, the *E. coli* inactivation dropped to 0.97 $\log_{10}$ (REF=3.6 $\frac{mJ}{cm^2}$). By increasing the flow rate by 33% and 67% with respect to 90 ml/min, the equivalent dose delivered by the reactor reduced by 32% and 42%.

Simulations results agreed well with the measurements in all the flow rates (Figure 26), and the model captured this non-linearity of inverse inactivation versus flow rate. It was seen that utilizing the inactivation function for the reactor simulation led to slightly overprediction. The difference between the simulations and the average of measurements for the flow rates of

90 ml/min, 120 ml/min, and 150 ml/min were 2.5%, 10.5%, and 9.0%, respectively. Nonetheless, all the simulations lied within the standard deviation of the experimental measurements.

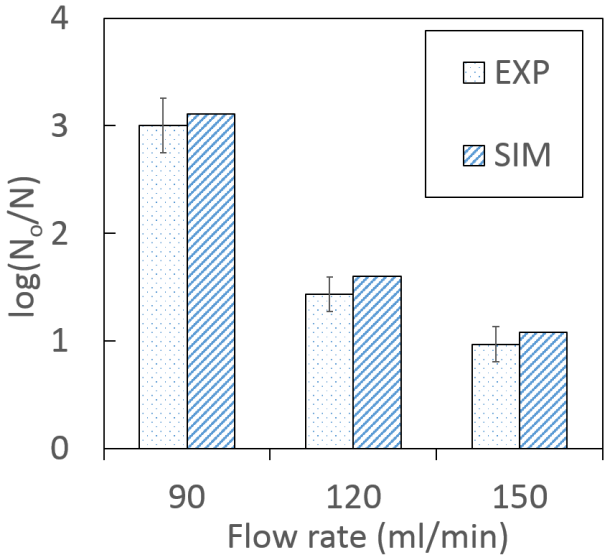

Figure 26. The simulation and experimental data for *E. coli* inactivation in reactor-1 when UV-LEDs were operating at 375 mA. The error bars show standard deviations for three independent tests.

The inactivation results can further be understood by studying the distribution of flow, radiation, and the delivered dose in the reactor. Figure 27-A shows the velocity contours on the longitudinal cross section of the reactor-1 at the 150 ml/min flow rate. The Reynolds numbers inside the pipe and the reactor were 317 and 63, respectively; therefore, the flow field was obtained using laminar model. It is seen that the water moves fast along the axis of the reactor-1, and the water recirculates in the region between the central axis and the walls due to the pressure difference. Due to the recirculation, the relatively higher residence time for the water is expected in that region. Figure 27-B shows that the fluence rate distribution is not uniform and decreases at farther distances from UV-LED. Since the refractive indices of the water (i.e., 1.37) and the plexiglass (i.e., 1.5) are close to each other which lead to a large amount of incident energy leaves the reactor, the reflection from the walls does not significantly alter the fluence rate distribution.

Figure 27-C displays a highly concentrated stream of *E. coli* passes through the central section while the rest of the reactor treats water to a high degree. Farther distances from UV-LEDs' principal direction near the wall, where a relatively low fluence rate is available, the water has a lower microorganism concentration than the central section. The locally delivered fluence can explain the observation. In our model, each computational cell is analogous to an ideal CSTR which its efficacy is determined by the residence time and delivered fluence rate. In other words, local performance can be related to the delivered fluence in each computational cell. In this view, this reactor can be divided into three sections near UV-LED, middle section, and far from UV-LEDs (Figure 27-D). Figure 27-D shows that near UV-LED where the water has low velocity and receives high fluence rate, the rate of inactivation is high (i.e., high fluence). In the middle section due to low residence time and fluence rate, the reactor performs poorly. Finally, in the area far from UV-LEDs, although lower fluence rate than middle section is received, the high fluence is delivered to microorganisms due to high residence time.

The local fluence determines the performance of each cell; however, it should be noted that the overall performance of a UV reactor depends on the accumulated fluence. Microorganisms receive different amounts of UV energy depending on their trajectories within the reactor, and the sum of all the locally delivered fluences yields the accumulated fluence received by each microorganism. The accumulated fluence distribution shows how microorganisms receive UV energy along their trajectories, so the effect of any change on the local performance will appear on the accumulated fluence.

In the Eulerian framework, the concentration of microorganisms represents the history of the interaction of hydrodynamics, radiation, and kinetic across the reactor. Therefore, using the microorganism's fluence-response curve (e.g., Figure 20), the accumulated delivered fluence

across the reactor can be obtained. Figure 27-E displays the accumulated fluence across the reactor. The accumulated fluence decreases slightly at the top and adjacent to the walls because the water recirculates and brings back a part of untreated microorganisms. The amount of the accumulated fluence in the middle section is far less than other sections, showing the area that reduces the reactor performance. This information helps to identify the areas of low performance in the reactor. Such areas then can be minimized by implementing changes in the reactor design. For example, if the low fluence in one area results from short residence time (i.e., high velocity) the flow pattern in the reactor can be modified by applying flow modifier. Similarly, if the low fluence results from low fluence rate, the UV-LEDs can be rearranged to generate a better distribution.

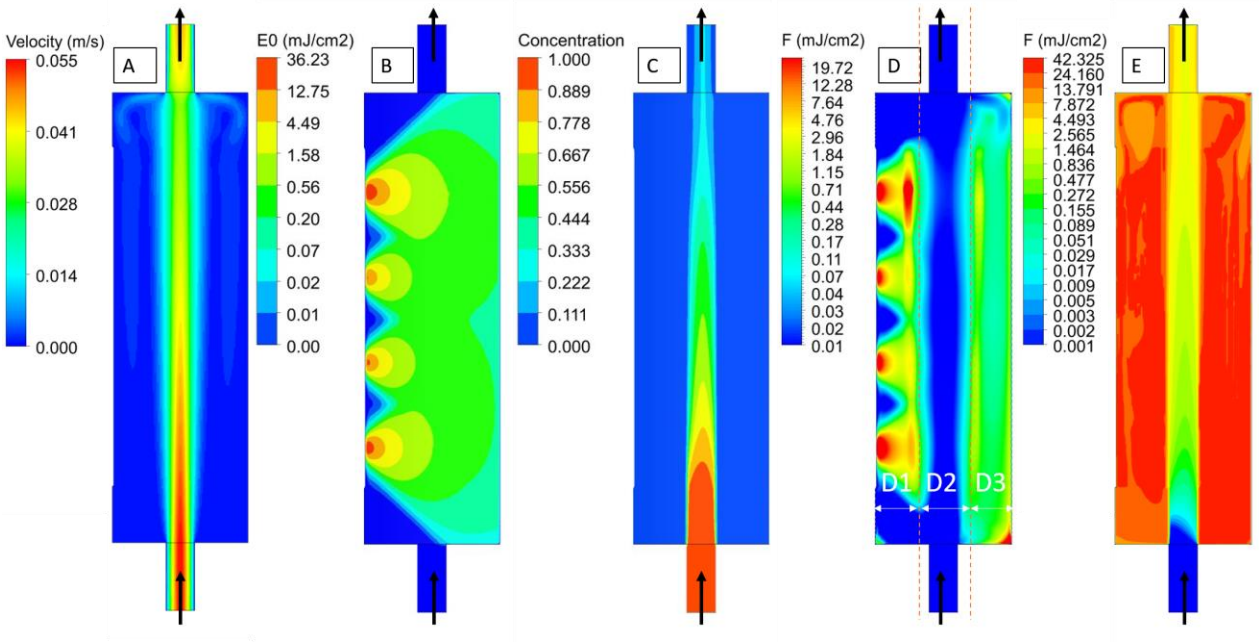

Figure 27. Velocity (A), fluence rate (B), normalized concentration (C), local delivered fluence (D), and accumulated delivered fluence (E) distributions on the longitudinal cross section of the UV-LED reactor at the flow rate of 150 ml/min and forward current of 375 mA. The reactor can be divided into three sections which are near UV-LED (D1), the middle section (D2), and far from UV-LEDs (D3).

4.3.2 The effect of radiant power and configuration

Unlike UV lamps, the power of UV-LEDs can be adjusted. Such capability of UV-LEDs allows tailoring their outputs to the target microorganism, which results in the operational flexibility and energy saving. Another operation flexibility that a UV-LED system offers relates to UV-LED fast start-up capability. Since UV-LEDs have no warm-up time, they can be turned on/off instantly, thereby the number of operating UV-LEDs in the system can be managed based on the flow rate. In this section, the capability of the simulation method for capturing the behavior of the reactor under different UV-LEDs' outputs and configuration is presented.

To study the effect of radiant power on the performance, the forward current of UV-LEDs was halved at the flow rate of 90 ml/min, which resulted in a 48% reduction in the UV-LEDs outputs. Although the UV-LEDs' outputs became approximately halved, the overall $\log_{10}$-removal decreased by more than 50% (Figure 28). If a linear relationship is assumed between the power and inactivation rate, it is expected to see ~50% reduction in $\log_{10}$-inactivation; however, 67% reduction was observed. This further reduction in efficacy was related to the *E. coli* inactivation curve as it is not linear. The analysis of performance in terms of delivered fluence showed that when the output reduced by 48%, the REF decreased ~43%, which implies a linear relationship between REF and the outputs of UV-LEDs.

In a separate set of the experiments, the effect of UV-LED arrangement on the reactor performance was studied. This experiment aimed to investigate the contribution of LED1 and LED4 to the overall inactivation at the flow rate of 90 ml/min; and if the model is capable of predicting such contribution. The experiments showed that 1.7 $\log_{10}$ (REF=4.5 $\frac{mJ}{cm^2}$) could be achieved by the two LEDs (Figure 28), and this was closely predicted by the model which was

1.6 $\log_{10}$ (REF=4.4 $\frac{mJ}{cm^2}$). The close agreement between the simulation and experiments showed the potential of this technique for assessing each element of the reactor. The circuit of UV-LEDs can be designed in such a way to turn the UV-LEDs on and off independently to meet the target REF in different flow rates.

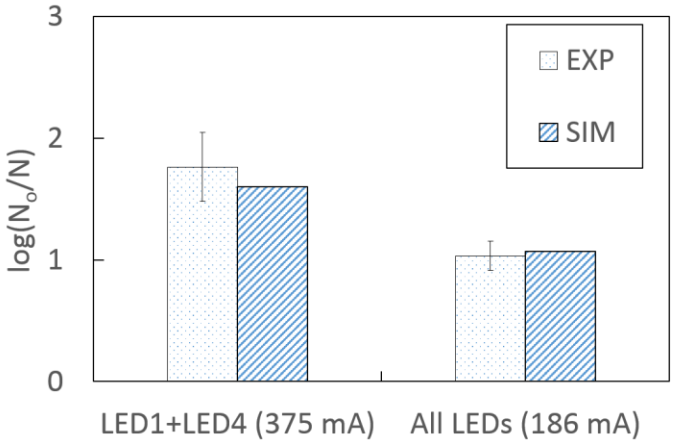

Figure 28. The simulation and experimental data of *E. coli* inactivation for reactor-1 when only LED1 and LED4 were operating at 375 mA (Left), and all LEDs were operating at 186 mA (Right) at the flow rate of 90 ml/min.

4.3.3 The effect of hydrodynamic alteration

The simulation results of reactor-1 revealed that the central area (Figure 27-D2) inside the reactor reduced the overall reactor performance. A diffuser was placed to divert the water from the central area to modify the flow and prevent the high-velocity flow jet at the reactor center. The realizable $k-\epsilon$ model with Enhanced Wall Treatment (wall function method) was chosen to simulate the flow field in reactor-2. According to the simulation predictions, reactor-2 could disinfect *E. coli* at the flow rate of 250 ml/min beyond the detection limit; therefore, MS2, as a more UV resistant organism, was chosen for the experimental studies. As a result of the flow modification, reactor-2 could achieve 1.35 and 0.79 $\log_{10}$ of MS2 inactivation (Figure 29) or 25

$\frac{mJ}{cm^2}$ and 11.5 $\frac{mJ}{cm^2}$ in terms of REF at 250 mL/min and 600 mL/min, respectively. Given reactor-2 outperformed reactor-1 under the same operating conditions, the overall improvement can be attributed to hydrodynamic effects. The velocity contours on the longitudinal cross section of the reactor-2 (Figure 30-A) shows that the flow is diverted from the central part after hitting the diffuser, and water moves towards the reactor's wall and then recombines somewhere near the outlet. As a result of the flow distribution, microorganisms pass near UV-LED and are exposed to the highest UV radiation inside the reactor (Figure 30-B).

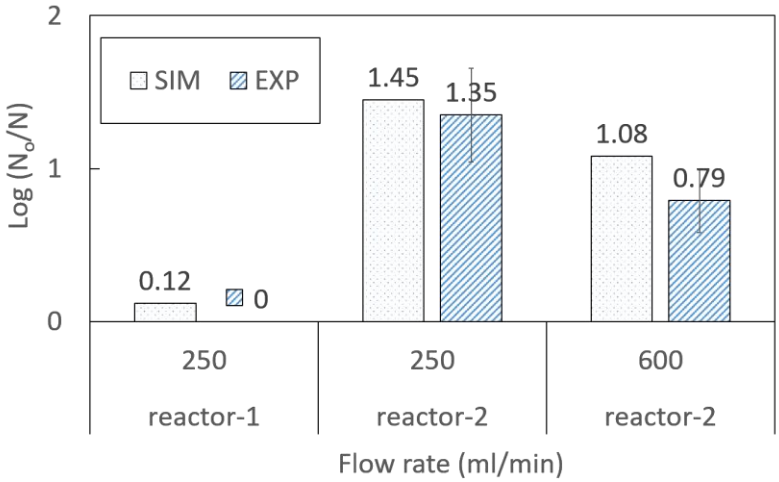

Figure 29. The simulation and experimental data for MS2 inactivation when UV-LEDs were operating at 375 mA. The error bars show standard deviations of six independent experiments. The experimental data are given as the mean of six independent tests at each flow rate.

Figure 30-C shows the normalized concentration distribution on the longitudinal cross section of reactor-2. There is a significant difference between the concentration of MS2 before and after the diffuser (Figure 30-C). Due to the water recirculation before the diffuser, the MS2 concentration decreases considerably, and unlike reactor-1, there is not a highly concentrated area around the axis of reactor-2. After the diffuser, however, the water gets disinfected gradually with higher inactivation in an area close to UV-LEDs. As seen, the concentration distribution is not

uniform despite the diffuser spreads microorganisms across the lateral cross section. Since fluence rate attenuates along the principal direction of UV-LEDs, microorganisms that pass under the diffuser and are far from UV-LED experience lower rates of inactivation compared to those pass near UV-LED (Figure 30-C). Therefore, concentration distributions over the lateral cross sections are not uniform.

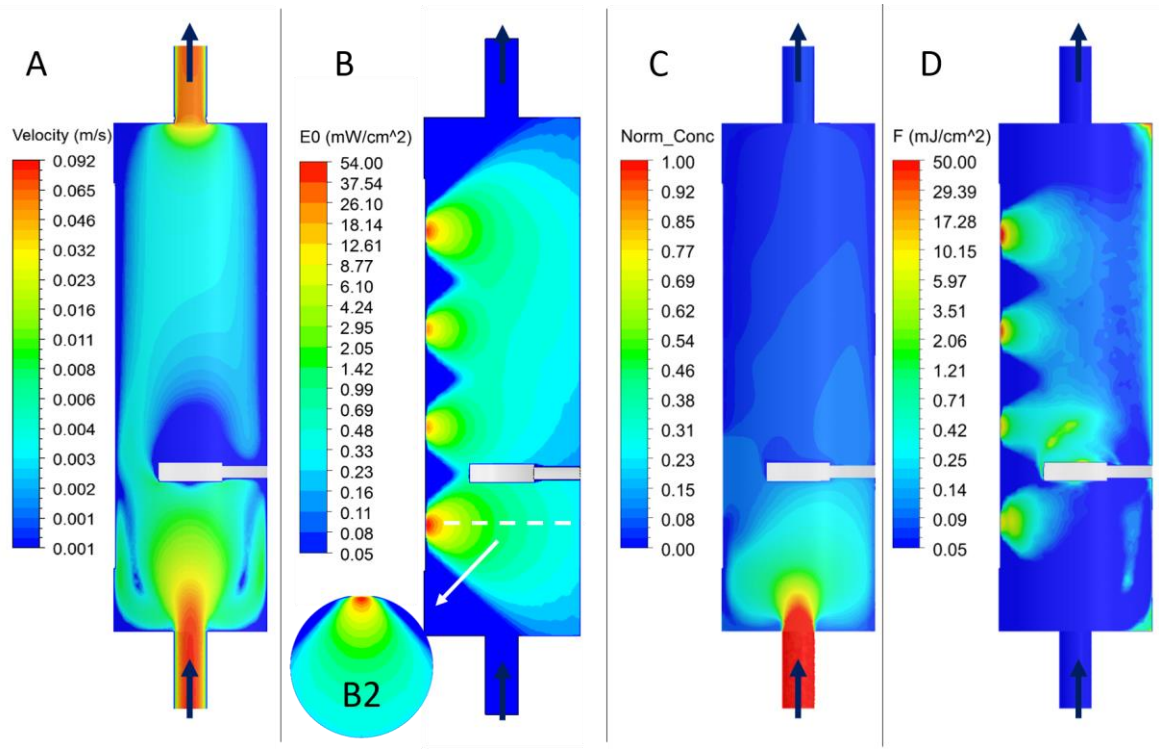

Figure 30. The distribution of velocity (A), fluence rate (B), normalized concentration (C), and local fluence (D) on the central longitudinal cross section of reactor2 at the flow rate of 250 ml/min. B2 shows the fluence rate of LED4 on the lateral cross section.

As explained earlier, the local performance of a UV reactor equates with local fluence. In this study, a computational cell that receives low fluence is called dark cell, and a series of dark cells is called a dark channel. A dark channel forms either when fluid residence time is extremely short or local fluence rate is negligible. Not every dark channel has the same negative impact on the performance of a UV reactor. The one that bridges between the inlet and outlet drastically

reduces overall disinfection efficiency because such channel by-passes a large number of microorganisms. For example, the central part of Reactor-1 (Figure 27-D2), which has low local fluence, bridges between inlet and outlet and diminishes the overall performance. The diffuser impedes the formation of the channel by deviating the water; consequently, the dark blue region around the central part of Reactor-1 (Figure 27-D) disappears in Reactor-2 (Figure 30-D). However, the local fluence is not uniformly distributed across Reactor-2. For example, the delivered fluences are greater near UV-LEDs (high fluence rate) and the back of the diffuser (high residence time) than the rest of the reactor.

Although the central dark channel of Reactor-1 disappears in Reactor-2 due to the diffuser, the dark regions that form because of the low radiant energy remain unchanged in Reactor-2 (Figure 30-B). For example, the areas that lie beyond the radiation cone of UV-LEDs receive low fluence rate (dark blue contours in Figure 30-B2). The dark areas between UV-LEDs on the longitudinal cross section (Figure 30-B) and the lateral cross section (Figure 30-B2) have different impacts on the overall performance. Microorganisms that pass through the dark areas between UV-LED on the longitudinal cross section have a chance of being exposed to UV along their trajectories. In contrast, microorganisms that pass through the lateral dark areas are not exposed by UV along their path because UV-LEDs are in a row and the dark area of one UV-LED is not irradiated by another one. It should be noted that since the body of the reactor is not reflective and most of the radiation energy is lost at the reactor's internal surfaces, the reflection has a negligible impact on the received energy, particularly in the lateral dark regions (Figure 30-B).

Iso-volume is the volume of the numerical domain that lies in a specific range. Figure 31-A shows the regions (iso-volume) with the normalized concentration of 0.1–1 across the reactor-2 at 250 ml/min. There is a strong correlation between the position of dark regions on the

lateral cross sections and the highly concentrated stream of microorganisms (pink color in Figure 31-B). Such correlation implies the importance of the concentration profile in recognizing the worst dark channels in the UV reactor, which is essential information for reactor modification.

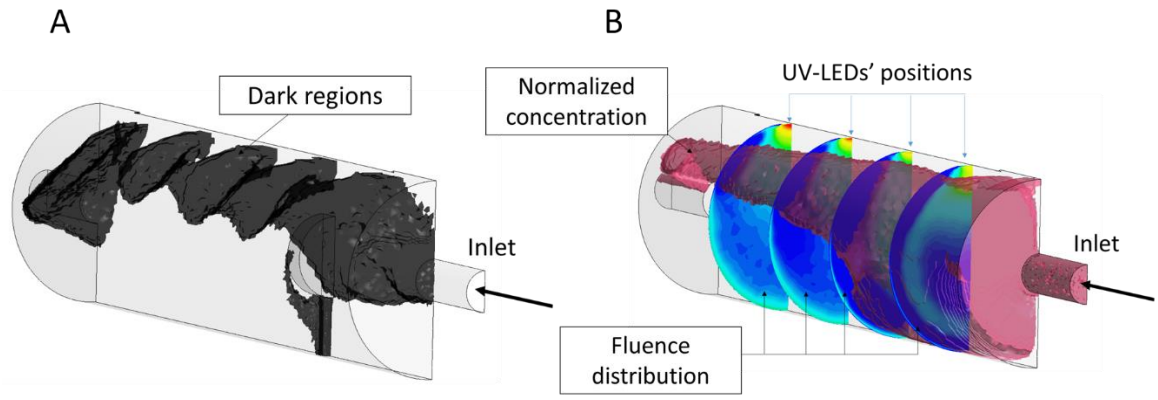

Figure 31. The dark regions in Reactor-2 at the flow rate of 250 ml/min is shown (A). The dark regions form when the amount of the local fluence is negligible. (B) shows the iso-volume of normalized concentration with a value of 0.1–1 across reactor-2. The distributions of fluence on four lateral cross sections are shown (B). There is a strong correlation between the position of low fluence areas on the lateral cross sections and the highly concentrated stream in reactor-2.

4.4 Summary

In this study, UV-LED reactors were simulated in the Eulerian framework and evaluated experimentally. The germicidal factors of UV-LEDs were calculated and used for homogenizing the outputs of UV-LEDs. This practical approach reduced the complexity of the simulation and eliminated the necessity of developing kinetic data for each UV-LED. The successful predictions showed the ability of the proposed method for UV-LED reactor simulation.

In this study, the performance of UV-LED reactors was discussed in detail. It was shown that the overall performance of a UV-LED reactor is influenced by the delivered fluence to each computational cell. The local fluence determines the performance of each part of a UV reactor.

This quantity is crucial for identifying and eliminating the low performing regions inside the reactor. It was shown that a series of low performing computational cells coincides with a highly concentrated stream of microorganisms; therefore, such regions should be modified either by a flow modifier or new UV-LED arrangement.

Chapter 5: The application of the reactor performance model

5.1 Introduction

Chapter 4 showed that the reactor performance improved once the uniformity of local fluence inside the reactor increased. The fluence is the product of fluence rate and the residence time, and since the residence time is inversely related to the local velocity, it can be inferred that local velocity and local fluence rate need to be proportionate to establish a uniform fluence across the reactor. When a uniform fluence across the reactor is established, the reactor behaves ideally. Theoretically, the ideal UV reactor delivers the ultimate fluence (F_U); however, due to practical limitations, it is not feasible to attain such performance practically.

Achieving the ideal performance from a UV reactor depends partly on the mode of irradiation. In the context of UV-LED reactor design, the modes of the irradiation of water can be categorized as cross-irradiation and parallel-irradiation. The cross-irradiation mode refers to the condition that the dominant direction of the fluid movement and UV rays are normal to each other (Figure 32), whereas, UV rays and the fluid are in the same direction in the parallel-irradiation (Figure 32). Since UV-LEDs are typically installed on the reactor wall, cross-irradiation is prevalent [e.g., 37, 45]. Since radiant energy intensity and fluid velocity distribution are inherently disproportionated in cross-irradiation, this type of water irradiation does not lead to the ideal performance. On the other hand, the parallel-irradiation aligns well with the concept of velocity-radiation proportionality and promise higher efficiency. One study has applied parallel-irradiation to a UV-LED reactor with a transparent body [77]; however, no solution was proposed to eliminate the dissipation of the radiant energy to the reactor which happens because of the UV rays divergence.

In order to retain the photons within the reactor, the internal surfaces of the reactor need to be reflective or UV rays could be collimated along the water direction. This chapter proposes two UV-LED reactors that retain UV energy within the reactor as stated above and apply the integrated model to study the efficacy of such design concepts.

Furthermore, the concept of ideal UV-LED reactor is discussed in this chapter. Since an ideal UV-LED reactor produces the maximum fluence, by comparing the REF, which is obtained through the experiment, with the maximum fluence derived through simulation, the room for the design modification is recognized.

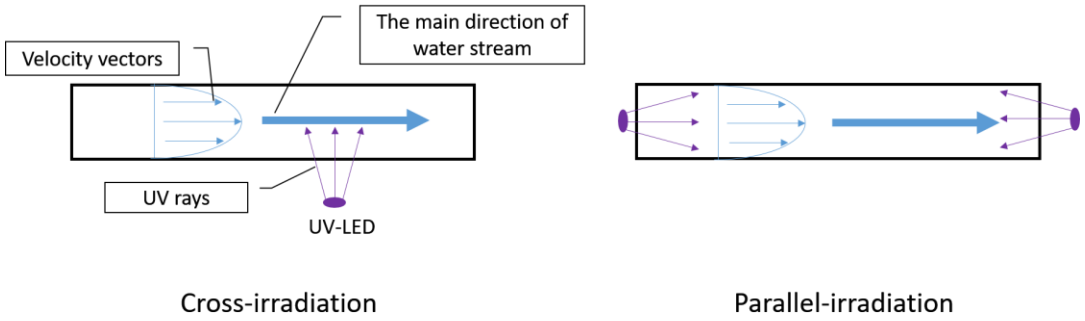

Figure 32. The schematic of the cross-irradiation and the parallel-irradiation. The cross-irradiation refers to the condition that the dominant direction of the fluid movement and UV rays are normal to each other (Left). The parallel-irradiation refers to the condition that UV rays and the fluid movement are in the same direction (Right).

5.1.1 Ideal UV reactor

The inactivation of microorganisms in a UV reactor is a function of delivered UV fluence to microorganisms, and UV fluence is the product of fluence rate and exposure time. An ideal UV reactor delivers the same fluence to all microorganisms, while a non-ideal UV reactor delivers a wide range of fluences to the water flow. A completely mixed batch reactor which harvests all the photons for the inactivation represents an ideal UV reactor. However, it is extremely difficult to

reach the ideal performance of a flow-through UV-LED reactor because radiant energy must be proportionated with the velocity distribution to reach uniform UV fluence distribution. This means that microorganisms with higher velocities (short residence time) should be exposed to higher fluence rates.

A continuous stirred-tank reactor (CSTR) or a plug flow reactor (PFR) that harvests all the photons for microbial inactivation are two types of ideal flow-through UV-LED reactors. In a CSTR, the microorganism suspension is well mixed. Thus, even if the radiation distribution is non-uniform, all the microorganisms will be exposed to the same level of radiant energy. As for the PFR, since all the microorganisms spend the same time in the reactor and the reactor is radially completely mixed, they receive the same fluence regardless of the radiation distribution inside the reactor. One example for the PFR could be a cylinder equipped with a collimator lens that without energy loss captures and collimates all the photons over the cross section of the PFR (Figure 32). In such PFR, the UV rays and the fluid have the same direction, resulting in optical length (Λ) and reactor length (L) have the same value. Here, the distance that the UV rays travel before leaving the reactor is called optical length (Λ). In the following section, this virtual reactor is used to derive a mathematical formula for calculating the maximum possible deliverable fluence in a reactor. Here, the maximum possible deliverable fluence is called the ultimate fluence (F_U).

5.2 Approach for the determination of an ideal UV-LED reactor efficiency

When all the photons are collimated, the fluence rate on the pipe cross section will be equal to $\frac{\mathrm{P}}{\mathrm{A}}$ where P (W) and A (m^2) are the sum of each UV-LED's germicidal output powers and the area of pipe's lateral cross section, respectively. In a plug flow reactor, hydraulic retention time (HRT (s)) is $\frac{\mathrm{A} \cdot \mathrm{L}}{\mathrm{Q}}$, where L (m) is the length of the reactor and Q ($\frac{m^3}{s}$) is the flow rate. In such PFR,

all the microorganisms will remain in the reactor for the same time equivalent to HRT, and they receive fluence rate of P/A ($\frac{W}{m^2}$) (assuming there is no absorption in the medium). Considering the effect of the UV absorption in water, fluence ($\frac{J}{m^2}$) at each cross section with the thickness of Δx will be equal to $\frac{P \cdot \Delta x}{A} 10^{-\alpha \cdot x}$ (or $\frac{P \cdot \Delta x}{A} e^{-\ln(10) \cdot \alpha \cdot x}$) where x (m) is the distance from the one end of the pipe, where the radiation is emitted to the fluid (Figure 32), and α ($\frac{1}{m}$) is the UV absorption coefficient of the water. In this regard, this reactor will deliver the fluence of $\int_0^L \frac{P \cdot dx}{Q} e^{-\ln(10) \cdot \alpha \cdot x}$ to the microorganism up to the length of L. If the absorption coefficient is zero, the maximum delivered fluence would be $\frac{P \cdot L}{Q}$. However, taking into account the UV absorption of water (not 100% UV transmittance), the following equation represents the maximum delivered fluence in a cylindrical reactor without reflective walls.

$$F(L) = \frac{P}{Q} \cdot \frac{1 - 10^{-\alpha \cdot L}}{\ln(10) \cdot \alpha} \qquad (18)$$

In Equation 18, another perspective can be considered the logarithmic mean of power ($\bar{P}$) along the reactor length reaches to the microbial suspension. Therefore, $F(L)$ will be equal to $\frac{\bar{P} \cdot L}{Q}$, where $\bar{P}$ is equal to $\frac{P \cdot [1 - 10^{-\alpha \cdot \Lambda}]}{\ln(10) \cdot \alpha \cdot \Lambda}$, P is the germicidal power of the UV-LED source, and Λ (optical length) is equal to L in this configuration.

If the length of the PFR is infinite, then all the UV energy is cultivated for the inactivation and the reactor delivers ultimate fluence (F_U) which is equal to $\frac{P}{\ln(10) \cdot \alpha \cdot Q}$. In this view, the ultimate fluence is a function of germicidal power (P), flow rate (Q) and absorption coefficient (α), which

all are available prior to the reactor design, so the ultimate fluence can be estimated for a given UV-LED reactor by knowing the aforementioned parameters.

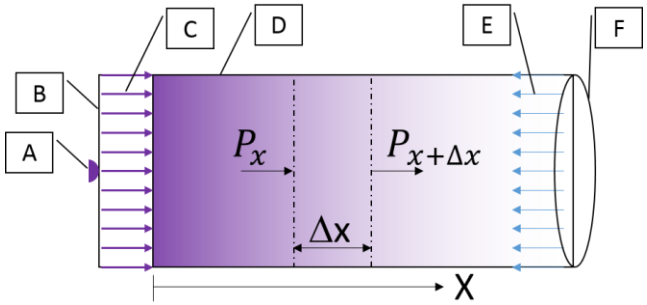

Figure 33. The schematic of an ideal plug flow UV-LED reactor. The radiant power (i.e., P) is uniformly distributed across the lateral pipe cross section (F), and it is decreasing along the pipe length (i.e., X-axis) due to absorption. A UV-LED (A), a collimator lens (B), collimated UV rays (C), longitudinal cross section of the reactor (D), velocity vectors (E), and the lateral cross section of the pipe (F) are shown in this figure.

A general approach can be taken to the quantification of the maximum deliverable fluence of a non-ideal UV reactor with a known geometry and fluence rate distribution. For such a reactor, the maximum performance takes place when all the microorganisms are exposed to the volumetric average fluence rate for a time span equal to the hydraulic retention time (HRT) of the reactor (i.e., $\frac{V}{Q}$, where V is the reactor volume and Q is the flow rate). Such performance could be obtained if the fluid is completely mixed within the reactor. Hence, by calculating the volume-weighted average fluence rate ($\bar{E}_0$), the maximum deliverable fluence resulting from the mixed flow assumption (F_{max}^H) is equal to $\bar{E}_0$ multiplied by HRT.

The main application of Equation 18 is, however, the calculation of the input power ($P_{input}\ (W)$) in order to obtain a specific target fluence (REF). For this purpose, germicidal power needs to be converted to the radiant power. As explained above, the germicidal power of a UV source is the product of its radianit power and germicidal efficiency ($\overline{GE}$), so the radiant power

can be calculated knowing the the germicidal efficiency. In addition to the germicidal efficiency, the wall plug efficiency (WPE) of the UV source should be considered because a portion of input power converts to radiant energy and the rest is lost as heat. Taking all the factors into consideration, the following equation describes input power which is needed to obtain the desired fluence from an ideal UV reactor.

$$\frac{1}{\mathrm{P}_{input_{ideal}}} = \frac{1}{F_U}\frac{(\overline{GE}\cdot WPE)}{\mathrm{Q}}\frac{1}{\ln(10)\cdot\alpha} \qquad (19)$$

The design efficiency (η) (Equation 20), which represents the ratio of REF to F_U , can be integrtaed into Equation 19 to yield the power requirement based on the target fluence.

$$\eta = \frac{REF}{F_U} \qquad (20)$$

By substituting Equation 19 in Equation 20, the input power needed to deliver a particular fluence to microorganisms in a real UV reactor is obtained (Equation 21).

$$\mathrm{P}_{input\_real} = \frac{REF}{\eta}\cdot\frac{\ln(10)\cdot\alpha\cdot Q}{(\overline{GE}\cdot WPE)} \qquad (21)$$

The innate differences between UV sources pertain to their germicidal factors and wall plug efficiencies. The difference between UV reactors, however, relates to their design factor (i.e., η). As inferred from Equation 21, a decent UV source has higher WPE and $\overline{GE}$, leading to a greater design efficiency (η). Since UV-LEDs have a flexibility in emanating the desired wavelength, they offer higher $\overline{GE}$ compared to LP UV lamps. In addition, they promise better radiation-hydrodynamics interaction (higher design efficiency). Currently, the WPE of UV-LEDs are less efficient than LP UV lamps. However, this ever-growing technology has reached 4% WPE [18] and recent breakthroughs in material science—utilization of graphene as the substrate of UV-

LED [20]— promise even higher efficiencies (~45%) [21], which is greater than that of LP UV lamp (~35%).

5.3 The implication of the CFD tool to design concept

As discussed earlier, the ideal PFR or CSTR that cultivate all photons for microbial inactivation are two examples of the ideal UV-LED reactors. To retain photons inside the reactor, the internal surfaces of the UV-LED reactor must be reflective. The impact of the internal surface reflectivity on the enhancement of the batch UV-LED system has been studied [43,61]; however, the challenge is to harness the reflection to design a flow-through UV-LED reactor properly. Another method for cultivating the radiant energy for microbial inactivation is irradiating the water inside an elongated PFR using an ideal collimator lens. In such reactor, UV rays are absorbed by water over the length of the PFR, and the photons are not dissipated to the walls, thereby all the photons are employed for the water disinfection. This concept was studied theoretically in the previous section under ideal PFR and collimation assumption. Since an ideal PFR and ideal collimator lens are unattainable, the integrated model can be applied to study the aforementioned design concepts to provide insight into their actual performance.

5.3.1 Assumptions

To establish ideal hydrodynamics-radiation interaction, a cylindrical reactor equipped with one UV-LED at one end of the pipe was chosen for a case study in this section. Further, two concepts of reflection and collimated rays are applied to the base model to investigate their impacts on the overall performance.

The dimensions of the UV-LED reactors for the case study are shown in Figure 34. The UV-LED is separated from the water using a quartz window (1.5 mm) in Reactor-1 (base model) and Reactor-2 (reflective reactor), while a Fresnel lens is used for the separation in Reactor-3

(collimated rays reactor) (Figure 34). UV-LED is placed at the focal length (1.5 cm) of the Fresnel lens, and there was not a reflector to return to water the UV rays that did not hit the lens. Although the collimation of rays can be obtained utilizing a combination of two or more lenses, a Fresnel lens is used to establish collimated rays in this study.

The internal surface of Reactor-2 was modeled as a reflective surface with a diffusive coefficient of one, whereas the walls of Reactor-1 and Reactor-3 were UV absorptive. The flow rate of 2000 mL/min was selected for this study and *E. coli* was chosen as a challenge organism. A UV-LED with the germicidal power of 25 mW was used as the radiation source when UV transmittance of water was set to 95%. The chosen UV-LED was twice as powerful as the LED1 in Chapter 4. This selection allows comparing the result of this chapter with those of Chapter 4.

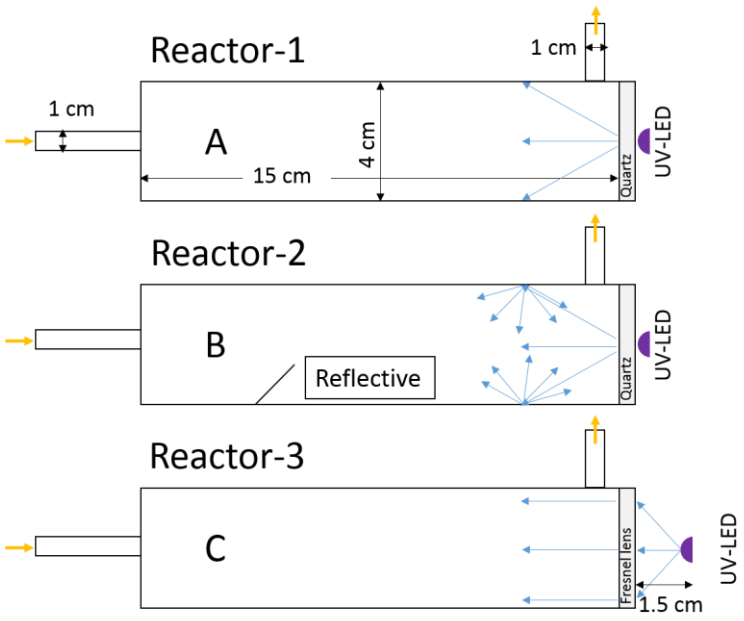

Figure 34. Three cylindrical UV-LED reactors each contain one UV-LED are shown. The wall of Reactor-1 (A) is absorptive, whereas, Reactor-2 (B) has a reflective wall. Reactor-3 (C) is equipped with a Fresnel lens that collimates UV rays.

5.3.1.1 Numerical method

The distributions of fluence rate in UV-LED reactors are different. The radiant energy field of Reactor-1 was obtained by considering all the main phenomena that impact ray propagation. As for Reactor-2, in addition to direct radiation, the effect of reflected rays was considered. Since the internal surface of Reactor-2 was reflective with a diffusive coefficient of one, the irradiance on each cell on the wall was initially calculated, and then the reflected energy was uniformly distributed across the domain. With regards to Reactor-3, the irradiance on the surface of the Fresnel lens was initially calculated, and the reflected energy was deducted from the incident energy and the remaining energy was collimated along the pipe axis (Figure 35), by taking into account the absorption of water and reflection at the lens-water interface. Since all the UV rays emanated from UV-LED do not hit the lens and get collimated, the amount of delivered UV energy to the water is less than that of Reactor-1 and Reactor-2.

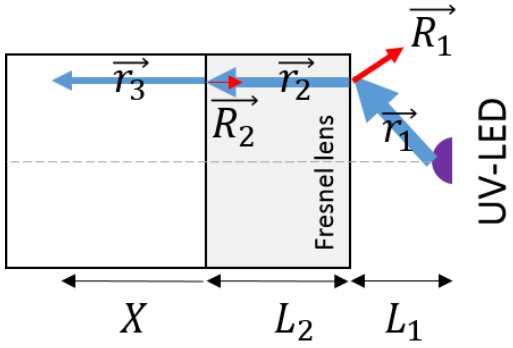

Figure 35. The schematic of the propagation of UV ray in Reactor-3. UV rays are shown in blue, and the reflected rays are shown in red. L_1 is the focal length of the Fresnel lens, L_2 is the lens thickness, x is the distance that a UV beam travel in the water.

The procedure of UV-LED reactor simulation was explained in Chapter 4. The same approach was employed to simulate the cylindrical UV-LED reactors in this chapter (Figure 34). In short, the geometry was discretized into 355359 tetrahedral cells, and the realizable $k-\varepsilon$ model

with scalable wall function was chosen from hydrodynamic sub models. The velocity-inlet and pressure-outlet, no-slip boundary conditions were assigned to the inlet, outlet and the reactor's walls, respectively. The convergence of the results was approved once the errors of two successive iterations for the scaled residuals were less than 10^{-6}.

5.3.2 Results and discussion

Figure 36 shows the velocity profile on the longitudinal cross section of the reactors. As seen, velocity profiles even out and the impact of pressure difference diminishes as water moves toward the outlet. The principal direction of the water is from left to right; however, when water moves upward to leave the reactor, the main direction is inclined upward, which further contributes to the non-ideal flow in the reactor. Another aspect of non-ideal flow relates to water recirculation shown by red-dashed lines in Figure 36. In such areas, water residence time is relatively longer than the central part, and microorganisms are exposed to a higher amount of UV energy.

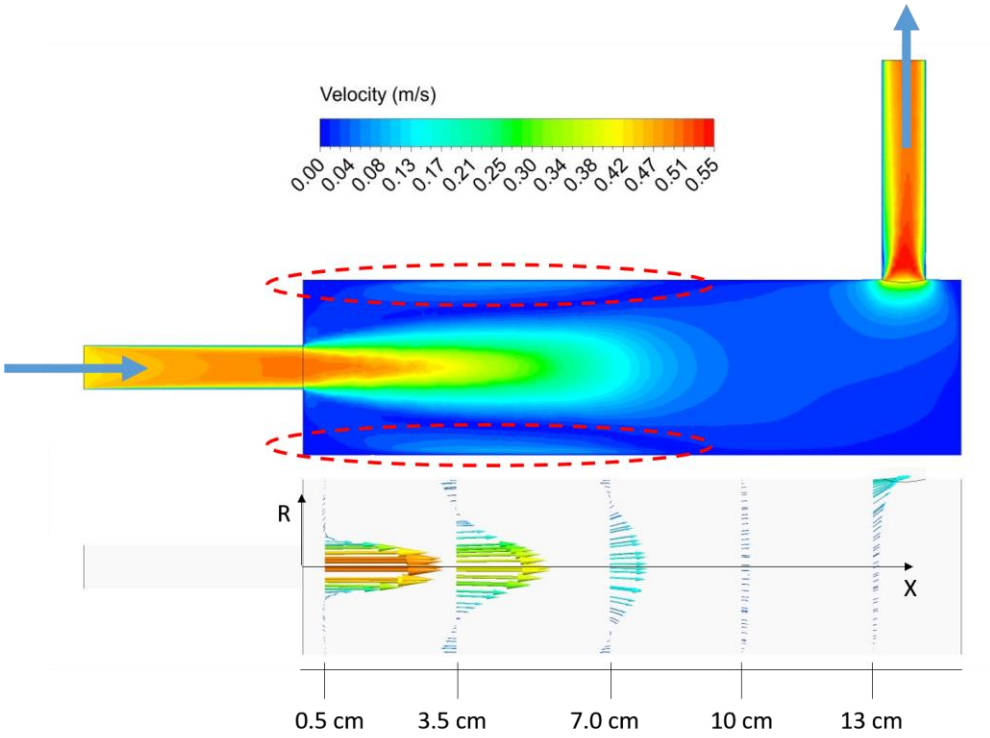

Figure 36. The velocity contours (A) and velocity vectors (B) on the longitudinal cross section of the UV-LED reactors.

Figure 37 shows the fluence rate distribution on the longitudinal cross section of the reactors. UV-LED irradiates the water in parallel mode with higher UV energy near the UV source. The fluence rate decreases along the pipe length, but its uniformity increases across the lateral-cross sections (Figure 37-A). The UV energy around the center is higher which is in accordance with the concept of ideal velocity-radiation interaction. However, UV rays diverge in short distances in Reactor-1, so the photons hit the wall and are eliminated at the end of their trajectories. Due to that, a large portion of emanated energy does not effectively contribute to the inactivation. The photons that are lost to the reactor wall in Reactor-1 are retained in Reactor-2 through the surface reflection. The increase in the magnitude of fluence rate in Reactor-2 shows the impact of

reflected rays (Figure 37-B). Although UV energy is preserved, still the fluence rate near the wall is higher than that of the center, which does not match well with velocity distribution.

Figure 37-C illustrates how parallel rays produce the fluence rate distribution in Reactor-3. The ideal collimator lens used in this case, collects rays and aligns them with the pipe axis. As a result of such behavior, the entire pipe is irradiated, and the gradient of UV energy along the pipe axis is much less than those of Reactor-1 and/or Reactor-2. This behavior exceptionally improves the uniformity of local fluence across the reactor (Figure 37-C). Since the profile of UV-LED is the balloon shape (Figure 10), the highest amount of UV energy is observed at the center. The UV rays lose their energy along their pass due to the absorption; therefore, the fluence rate contours taper as they progress toward the inlet. The simulation showed that 22% of radiant energy emanated by UV-LED does not hit the Fresnel lens in Reactor-3; therefore, the amount of delivered energy to Reactor-3 is less than that of either Reactor-1 or Reactor-2. Nonetheless, the radiant energy field is well matched with the velocity contours in Reactor-3 so that microorganisms with higher velocity are exposed to a higher amount of UV rays.

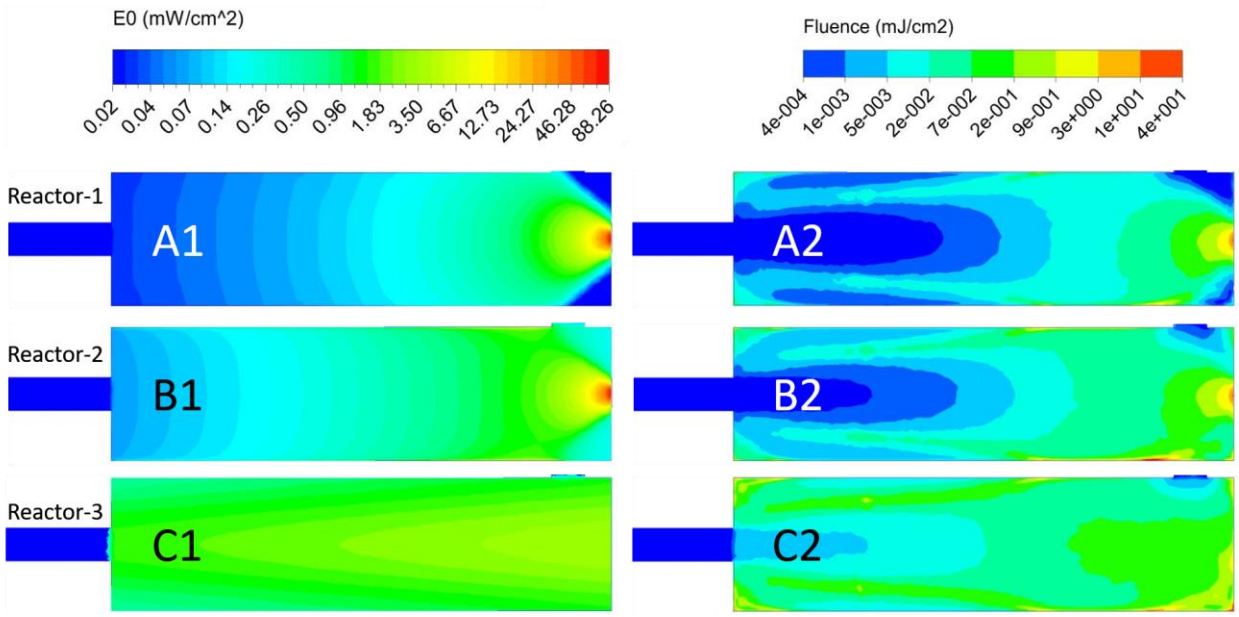

Figure 37. The fluence rate (left) and local fluence (right) distributions on the longitudinal cross sections of the three UV-LED reactors.

Figure 37 shows the local fluence (local performance) on the longitudinal cross sections of all the reactors. Reactor-1 local fluence profiles (Figure 37-A2) reveals that the incoming flow receives low fluences near the inlet as a result of short residence time. However, the reactor performs better as fluid moves toward the outlet so that the maximum local fluence is seen near the UV-LED. In comparison to Reactor-1, Reactor-2 delivers higher fluence and diminishes the extent of the low-performing region. The impact of reflection is evident, particularly near the walls in which the fluid has higher residence time. Figure 37-C2 shows the local fluence of Reactor-3, and in comparison with two other reactors, the water receives the comparably higher amount of UV energy near the inlet; and the reactor performs even better as water flows toward the other end of the reactor. Reactor-3 has the highest fluence uniformity among all (Figure 37-C2), and the radiant energy field is well matched with velocity profile.

The profile of microorganisms' concentration across the reactor illustrates how water is treated along the pipe (Figure 38). A large portion of the volume of Reactor-1 and Reactor-2 contain water with highly concentrated microorganisms (red color), while much of the inactivation occurs near the UV-LED. This shows the susceptibility of such reactor designs because a small change in hydrodynamics drastically reduces their ability to treat water. In contrast, Reactor-3 effectively disinfects the water along the pipe so that when the velocity profile becomes approximately uniform across the lateral cross section (x~10 cm in Figure 36), the concentration contours fade out linearly with respect to the pipe axis (Figure 38-C). Such behavior suggests that a more elongated pipe promise even higher design efficiency as a result of higher fluence uniformity.

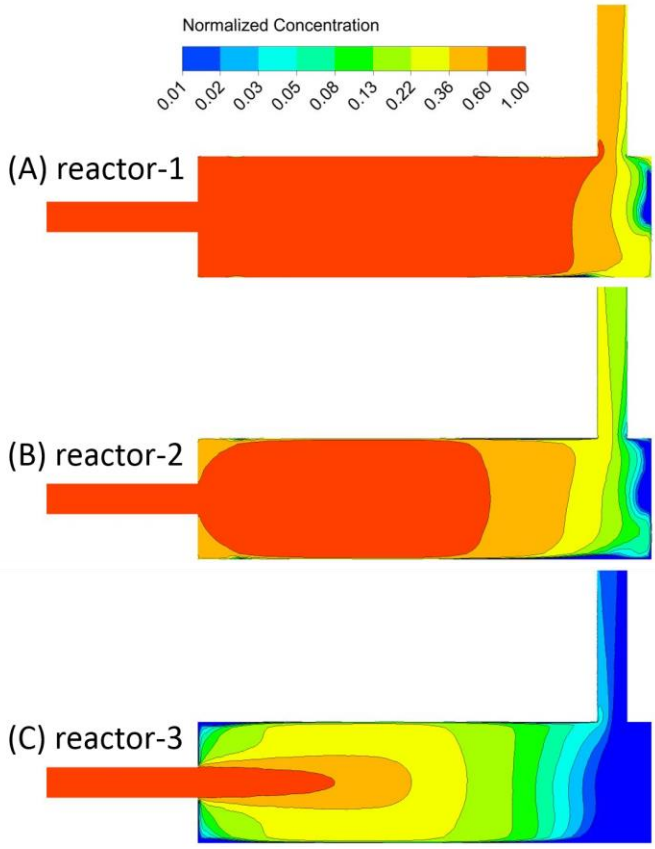

Figure 38. Concentration profile on the longitudinal cross sections of the three reactors

Figure 38 shows the log inactivation and their efficiency with respect to their corresponding ultimate fluence. The simulations showed that Reactor-1 could disinfect *E. coli* up to 0.35 log at the flow rate of 2000 ml/min. The result signifies the efficacy of parallel irradiation if the log-inactivation is compared with what was observed during cross-irradiation in Chapter 4, where the reactor comprised 4 UV-LEDs (~43 mW) and could treat the water up to 1 log at 150 ml/min. Although ~43 mW was delivered to Reactor-1, the log inactivation was less than that of Reactor-3. The reflection and collimation enhanced the performance of Reactor-1 approximately two and four times, respectively. However, based on this result, it cannot be concluded that reflection alone always leads to lower performance because a well-mixed reactor with a reflective wall could be an ideal UV reactor. According to the behavior of a CSTR, improving the mixing in a reflective UV-LED reactor is a practical approach to attain higher performances. Nonetheless, the reflection is prone to bio-fouling which changes the characteristics of the reactor and decreases its performance drastically. Besides, the desired radiation profile may not be achieved through reflection.

Table 6 shows that a 15-cm plug flow reactor with the collimated rays could deliver the fluence of 7.86 $\frac{mJ}{cm^2}$, which is approximately the half of the ultimate fluence (14.67 $\frac{mJ}{cm^2}$). This calculation shows that up to the length of 15 cm, only ~50% of total energy is cultivated for the inactivation, suggesting that increasing the length of the reactor improves the delivered fluence. Table 6 presents that Reactor-3 exhibited 33% of the performance of an ideal reactor, which shows significant improvement compared to the other reactors. In the configuration of Reactor-3 due to the divergence of UV rays emanated from UV-LED, 22% of UV energy does not hit the Fresnel lens, thereby do not contribute to the radiant energy field. It is expected that any effort to capture and collimate all the photons results in higher performance. One suggestion could be utilizing a

reflector that captures and returns UV rays. Note, since the reflected rays would hit the Fresnel lens with new incident angles that may not be optimum, the ultimate performance will not increase by 22%.

Table 6. Reduction equivalent fluence (dose) and the design efficiency of the three reactors

	Log-inactivation	REF (mJ cm^{-2})	$\eta = \frac{REF}{F_U}$
Reactor-1	0.35	1.29	0.087
Reactor-2	0.71	2.63	0.179
Reactor-3	1.95	4.88	0.332
15-cm Plug flow reactor with collimated beams		7.86	
Ideal reactor †		14.67	

Absorption coefficient=0.0222 [cm^{-1}] equivalent to 95% UVT

Germicidal power= 25 [mW]

Length= 15 [cm]

Flow rate= 2 [L/min]

† an infinite length plug flow reactor with collimated beams or a well-mixed reactor with fully reflective internal surfaces

5.4 Summary

The concept of velocity-radiation proportionality was defined, and an ideal performance was built upon that concept. The concept of parallel-irradiation which leads to a better hydrodynamics-radiation interaction was introduced, and the integrated model was employed to show the efficacy of parallel-irradiation mode.

The study of the ideal UV-LED reactor opened doors to the advent of new conceptual designs such as reactors with reflective internal surfaces and collimated UV rays which promise higher efficiency. The study of ideal UV-LED reactors led to the development of a mathematical formula to calculate the maximum fluence of a UV-LED reactor. The formula was used for the

calculation of the power consumption once the wall plug efficiency and germicidal efficiency of UV-LED were taken into account.

Three cylindrical UV-LED reactors were simulated when the internal surface of Reactor-1 and Reactor-3 were UV absorptive, while Reactor-2's internal surface was reflective. The radiation profile of the UV-LED in Reactor-3 was modified using a Fresnel lens. The simulation results showed that the UV-LED reactors with reflective internal surfaces and collimated rays, in turn, could deliver two and four times higher fluence compared to Reactor-1. Reactor-3 could reach 33% of the ultimate fluence despite the fact that 22% of the radiant energy did not hit the Fresnel lens and did not get into the reactor. The analysis of the fluence distribution of Reactor-3 suggested that a more extended reactor could increase fluence uniformity and ultimately higher design efficiency.

The concepts proposed in this chapter can be employed to design more efficient reactors, and the intergraded model can be applied to study their performance under real operating conditions.

Chapter 6: Conclusions and recommendations

This study developed an integrated model for simulating UV-LED reactors for water treatment. The integrated model needs three prerequisite models (hydrodynamic, radiation, and kinetic) to predict the overall performance of a UV-LED reactor. In this study, the appropriate hydrodynamic model was selected according to the prior works in our research group. The method for simulating UV-LED radiation was proposed and evaluated experimentally. The method for estimating the UV-LED microbial inactivation was proposed and examined using *E. coli* and MS2 in different operating conditions. The prerequisites models were integrated into a commercial CFD software package (ANSYS FLUENT) to simulate the performance of UV-LED reactors. The robust CFD-based model could successfully predict the performance of UV-LED reactors under various operating conditions such as different flow rates, flow regimes, UV-LED outputs, and UV-LED configurations. The reliable CFD-based model can be utilized as an engineering tool to design, optimize, scale-up similar UV-LED reactors. In the following, the general conclusions derived from this research study are presented.

A general method for the prediction of the fluence rate within a UV-LED reactor was developed by considering an actual UV-LED's radiation profile, Snell's and Fresnel's laws through the propagation of UV rays, and the reflection from internal wall surfaces. The UV-LED was modeled as a polychromatic radiation source, and the impact of the UV-LED emission spectrum on the quartz absorption coefficient and microorganism's inactivation were studied. The results showed that UV-LEDs with larger wavelength than 265 nm could be assumed as monochromatic during the calculation of the quartz absorption coefficient. Moreover, the quartz had a negligible impact on the emission spectra of UV-LEDs with peak wavelengths larger than 265 nm. The experimental measurements showed that UV-LED radiation profiles are not

symmetric with respect to the UV-LED normal vector. However, statistical analysis showed that the symmetric assumption could yield acceptable predictions.

The evaluated radiation model was applied to predict the delivered fluence rate to the microbial suspension when the UV-LED was ~1.5 cm above the petri dish to produce high fluence rate. The simulation results showed that the reflection from the water surface was different and the fluence rate was non-uniform across the petri dish. The analysis of reflection from internal walls revealed that a negligible amount of UV reflects back to the water and the reflection effect can be ignored during the fluence rate calculations. The close agreement between the actinometry data and numerical predictions derived based on the polychromatic assumption implied that the entire emission spectrum of UV-LED needs to be considered to improve the accuracy of the fluence rate prediction.

During the kinetics studies, the gently mixed microbial suspension was exposed to UV for different time periods to receive pre-determined fluences. The experimental fluence rate in the microbial suspension was back-calculated by considering the germicidal efficiency of UV-LEDs. The comparison between the numerical predictions and experimental data showed that when the exposure time became longer than 200 seconds, the experimental fluence rate approached the numerical fluence rate so that their differences reduced to less than 5%. Since numerical predictions were derived based on the completely-mixed assumption, the significant deviations between the numerical and experimental data in the shorter exposure times were related to the mixing as the water inside the petri dish was not well-mixed. Therefore, the output power of a UV-LED must be adjusted prior to the experiment in such a way that a long exposure time (e.g., 200 s) is needed to deliver the target fluence. This conclusion was drawn based on the non-uniform

fluence rate distribution in the 5 cm and 9 cm petri dishes. It should be noted that if the fluence rate uniformity increases, it is expected that shorter exposure times lead to reliable kinetics data.

The main conclusion drawn from this study was the use of the germicidal efficiency—derived based on the polychromatic assumption and the action spectra—could yield reliable kinetics information. Thus, the inactivation effect of UV-LEDs with different wavelengths can be estimated without experimental studies, which has real-life applications when a reactor of different UV-LEDs is to be simulated.

Once the prerequisites models for the development of the integrated model were developed, the performance of two cylindrical UV-LED reactors was simulated using the integrated model. The simulations could predict the inactivation of *E. coli* and MS2 in continuous flow reactors under different operating conditions, showing the capability of the proposed method. The simulation of the reactors in the Eulerian framework facilitated the analysis of the behavior of the reactor, resulting in identifying the areas with low performance. The analogy of each computational cell to a well-mixed UV reactor allowed to define the local performance of a UV reactor based on the delivered local fluence. This study showed that the negative impact of low-performing regions could be different, and the concentration profile and/or accumulated fluence shows which poorly-performed region has the worst impact. This study showed that by modifying the hydrodynamics of the reactor, the delivered fluence increased ten times, implying the capability of the integrated method for design modification. The general guideline proposed in this study can be applied to other similar photoreactors to improve efficiency.

The analysis of cross-irradiation and parallel-irradiation modes showed that parallel-irradiation could result in higher efficiencies. Therefore, two reactors based on parallel-irradiation concept were introduced, where reflective surfaces and collimated rays were two ways of

improving the radiation distribution in cylindrical reactors. The irradiating the water using the collimated rays, due to a better fluence uniformity, resulted in higher efficiency in such a way that the reactor could achieve 33% of the ultimate fluence. The efficiency of the cylindrical reactor with the collimated rays was almost two times higher than that of the reflective reactor. If the water is well-mixed inside the reflective reactor, the performance will rise. However, the reflective surfaces are prone to biofouling, which drastically reduce the overall performance.

6.1 Recommendation

This study used realizable $k-\epsilon$ with along with wall functions (e.g., enhanced wall treatment and scalable wall function) to simulate the flow field according to the prior works in our research group. Since the validity of the hydrodynamic model is crucial for simulating the reactor, it is recommended to perform experimental studies to evaluate the numerical predictions, particularly for high Reynolds numbers.

The integrated model could reliably predict reactor performance. It is recommended to couple the integrated model with an optimization routine to find the optimum performance of a UV-LED reactor for a given design criterion.

The radiation model is applicable to a clear fluid where the scattering effect is negligible. When there are particles in the water or the turbidity of the water is low, the proposed radiation model may not predict the fluence rate inside the reactor accurately. If the distribution of particles across the reactor is known, through an iterative procedure the scattering effect can be captured. However, such process is computationally intensive. It is recommended to develop an efficient algorithm to simulate the propagation of rays considering scattering effect. Such a model could have applications in wastewater treatment processes.

The radiation distribution of a UV-LED reactor can be modified using optical lenses. The current model considers Snell's and Fresnel's laws during the propagation of rays. However, it was not utilized to predict the radiation distribution when an optical lens alters the UV-LED's radiation profile. It is recommended to apply the algorithm proposed in this study to simulate the effect of an optical lens on the radiation distribution and evaluate the predictions experimentally.

The radiation model developed in this study is applicable to systems that have a clear fluid with a constant absorption coefficient. Once photoreaction takes place within the photoreactor and the photo-products have significantly different absorption coefficient, the accuracy of the predictions based on the proposed model drops sharply. Therefore, the absorption coefficient across the reactor needs to be updated simultaneously throughout the simulation. This requires an iterative process in which the concentration profile is achieved, and then the radiation profile is updated to update a new concentration profile until the changes in concentration and radiation profiles become negligible. In each iteration, the mentioned iterative process needs to be implemented. The proposed method to simulate such a system is time-consuming, so it is recommended to develop an efficient algorithm to update radiation profile reliably in a time efficient manner.

Bibliography

[1] J.R. Bolton, C.A. Cotton, The ultraviolet disinfection handbook, American Water Works Association, 2008.

[2] U. EPA, National Primary Drinking Water Regulations: Disinfectants and Disinfection Byproducts, 63 (1998). https://www.gpo.gov/fdsys/pkg/FR-1998-12-16/pdf/98-32887.pdf.

[3] M.D. Sobsey, Managing Water in the Home: Accelerated Health Gains from Improved Water Supply, World Health. 8 (2004) 1–83. doi:10.1111/j.1461-0248.2005.00820.x.

[4] U. Von Gunten, J. Hoigne, Bromate Formation during Ozonation of Bromide-Containing Waters: Interaction of Ozone and Hydroxyl Radical Reactions, 1994. https://pubs.acs.org/sharingguidelines.

[5] R.L. Wolfe, Ultraviolet disinfection of potable water, Environ. Sci. Technol. 24 (1990) 768–773. doi:10.1021/es00076a001.

[6] USEPA, Ultraviolet Disinfection Guidance Manual for the Final Long Term 2 Enhanced Surface Water Treatment Rule, Office of Water, Washington DC, 2006. https://nepis.epa.gov/Exe/ZyPDF.cgi?Dockey=600006T3.txt.

[7] J.R. Bolton, Ultraviolet Applications Handbook, 3rd ed., ICC Lifelong Leam, Inc., 2013.

[8] K. Oguma, H. Katayama, S. Ohgaki, Photoreactivation of Escherichia coli after low- or medium-pressure UV disinfection determined by an endonuclease sensitive site assay, Appl. Environ. Microbiol. 68 (2002) 6029–6035. doi:10.1128/AEM.68.12.6029-6035.2002.

[9] W. Harm, Biological effects of ultraviolet radiation, Cambridge University Press, 1980.

[10] K. Oguma, UV LEDs for Water Treatment : Research Overview and Perspectives, IUVA News. 20 (2017) 18–20.

[11] F. Taghipour, UV LED Technology: The Times They are A-Changin', IUVA News. 20 (2018) 14–17. http://iuvanews.com/stories/pdf/IUVA_2018_Quarter1_Taghipour-article_hyperlinks.pdf.

[12] K. Song, F. Taghipour, M. Mohseni, Microorganisms inactivation by continuous and pulsed irradiation of ultraviolet light-emitting diodes (UV-LEDs), Chem. Eng. J. 343 (2018) 362–370. doi:10.1016/j.cej.2018.03.020.

[13] J. Chen, S. Loeb, J.-H. Kim, LED revolution: fundamentals and prospects for UV disinfection applications, Environ. Sci. Water Res. Technol. 3 (2017) 188–202. doi:10.1039/C6EW00241B.

[14] Y. Taniyasu, M. Kasu, T. Makimoto, An aluminium nitride light-emitting diode with a wavelength of 210 nanometres, (2006). doi:10.1038/nature04760.

[15] J.S. Blakemore, Semiconducting and other major properties of gallium arsenide, J. Appl. Phys. 53 (1982). http://aip.scitation.org/toc/jap/53/10 (accessed July 25, 2018).

[16] M. a. Würtele, T. Kolbe, M. Lipsz, a. Külberg, M. Weyers, M. Kneissl, M. Jekel, Application of GaN-based ultraviolet-C light emitting diodes - UV LEDs - for water disinfection, Water Res. 45 (2011) 1481–1489. doi:10.1016/j.watres.2010.11.015.

[17] M. a. S. Ibrahim, J. MacAdam, O. Autin, B. Jefferson, Evaluating the impact of LED bulb development on the economic viability of ultraviolet technology for disinfection, Environ. Technol. 35 (2014) 400–406. doi:10.1080/09593330.2013.829858.

[18] H. Rothblatt, Why the Capabilities of a 100mW UVC LED are Kind of a Big Deal. | Ultra violet LED | Irtronix, Inc., (2017). https://www.irtronix.com/single-post/2017/12/04/Why-the-Capabilities-of-a-100mW-UVC-LED-is-Kind-of-a-Big-Deal (accessed September 25, 2018).

[19] M. Shatalov, Deep UV LEDs with record external quantum efficiency, Semicond. Today. 7 (2012) 92–93.

[20] A.M. Munshi, D.L. Dheeraj, V.T. Fauske, D.-C. Kim, A.T.J. Van Helvoort, B.-O. Fimland, H. Weman, Vertically Aligned GaAs Nanowires on Graphite and Few-Layer Graphene: Generic Model and Epitaxial Growth, Nano Lett. 12 (2012) 4570–4576. doi:10.1021/nl3018115.

[21] NANOWIRES ON GRAPHENE, (n.d.). http://crayonano.com/technology/ (accessed September 25, 2018).

[22] A. Kheyrandish, M. Mohseni, F. Taghipour, Protocol for Determining Ultraviolet Light Emitting Diode (UV-LED) Fluence for Microbial Inactivation Studies, (2018). doi:10.1021/acs.est.7b05797.

[23] M.A. Cataldo Hernández, A. May, A. Bonakdapour, M. Mohseni, D.P. Wilkinson, Analytical quantification of electrochemical ferrates for drinking water treatments, Can.

J. Chem. 95 (2017) 105–112. doi:10.1139/cjc-2016-0315.

[24] Safe Water for First Nations | The Council of Canadians, (n.d.). https://canadians.org/fn-water (accessed July 25, 2018).

[25] Fact check: Indigenous water crisis isn't improving, despite promises from Trudeau – VICE News, (n.d.). https://news.vice.com/en_ca/article/j5da9g/fact-check-indigenous-water-crisis-isnt-improving-despite-promises-from-trudeau (accessed July 25, 2018).

[26] Canada's Indigenous water crisis – VICE News, (n.d.). https://news.vice.com/en_ca/article/3kpjby/canadas-indigenous-water-crisis (accessed July 25, 2018).

[27] M. Cataldo-Hernández, M. Stewart, A. Bonakdarpour, M. Mohseni, D.P. Wilkinson, Degradation of ferrate species produced electrochemically for use in drinking water treatment applications, Can. J. Chem. Eng. 96 (2018) 1045–1052. doi:10.1002/cjce.23073.

[28] Daily Updated Map of Canada's Boil Water Advisories (BWA), (n.d.). http://www.watertoday.ca/map-graphic.asp (accessed July 25, 2018).

[29] C.K. Barstow, A.D. Dotson, K.G. Linden, Assessing point-of-use ultraviolet disinfection for safe water in urban developing communities, (2014). doi:10.2166/wh.2014.223.

[30] B. Guragai, S. Takizawa, T. Hashimoto, K. Oguma, Effects of inequality of supply hours on consumers' coping strategies and perceptions of intermittent water supply in Kathmandu Valley, Nepal, Sci. Total Environ. 599–600 (2017) 431–441. doi:10.1016/j.scitotenv.2017.04.182.

[31] M. Gold, E.A. Thomas, R.L. Byyny, J.P. Habanabakize, M. Gold, E. Thomas, R. Habanabakize, Development and Implementation of the Bring Your Own Water Treatment System in Dense, Rural, and Mountainous Rwandan Communities, 2007. https://pdxscholar.library.pdx.edu/mengin_fac.

[32] S.A. Brownell, A.R. Chakrabarti, F.M. Kaser, L.G. Connelly, R.L. Peletz, F. Reygadas, M.J. Lang, D.M. Kammen, K.L. Nelson, Assessment of a low-cost, point-of-use, ultraviolet water disinfection technology, J. Water Health. 6 (2008) 53–65. doi:10.2166/wh.2007.015.

[33] D.A. Sozzi, F. Taghipour, UV reactor performance modeling by Eulerian and Lagrangian

methods, Environ. Sci. Technol. 40 (2006) 1609–1615. doi:10.1021/es051006x.

[34] S. Elyasi, F. Taghipour, Simulation of UV photoreactor for water disinfection in Eulerian framework, Chem. Eng. Sci. 61 (2006) 4741–4749. doi:10.1016/j.ces.2006.03.010.

[35] J.J. Ducoste, D. Liu, K. Linden, Alternative Approaches to Modeling Fluence Distribution and Microbial Inactivation in Ultraviolet Reactors: Lagrangian versus Eulerian, J. Environ. Eng. 131 (2005) 1393–1403. doi:10.1061/(ASCE)0733-9372(2005)131:10(1393).

[36] A. Kheyrandish, M. Mohseni, F. Taghipour, Development of a method for the characterization and operation of UV-LED for water treatment, Water Res. 122 (2017) 570–579. doi:10.1016/j.watres.2017.06.015.

[37] A. Kheyrandish, M. Mohseni, F. Taghipour, IUVA News, Int. Ultrav. Assoc. 18 (2016) 20–21.

[38] R.M. Jenny, O.D. Simmons, M. Shatalov, J.J. Ducoste, Modeling a continuous flow ultraviolet Light Emitting Diode reactor using computational fluid dynamics, Chem. Eng. Sci. 116 (2014) 524–535. doi:10.1016/j.ces.2014.05.020.

[39] C. Bowker, A. Sain, M. Shatalov, J. Ducoste, Microbial UV fluence-response assessment using a novel UV-LED collimated beam system, Water Res. 45 (2011) 2011–2019. doi:10.1016/j.watres.2010.12.005.

[40] C. Casado, R. Timmers, A. Sergejevs, C.T. Clarke, D.W.E. Allsopp, C.R. Bowen, R. van Grieken, J. Marugán, Design and validation of a LED-based high intensity photocatalytic reactor for quantifying activity measurements, Chem. Eng. J. 327 (2017) 1043–1055. doi:10.1016/j.cej.2017.06.167.

[41] J.R. Grandusky, J. Chen, S.R. Gibb, M.C. Mendrick, C. Moe, M. Wraback, L.J. Schowalter, High Output Power from 260 nm Pseudomorphic Ultraviolet Light-Emitting Diodes with Improved Thermal Performance, Appl. Phys. Express. 4 (2011). http://iopscience.iop.org.ezproxy.library.ubc.ca/article/10.1143/APEX.4.082101/pdf (accessed July 2, 2018).

[42] A. Kheyrandish, F. Taghipour, M. Mohseni, UV-LED Radiation Modeling and its Applications in Dose Determination for Water Treatment, J. Photochem. Photobiol. A Chem. 352 (2017) 113–121. doi:https://doi.org/10.1016/j.jphotochem.2017.10.047.

[43] R. Simons, U.E. Gabbai, M. a. Moram, Optical fluence modelling for ultraviolet light emitting diode-based water treatment systems, Water Res. 66 (2014) 338–349. doi:10.1016/j.watres.2014.08.031.

[44] K. Oguma, R. Kita, S. Takizawa, Effects of Arrangement of UV Light-Emitting Diodes on the Inactivation Efficiency of Microorganisms in Water, Photochem. Photobiol. 92 (2016) 314–317. doi:10.1111/php.12571.

[45] M.G. Carvalho, T.L. Farias, Modelling of Heat Transfer in Radiating and Combusting Systems, Chem. Eng. Res. Des. 76 (1998) 175–184. doi:10.1205/026387698524749.

[46] V. Pareek, S. Chong, M. Tadé, A.A. Adesina, Light intensity distribution in heterogenous photocatalytic reactors, Asia-Pacific J. Chem. Eng. 3 (2008) 171–201. doi:10.1002/apj.129.

[47] D. Le Hardy, Y. Favennec, B. Rousseau, F. Hecht, Specular reflection treatment for the 3D radiative transfer equation solved with the discrete ordinates method, J. Comput. Phys. 334 (2017) 541–572. doi:10.1016/J.JCP.2017.01.019.

[48] S. Elyasi, F. Taghipour, General method of simulating radiation fields using measured boundary values, Chem. Eng. Sci. 65 (2010) 5573–5581. doi:10.1016/j.ces.2010.08.009.

[49] K.G. Chatterley Christie; Linden, UV-LED Irradiation Technology for Point-of-Use Water Disinfection, 2003. doi:doi:10.2175/193864709793848176.

[50] K. Oguma, R. Kita, H. Sakai, M. Murakami, S. Takizawa, Application of UV light emitting diodes to batch and flow-through water disinfection systems, Desalination. 328 (2013) 24–30. doi:10.1016/j.desal.2013.08.014.

[51] K. Song, M. Mohseni, F. Taghipour, Application of ultraviolet light-emitting diodes (UV-LEDs) for water disinfection: A review, Water Res. 94 (2016) 341–349.

[52] K. Oguma, S. Rattanakul, J.R. Bolton, Application of UV Light-Emitting Diodes to Adenovirus in Water, J. Environ. Eng. 142 (2015) 1–6. doi:10.1061/(ASCE)EE.1943-7870.0001061.

[53] J.R. Bolton, K.G. Linden, Standardization of Methods for Fluence (UV Dose) Determination in Bench-Scale UV Experiments, J. Environ. Eng. 129 (2003) 209–215. doi:10.1061/(ASCE)0733-9372(2003)129:3(209).

[54] J. Kuipers, H. Bruning, D. Yntema, H. Rijnaarts, Wirelessly powered ultraviolet light

emitting diodes for photocatalytic oxidation, J. Photochem. Photobiol. A Chem. 299 (2015) 25–30. doi:10.1016/j.jphotochem.2014.10.017.

[55] J.R. Bolton, I. Mayor-Smith, K.G. Linden, Rethinking the Concepts of Fluence (UV Dose) and Fluence Rate: The Importance of Photon-based Units - A Systemic Review, Photochem. Photobiol. 91 (2015) 1252–1262. doi:10.1111/php.12512.

[56] R. Tsekov, P.G. Smirniotis, Radiation field in continuous annular photocatalytic reactors: Role of the lamp finite size, Chem. Eng. Sci. 52 (1997) 1667–1671. doi:10.1016/S0009-2509(97)00006-7.

[57] E.R. Blatchley, Numerical modelling of UV intensity: Application to collimated-beam reactors and continuous-flow systems, Water Res. 31 (1997) 2205–2218. doi:10.1016/S0043-1354(97)82238-5.

[58] J.S. Devia-orjuela, L.A. Betancourt-buitrago, F. Machuca-martinez, CFD modeling of a UV-A LED baffled flat-plate photoreactor for environment applications : a mining wastewater case, Environ. Sci. Pollut. Res. (2018). doi:https://doi.org/10.1007/s11356-018-2431-2.

[59] D. Liu, J. Ducoste, S. Jin, K. Linden, Evaluation of alternative fluence rate distribution models, J. Water Supply Res. Technol. - Aqua. 53 (2004) 391–408. http://aqua.iwaponline.com/content/53/6/391.abstract.

[60] A. Gross, F. Stangl, K. Hoenes, M. Sift, M. Hessling, Improved Drinking Water Disinfection with UVC-LEDs for Escherichia Coli and Bacillus Subtilis Utilizing Quartz Tubes as Light Guide, Water. 7 (2015) 4605–4621. doi:10.3390/w7094605.

[61] A. Hajimalayeri, Effect of UV-LED Fluence Rate and Reflection on Inactivation of Microorganisms, 2014.

[62] F. Wu, Q. Huang, A precise model of LED lighting and its application in uniform illumination system, Optoelectron. Lett. 7 (2011) 334–336. doi:10.1007/s11801-011-1031-x.

[63] FLUENT 6.3 User's Guide, (2006).

[64] J.E. Duran, F. Taghipour, M. Mohseni, Irradiance modeling in annular photoreactors using the finite-volume method, J. Photochem. Photobiol. A Chem. 215 (2010) 81–89. doi:10.1016/j.jphotochem.2010.07.027.

[65] R.M. Jenny, M.N. Jasper, O.D. Simmons, M. Shatalov, J.J. Ducoste, Heuristic optimization of a continuous flow point-of-use UV-LED disinfection reactor using computational fluid dynamics, Water Res. 83 (2015) 310–318. doi:10.1016/j.watres.2015.06.031.

[66] R.O. Rahn, M.I. Stefan, J.R. Bolton, E. Goren, P.-S. Shaw, K.R. Lykke, Quantum yield of the iodide-iodate chemical actinometer: dependence on wavelength and concentrations., Photochem. Photobiol. 78 (2003) 146–152. doi:10.1562/0031-8655(2003)0780146qyotic2.0.co2.

[67] R. Sommer, A. Cabaj, T. Haider, G. Hirschmann, UV Drinking Water Disinfection–Requirements, Testing and Surveillance: Exemplified by the Austrian National Standards M 5873-1 and M 5873-2, IUVA News. 6 (2004) 27–35. http://iuva.org/sites/default/files/member/news/IUVA_news/Vol06/Issue4/060404SommeretalArticle.pdf.

[68] J.R. Bolton, Action Spectra : A Review, IUVA News. 19 (2017) 10–12. http://iuvanews.com/stories/070317/action-spectra.shtml.

[69] A.H. Malayeri, M. Mohseni, B. Cairns, J.R. Bolton, UV dose required to achieve incremental log inactivation of bacteria, protozoa and viruses, IUVA News. 18 (2016) 3. http://uvsalesinfo.com/Documents/NavLink/UV_Destruction_Chart_uid7102009502412.pdf.

[70] M. Cho, J. Kim, J.Y. Kim, J. Yoon, J.H. Kim, Mechanisms of Escherichia coli inactivation by several disinfectants, Water Res. 44 (2010) 3410–3418. doi:10.1016/j.watres.2010.03.017.

[71] G.A. Shin, M.D. Sobsey, Inactivation of norovirus by chlorine disinfection of water, Water Res. 42 (2008) 4562–4568. doi:10.1016/j.watres.2008.08.001.

[72] M. Adams, Bacteriophages., Bacteriophages. (1959) 620.

[73] I. Thormaehlen, J. Straub, U. Griguli, Refractive index of water and its dependence on wavelength, temperature and density, J. Phys. Chem. Ref. Data. 14 (1985) 933–1945. doi:10.1063/1.555743.

[74] E. Siamak, T. Fariborz, Simulation of UV photoreactor for degradation of chemical contaminants: Model development and evaluation, Environ. Sci. Technol. 44 (2010)

2056–2063. doi:10.1021/es902391t.

[75] M. Bagheri, M. Mohseni, Computational fluid dynamics (CFD) modeling of VUV/UV photoreactors for water treatment, Chem. Eng. J. 256 (2014) 51–60. doi:10.1016/j.cej.2014.06.068.

[76] D. Liu, C. Wu, K. Linden, J. Ducoste, Numerical simulation of UV disinfection reactors: Evaluation of alternative turbulence models, Appl. Math. Model. 31 (2007) 1753–1769. doi:10.1016/j.apm.2006.06.004.

[77] M. Hessling, A. Gross, K. Hoenes, M. Rath, F. Stangl, H. Tritschler, M. Sift, Efficient Disinfection of Tap and Surface Water with Single High Power 285 nm LED and Square Quartz Tube, Photonics. 3 (2016) 7. doi:10.3390/photonics3010007.

[78] Z. Wang, J. Liu, Y. Dai, W. Dong, S. Zhang, J. Chen, CFD modeling of a UV-LED photocatalytic odor abatement process in a continuous reactor, J. Hazard. Mater. 215–216 (2012) 25–31. doi:10.1016/j.jhazmat.2012.02.021.